Electrospun Polymeric Nanocomposites for Aqueous Inorganic and Organic Pollutant Removal

by

Natalia Virginia Hoogesteijn von Reitzenstein

A Dissertation Presented in Partial Fulfillment
of the Requirements for the Degree
Doctor of Philosophy

Approved March 2018 by the
Graduate Supervisory Committee:

Paul Westerhoff, Chair
Pierre Herckes
Kiril Hristovski
François Perreault

ARIZONA STATE UNIVERSITY

August 2018

ABSTRACT

Electrospinning is a means of fabricating micron-scale diameter fiber networks

with enmeshed nanomaterials. Polymeric nanocomposites for water treatment require the

manipulation of fiber morphology to expose nanomaterial surface area while anchoring

the nanomaterials and maintaining fiber integrity; that is the overarching goal of this

dissertation. The first investigation studied the effect of metal oxide nanomaterial

loadings on electrospinning process parameters such as critical voltage, viscosity, fiber

diameter, and nanomaterial distribution. Increases in nanomaterial loading below 5%

(w/v) were not found to affect critical voltage or fiber diameter. Nanomaterial dispersion

was conserved throughout the process. Arsenic adsorption tests determined that the fibers

were non-porous. Next, the morphologies of fibers made with carbonaceous materials

and the effect of final fiber assembly on adsorption kinetics of a model organic

contaminant (phenanthrene, PNT) was investigated. Superfine powdered activated carbon

(SPAC), C_{60} fullerenes, multi-walled carbon nanotubes, and graphene platelets were

added to PS and electrospun. SPAC maintained its internal pore structure and created

porous fibers which had 30% greater PNT sorption than PS alone and a sevenfold

increase in surface area. Carbon-based nanomaterial-PS fibers were thicker but less

capacious than neat polystyrene electrospun fibers. The surface areas of the carbonaceous

nanomaterial-polystyrene composites decreased compared to neat PS, and PNT

adsorption experiments yielded decreased capacity for two out of three carbonaceous

nanomaterials. Finally, the morphology and arsenic adsorption capacity of a porous TiO_2-

PS porous fiber was investigated. Porous fiber was made using polyvinylpyrrolidone (PVP) as a porogen. PVP, PS, and TiO_2 were co-spun and the PVP was subsequently eliminated, leaving behind a porous fiber morphology which increased the surface area of the fiber sevenfold and exposed the nanoscale TiO_2 enmeshed inside the PS. TiO_2-PS fibers had comparable arsenic adsorption performance to non-embedded TiO_2 despite containing less TiO_2 mass. The use of a sacrificial polymer as a porogen facilitates the creation of a fiber morphology which provides access points between the target pollutant in an aqueous matrix and the sorptive nanomaterials enmeshed inside the fiber while anchoring the nanomaterials, thus preventing release.

DEDICATION

This work is dedicated to my family. Thank you for your encouragement and

support.

TABLE OF CONTENTS

LIST OF TABLES

LIST OF FIGURES

Figure Page

CHAPTER 1

INTRODUCTION & BACKGROUND

1.1 Identifying the Need for Alternative Sources of Clean Water

More than 700 million people lack access to clean drinking water.[1] As

conventional sources of drinking water become stressed, unconventional water sources,

such as surface water, storm water, and seawater, are being investigated for the provision

of drinking water as demand grows. Meanwhile, existing water infrastructure deteriorates

and new infrastructure does not materialize, motivating alternative means of producing

clean drinking water in underserved areas, including rural areas of the United States.

Going "off the grid" or constructing less capital-intensive small scale systems and

extracting water from a nearby source, such as a well or river, becomes an alternative to

centralized infrastructure as public health crises, such as the 2016 Flint water crisis and

the 2017 drought in Cape Town, arise. To meet this demand, new technologies that

surpass centralized Victorian-age water treatment methods are needed to meet the

complex water quality challenges that these sources provide.[2]

Small-scale systems and point-of-use/point-of-entry (POU/POE) treatment

systems provide alternative methods of obtaining clean water where centralized treatment

systems do not exist. The Environmental Protection Agency defines a small-scale water

treatment system as one serving between 25-500 people. 84% of the treatment systems in

the United States fall into this category, and 79% of them are not compliant with federal

regulations for clean drinking water.[3] POU refers to devices installed at one tap or a small

number of taps and treat water for cooking and drinking. Point-of-entry (POE) systems treat all water entering a home, office, school, or other facility.[4] Water quality issues specific to POU and POE systems include iron, manganese, copper, silica, fluoride, phosphate, sulfate, organic contaminants (such as pesticides), volatile organic contaminants, and heavy metals.[3,5] The complexity of the water matrices that these systems must treat represent an opportunity for the development of targeted, innovative materials and processes which can exceed existing centralized water treatment technology performance in a fraction of the space required and at lower cost.[2]

Nanomaterials are highly efficient, multifunctional materials which provide many opportunities for the development of alternative water treatment technologies to satisfy the increasing demand for clean water, especially where conventional infrastructure is not present.[1,6] Nanomaterials may be synthesized from the bottom-up, which allows their physical and chemical properties to be fine-tuned for specific applications. The ability to manipulate the atomic structure makes it possible to change properties such as hardness, color, corrosion resistance, surface area, catalytic activity, magnetism, and melting point, among others.[7] For sorption applications, for example, pore size and structure of nanomaterials can be tuned for faster kinetics. Additionally, composite nanomaterials may be synthesized to produce one multi-functional structure that targets multiple contaminants with faster mass transfer while taking up less space than its bulk counterpart. Nano-sized replacements for bulk materials commonly used in water treatment are being investigated as next-generation technologies.[2,6,8–10]

Despite their many benefits, unintended nanomaterial release may pose perceived or actual human risk. For this reason, it is desirable to immobilize nanomaterials in a way that does not inhibit their benefits while anchoring them to a scaffold that facilitates their application. Electrospinning provides a means of anchoring nanomaterials to a flexible web of nano- to micron-diameter fibers, similar to a neural network. One of the major limitations of combining polymers and nanomaterials is the blocking of the reactive nanomaterial surface by polymer. The engineering of pores on the surface of the fiber should facilitate the exposure of the nanomaterials within the fiber so that the nanomaterial surface is still available for reactions with target molecules. Gaps in the literature exist at the intersection of electrospinning, sorptive nanomaterials, and the application of sorptive nanomaterial-polymer composites in fluids. The use of nanomaterials as additives in electrospun fibers is known to increase fiber diameter and increase surface roughness, but the manipulation of the porosity of the fiber surface during the electrospinning process is a research area where many questions remain.[11–15]

This dissertation is structured to provide background on nanomaterials, electrospinning, and applications of nanomaterials and electrospinning with an emphasis on water treatment, particularly sorption, and present original research expanding scientific understanding of the incorporation of sorptive nanomaterials into electrospun fibers for application as aqueous adsorbent networks. The research presented in the following chapters strives to answer central research question: How can we immobilize nanomaterials in a way that will retain their unique functionality for treating water while mitigating their risk of release? The following chapters contain original, published

research on the integration of three metal oxides and four carbonaceous nanomaterials into electrospun fibers with the aim of producing a nanomaterial network able to sorb aqueous organic and inorganic pollutants.

1.2 Research Objective

The objective of this dissertation is to answer the principal research question:

How can the surface area of nanomaterials available for reactions with target molecules be maximized without compromising the integrity of the electrospun polymeric support?

Answers to this question are proposed herein after conducting literature reviews of existing research as it pertains to polymers, electrospinning, nanomaterials, and sorption, after performing detailed, original research, and after analyzing and processing findings and their significance to the scientific and engineering community. The literature review can be found in Chapter 2 and covers pertinent existing research related to the primary question. Original research addressing the following research hypotheses as part of the primary research question are answered in Chapters 3 through 6. Chapter 7 synthesizes the entire effort to address the principal question. Chapter 8 provides summaries of the research conducted in Chapters 3 through 6, major conclusions of the research, and looks to the future by identifying key research needs and future work as it related to the advancement of the research presented here.

1.3 Research Questions and Hypotheses

This dissertation addressed seven research questions. They are listed under their corresponding research projects, written as chapters for purposes of this document. Hypotheses appear below the corresponding research question.

Chapter 3: Morphology, Structure, and Properties of Metal Oxide/Polymer Electrospun Mats

1. Do metal oxide nanoparticle loadings at 0.05, 0.5, and 5% (m/v) increase electrospinning solution viscosity, increase voltage required to observe a Taylor cone, or increase electrospun fiber diameter?

   Hypothesis 1. Adding nanomaterials of any quantity will increase solution viscosity, therefore requiring higher voltage and resulting in larger fiber diameters than neat polymer fibers.

2. Can metal oxide nanomaterials be incorporated into electrospun fibers without post-spinning treatment to enable arsenate adsorption by the composite nanofiber?

   Hypothesis 2. The use of volatile organic solvents, such as Dimethylformamide (DMF), will induce a fiber surface porosity which will provide access points for target contaminants, such as arsenic, to be removed from aqueous solution via nanosorbents (TiO_2) embedded in the fiber.

Chapter 4: Superfine Powdered Activated Carbon Incorporated into Electrospun Polystyrene Fibers Preserve Adsorption Capacity

3. Can superfine powdered activated carbon be incorporated into electrospun polystyrene fibers in a single step while preserving accessibility to SPAC's inner pore network?

    Hypothesis 3. SPAC can be incorporated into electrospun polymeric matrices in a single step without post-treatment while preserving accessibility to SPAC's inner pore network.

Chapter 5: Morphology of Polymeric Electrospun Fiber Containing Multi-Dimensional Nanomaterials for Water Purification

4. How does the incorporation of different carbonaceous nanomaterial geometries into electrospun polystyrene fibers change the pore diameter, frequency, or shape?

    Hypothesis 4. The porous nature of hybrid CNM composites leads to increases in diameter, pore size, and number of pores compared to a neat polymer fiber, while Dimethylformamide (DMF) evaporation from the NM inside the polymer leaves behind inter-connected pores in the solidified polymer.

Chapter 6: Hierarchical Pore Structures of Electrospun Titanium Dioxide

Nanocomposites for Arsenate Removal

5. Does the use of a sacrificial polymer as a porogen during electrospinning induce the production of meso- and macropores in a TiO_2-PS electrospun fiber?

   Hypothesis 5. By manipulating the phase separation process between the two polymers during and after electrospinning, a unique meso- and macro-porosity will remain on the surface of the TiO_2-PS fiber after PVP elimination via dissolution.

6. How does the porosity of a TiO_2-PS-PVP fiber change before and after PVP elimination?

   Hypothesis 6. As PVP is eliminated from the fiber matrix via dissolution, internal surface area previously occupied by the PVP chains will become available, making pore size and number increase and opening slit-like pores in the fiber surface.

7. Does the sacrificial polymer method used in TiO_2-PS fibers, GO-PS fibers, and TiO_2-GO-PS fibers facilitate adsorption of representative oxo-anions (arsenate) and polar organic (pCBA) pollutants?

   Hypothesis 7:
   Using the sacrificial polymer method will make GO and TiO_2 surface area available for adsorption of arsenate and pCBA.

Figure 1.1 Research Questions and Corresponding Hypotheses. Nanomaterial-polymer fiber electrospinning process and related research questions and hypotheses. From polymer solution injection to fiber collection with diagram of fiber segment structure (top), and pollutant sorption via porous morphology of fibers, making nanomaterials in fiber interior accessible to aqueous matrix (bottom).

CHAPTER 2

LITERATURE REVIEW

Understanding the context of an original idea is critical to successful research. To that end, this chapter summarizes information related to the use of (1) background information related to arsenic and phenanthrene, which were used as model pollutants for the purposes of demonstrating adsorption capacity of electrospun nanomaterial-polymer fibers, (2) opportunities for nanomaterials as technology for water treatment, as well as information on (3) electrospinning, a technique which allows nanomaterials' desirable properties to be harnessed while mitigating the risk of their release, and (4) a summary of research needs.

Pollutants of Concern

Arsenic in the U.S.

Arsenic has been classified by the International Agency for Research on Cancer (IARC) as a Group 1 carcinogen: carcinogenic to humans.[16,17] Arsenic occurs naturally in mineral complexes in rocks and soils, waterways, and can also be found in synthetic substances such as insecticides, herbicides, wood preservatives, and in paints, wallpapers, and ceramics. Natural concentrations of arsenic typically range between 3-4 ppm in soils.[18] It is estimated that 8 million pounds of arsenic are released into the environment in a single year from anthropogenic sources.[19] 2% of U.S. drinking water exceeds 20 ppb of arsenic.[18] Once arsenic is released into the environment, it may undergo oxidation-

reduction reactions, transformations, and ligand exchange depending on its oxidation state, reduction potential, pH, temperature, salinity, and concentrations of iron and sulfides.[18,20–23] Arsenic is a tasteless and odorless substance that exists mainly in two oxidation states – pentavalent (As(V)) or trivalent (As(III)). As(V) is associated with divalent anion $HAsO_4^{2-}$ and monovalent anion $H2AsO_4^{1-}$ (pKa of the two anions is 6.8).[24]

Inorganic arsenic is taken up primarily by the liver cell and methylated and reduced in the body.[18] Arsenic exposure may result in a variety of human health effects including increased risk of skin, lung, liver, bladder, kidney, and colon cancer.[23] Oral toxicity of arsenic is the most deleterious to animals. Humans will begin to develop lesions from arsenic exposure levels between 0.002-0.02 mg As/kg/day. High blood pressure, circulatory problems, respiratory problems, birth defects, miscarriages, cyanosis, and gangrene are also associated with arsenic exposure. The EPA has calculated an oral cancer slope factor of 1.5 $(mg/kg/day)^{-1}$; the Agency for Toxic Substances and Disease has suggested an oral minimal risk level (MRL) of 0.005 mg As/kg/day for acute exposure (less than 14 days) and 0.0003 mg As/kg/day for chronic exposure (365+ days). Urban storm water runoff has been found to contain between 1-50 ppb of arsenic.[25] Arsenic in drinking water is regulated under the Safe Drinking Water Act at a maximum contaminant level (MCL) of 10 ppb. The World Health organization also suggest this MCL has a guideline for drinking water supplies.[26] Data obtained from 31,350 private groundwater wells in 2001 shows high concentrations of arsenic in the western, Midwestern, and northeastern U.S (Figure 2.1).[27] Arsenic intoxication persists in the United States into the present day.

Aqueous arsenic removal technologies

The most common methods of arsenic removal from the water supply include oxidation, precipitation, coagulation, sorption, and ion exchange. Arsenic removal using metal oxides as adsorbents is known as an effective technology due to its low cost, consistent removal efficiency, and ease of operation and maintenance.[24,28–30] Manganese oxides, iron oxides, activated alumina, and titanium dioxide, among others, appear in the literature as metal oxide-based materials which have been used as arsenic adsorbents.[30] For the purposes of this work, mechanistic descriptions will be limited to arsenic adsorption onto nanoscale titanium dioxide, covered in section 2.3.2 of this dissertation.

Adsorption Isotherms

Adsorption isotherms describe the amount of adsorbate that can be adsorbed onto an adsorbent at equilibrium and constant temperature by exposing a known quantity of adsorbate to distinct dosages of adsorbent inside a known volume. Adsorption equilibrium capacity is calculated by using the following equation:

$$q_e = \frac{V}{M}(C_0 - C_e)$$

Where q_e=adsorbate concentration in adsorbate at equilibrium (mg/g)

V=volume of liquid added to bottle (L)

M=mass of adsorbent (g)

C_0=initial concentration of adsorbate (mg/L)

C_e=equilibrium concentration of adsorbate (mg/L)

Equations developed by Langmuir, Freundlich, and Brunauer, Emmett, and Teller (BET) are used to describe this process. The Freundlich isotherm is a two-parameter isotherm which describes adsorption on heterogeneous surfaces (sites with varying adsorption energies) using thermodynamics of adsorption using the Freundlich equation:

$$q_A = K_A C_A^{1/n}$$

Where K_A=Freundlich adsorption capacity parameter (mg/g)(L/mg)1/n

1/n=Freundlich adsorption intensity parameter (unitless)

1/n will depend on temperature:

$$\frac{1}{n} = \frac{\Delta H_M^{\circ}}{RT} - \frac{r\Delta H_{ad}^{\circ}}{R}$$

Where ΔH_M°=mean site energy J/mol

R=universal gas constant (8.314 J/mol K)

ΔH_{ad}°=change in site enthalpy (J/mol)

T=absolute temperature (K)

r=proportionality constant

The Freundlich isotherm operates under the assumptions that adsorption site energies follow a Boltzmann distribution and that the change in site entropy increases in proportion to site enthalpy and the proportionality constant.[31–33]

Inductively Coupled Plasma Mass Spectrometry

Inductively Coupled Plasma Mass Spectrometry (ICP-MS) is an analytical method used for arsenic analysis of aqueous samples. ICP-MS combines a high-temperature source (ICP) which ionizies samples and then separates those ions, with an

MS, which detects ions based on mass-to-charge ratio. A detector then translates the number of ions into an electrical signal that is measured and correlated with the number of atoms in a particular element. ICP-MS can detect arsenic concentrations down to the part-per-trillion (ppt) range.[34,35]

Polycyclic aromatic hydrocarbons in the U.S. Water Supply

Polycyclic aromatic hydrocarbons, such as phenanthrene, are a class of undesirable persistent organic pollutants (POP) based on their toxicity, mutagenicity, and carcinogenicity.[36,37] The EPA has classified 16 as aqueous PAHs as pollutants because of their toxicity to mammals and aquatic life.[38] PAHs are based on fused benzene rings, and therefore their properties are similar to those of benzene and olefinic hydrocarbons; they have low water solubility and high octanol-water partitioning coefficients.[39] They are used in the production of fluorescent dyes and pigments, but the highest contributor of PAHs to the environment is anthropogenic: the processing of coal and crude oils.[40] Their low vapor pressure combined with their benzene ring structure allows them to sorb easily to airborne particles, transporting PAHs long distances from their source.[40] Although the main sinks for PAHs are soils and sediments, they are found frequently in aqueous environments; groundwater in Germany has been found to contain between 0.045-0.51 µg/L total PAH and treated surface water from German rivers has been found to contain up to 0.234 µg/L PAH.[41,42] The EPA drinking water MCLs for PAHs are between 0.0001-0.0004 mg/L, depending on the PAH in question. High exposure to PAHs has been linked to lung cancer.

High Performance Liquid Chromatography

High Performance Liquid Chromatography (HPLC) is a technique used to identify and quantify components in mixtures via separation. Chromatography partitions sample molecules between two phases, a mobile phase, usually a gas or supercritical fluid, and a stationary phase, a highly porous solid packed inside of a column. As a sample travels through the column and sorbs and desorbs between the two phases many thousands of times, the speed at which is travels is recorded as its retention time, which is used to identify the analyte. As the sample is eluted (removed via solvation) from the column, it passes through a detector (usually UV-Vis absorbance detector) which produces a response in the form of a peak. Peak areas are proportional to analyte quantity. Peak area heights are compared to standards of known concentration to determine amount of compound in question.[43,44]

Aqueous PAH removal technologies

Conventional water treatment methods including sedimentation, coagulation and flocculation have been found to eliminate PAHs from water supplies to a high degree. Oxidation via chlorine, chlorine dioxide, and ozone treatment has also been effective.[39] One of the most cost-effective and efficient methods of PAH removal, however, is activated carbon. Granular activated carbon (GAC) is particularly suited for the adsorption of high molecular weight, hydrophobic compounds such as PAHs.[45]

14
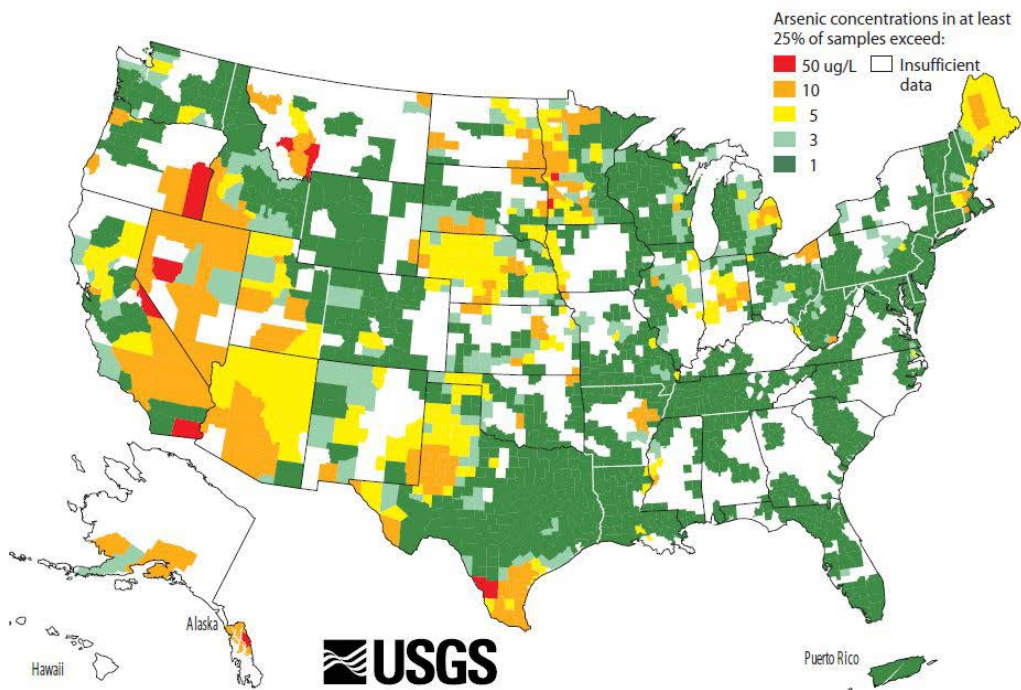
Figure 2.1 Arsenic Concentration in Groundwater Wells by County. Adapted from Ryker (2001).[27]

2.2 Nanomaterials as a Technology for Water Treatment

Nanomaterials are generally defined as materials possessing at least one dimension in the nanoscale, 0-100 nm.[6,46,47] They are inherently heterogeneous structures; they are assemblies of nanoscale building blocks and the regions between those building blocks.[7] These materials are designed from the bottom up, synthesized from gases or other reactants.[48] The ability to design them from the bottom up coupled with their small size gives them a number of desirable properties, including high surface area, short intraparticle diffusion distance, tunable pore size and surface chemistry, and low volume.[49] These characteristics make them ideal for small, modular treatment systems that can be easily transported to rural areas where large water treatment infrastructure is not feasible.

2.2.1 Nanomaterial Size & Shape Effects

Nanomaterial size is known to affect the physical and chemical properties of nanomaterials. Roduner classified size-dependent effects of nanomaterials into two categories: effects of scale related to the atoms on the surface of nanomaterials, and quantum effects, where nanomaterials exhibit behavior distinct from its bulk counterpart due to delocalization of electrons. Nanomaterials behave differently because of the number of atoms available at their surface. A larger number of available atoms at the surface implies a larger number of electrons available, especially at corner and edge sites, where corner and edge atoms have lower coordination numbers (or number of neighboring atoms) and are more available to form bonds with other molecules. This is

especially relevant for adsorption applications, where an increase in available surface atoms translates into higher surface energy for sorption.

Nanomaterials' small size makes for a much shorter intraparticle diffusion distance, meaning faster kinetics for the adsorption of contaminants.[50] Quantum effects are a product of the proximity of electron orbitals in small clusters of atoms, or density of states (DOS). In high-DOS nanomaterials, the proximity of electron bands to each other can lead to the excitation of electrons across Kubo gap (the space between the highest occupied and lowest occupied electron state, also known as the HOMO-LUMO gap) or the overlap of electron bands. These phenomena lead to discontinuities between the nanomaterial and bulk form properties of a material.[46]

Conversely, nanomaterial size can be engineered in order to apply certain properties of nanomaterials toward a specific function where bulk materials would not be suitable.[46] Pokropivny and Skorokhod classified nanostructured materials into elementary units based on structure: zero-dimensional (0D), one-dimensional (1D), two-dimensional (2D), and three-dimensional (3D) structures.[49] Zero-dimensional NM example structures include quantum dots and hollow spheres. 1D NMs consist of structures that are long and tubular in shape, including nanotubes, nanowires, and nanorods. 2D NMs include nanowalls, nanosheets, and nanoplatets. 3D structures are usually collections or crystals of lower-dimension NMs, which have been linked to form a larger network, such as zeolites.

Pore size, frequency, and tortuosity are important attributes of adsorbent materials used for contaminant remediation. The characteristics of pores dictate transport of

contaminants out of aqueous matrices, in particular, diffusion. The pore structure of a

material determines how much of a contaminant it can adsorb.[51] The trajectory and speed

of a contaminant molecule may be inhibited or delayed by the path it must take inside of

a sorbent, which in turn affects the kinetics of the adsorption reaction.[31] The increased

surface area of nanomaterials translates into lower tortuosity, which is favorable for fast

kinetics.
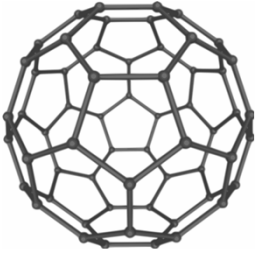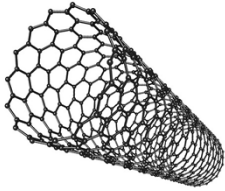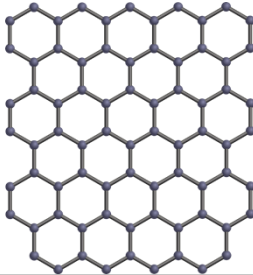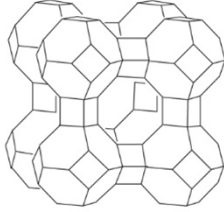
0D Nanomaterials	1D Nanomaterials	2D Nanomaterials	3D Nanomaterials
Hollow spheres, quantum dots	Nanotubes, nanowires, nanorods	Nanosheets, nanoplatets	Crystals and other collections or networks of 0-2D nanomaterials

Figure 2.2 Dimensions of Nanomaterials with Examples.

2.3 Types of Nanomaterials Relevant to Water Treatment

2.3.1 Carbonaceous Nanomaterials

Carbonaceous nanomaterials (CNMs) are composed entirely or mostly of carbon, such as graphene, fullerenes (C_{60}), and single or multiwalled carbon nanotubes (SWCNT and MWCNT respectively). They generally have high surface area, surface functionality, and surface porosity, all desirable characteristics for a sorbent material.[10,52,53] For example, graphene theoretically exhibits twice the surface area of activated carbon, the leading adsorbent material.[54] CNMs such as graphene and graphene oxide, which have surface groups on their surface (for example, oxygen and hydrogen groups), can function as good sorbents for heavy metals.[55–58] Copper, cadmium, cobalt, zinc, lead, mercury, nickel, arsenic, and chromium have all been used in adsorption studies utilizing graphene and graphene oxide as sorbents, with adsorption capacities ranging from 20-980 mg/g.[9,48] For CNMs in general, π-π stacking can also occur between the graphene sorbent and aromatic contaminants.[59] Polycyclic aromatic hydrocarbons (PAHs), volatile organic compounds (VOCs), herbicides, and dyes have also been removed using CNMs in aqueous matrices.[56,60–62]

2.3.2 Metal Oxide Nanomaterials

Metal oxide nanomaterials, such as titanium and iron oxide, have been recognized for high surface area, high catalytic activity, and potential for self-assembly.[63] Mechanisms include adsorption, chemical degradation, photodegradation, and chemical disinfection.[48] The most commonly applied metal oxide nanomaterials for water remediation include titanium dioxide (TiO_2), zero-valent iron (nZVI), and silver.[64,65,74,66–

[73] TiO$_2$ functions as a photocatalyst for the degradation of organic contaminants.[75–78]

nZVI is applied for the chemical reduction of organic solvents, dyes, pharmaceuticals, and arsenic.[79–85] Silver is used as an antimicrobial and as a photocatalyst.[67,86–89]

Mechanism of Arsenic Adsorption by Titanium Dioxide

Although TiO$_2$ is more commonly used for the degradation of pollutants via photocatalytic reactions, it can also be used as an adsorbent for the removal of As(III) and As(IV). Adsorption of As onto the TiO$_2$ surface is a step in the photo-oxidative process and will occur even without exposure to UV light. Pena et al. (2006) found As(III) and As(IV) form negatively charged inner-sphere complexes at the solid-water interface of nanoscale TiO$_2$. EXAFS studies suggest that both As species form bidentate binuclear surface complexes. From pH 5 to 10, (TiO$_2$) AsO$_2^-$ is the dominant surface species.[90–93]

2.4 Nanomaterial Toxicology & Perceived Risk

The same enhanced properties that make engineered NMs attractive also make them a toxicity concern in the case of their release. Depending on their composition and surface chemistry, nanomaterials may disperse or accumulate in waterways and soils, sorb to other surfaces, or precipitate and sink into riverbeds and ocean floors. Due to the ecological complexity of marine and freshwater environments, it is hard to consistently predict how NMs will affect plant and animal life that may be exposed. NMs become highly mobile at the cellular level and are known to disrupt cellular function. Possible mechanisms of nanomaterial toxicity at the cellular level include the production of reactive oxygen species (ROS), the disruption of cell membranes, oxidation of proteins,

and DNA damage.[94–97] Concerns about NM toxicity motivates the need for their immobilization in a way that does not inhibit their benefits. Incorporation of nanomaterials into polymer fibers via electrospinning provides a means of immobilizing different shapes of nanomaterials while still exposing their surfaces and retaining their functionality.

2.5 Operating Principles of Electrospinning & Electrospraying

In electrospinning, a charged jet of polymer solution produces filaments by applying a high voltage potential between 10-40 kV and a grounded collector (Figure 2). Charge is induced on the polymer solution surface by an electric field. The electric field overcomes the surface tension of the fluid droplet at the tip of the syringe and a jet stretches from the syringe tip and deposits onto the grounded collector, forming a mat of fibers with micro- and nanoscale diameters as the organic solvent in the polymer solution evaporates. The jet gradually changes from a stream to a whipping jet closer to the grounded collector.[98] An important feature of electrospinning is the Taylor cone, which forms at the capillary tip. Taylor cone formation indicates that the voltage applied affects the surface tension of the solution, and it is a precursor to a stable, continuous polymer jet. The charged jet is the distinguishing characteristic between electrospinning and electrospraying, where the end result of electrospraying is charged polymer droplets without fiber formation. The critical voltage occurs when the jet forms. Droplet shape at the tip varies with applied voltage. At lower voltages, the originating drop at the capillary tip is larger than the diameter of the capillary tip. As voltage increases, the jet originates

first from the bottom of the drop, and then the drop diameter decreases with increasing

voltage until the jet emerges from the solution within the syringe tip.[99] Electrospraying

functions identically, with the exception of solution manipulation (usually by lowering

viscosity) in order to produce a fine spray instead of a charged jet.[100,101]
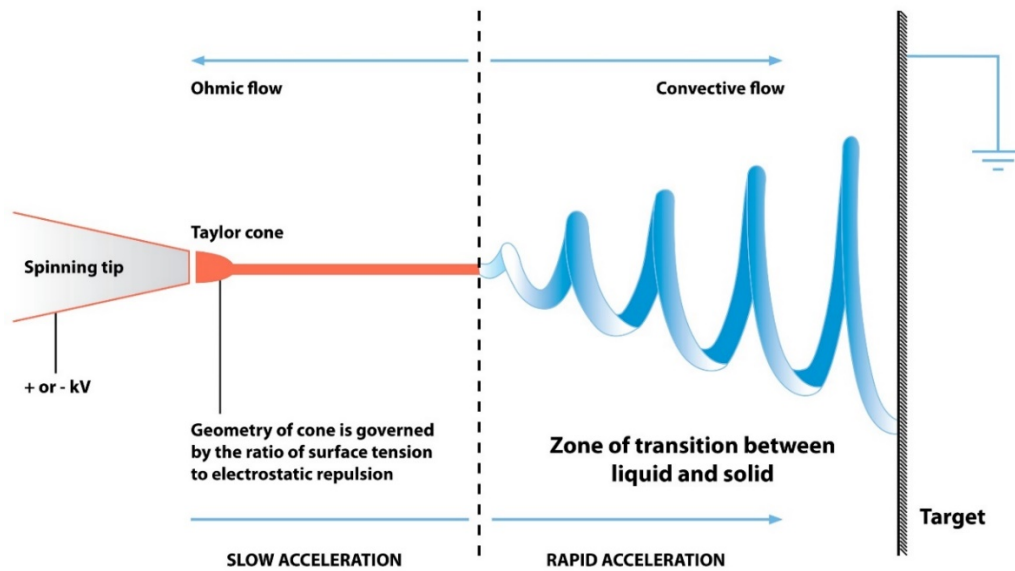
Figure 2.3 Basic Electrospinning Process Schematic. Horizontal electrospinning setup showing Taylor cone formation as well as differences in charged jet between the capillary tip and grounded collector. Diagram by Joanna Gatford/The New Zealand Institute for Plant and Food Research Ltd, distributed under a CC-BY 2.0 License.

2.5.1 Hierarchical Structures of Electrospun and Electrosprayed Fibers

The conditions under which electrospun fibers are made, or the parameters of the experiment, exert a large influence on the fiber structure. Electrospinning is usually conducted at room temperature under atmospheric conditions. Electrospinning parameters can be divided into two broad categories – solution parameters and external parameters. The resulting fiber structures can be classified into two categories: primary structures (fiber segments, beads, and bead-on-string structures) and secondary structures (nanopores, nanopapilla, and other extrusions from or surface features on the fiber surface). Table 1 lists the parameters which have been found to affect primary and secondary structures, including humidity, molecular weight of polymer, applied voltage, solution component concentrations, surface tension, pump flow rate, needle diameter, and capillary tip-to-collector distance. The properties of the polymer(s), organic solvent(s), and any additives which are added directly to the solution exert influence over pore diameter and frequency, bead morphology, and jet flight path. External conditions such as ambient humidity level, voltage applied, flow rate of the pump, needle diameter, and capillary tip-to-collector distance can be manipulated to alter fiber diameter, bead density, and surface pore diameter, shape, and frequency.

Table 2.1 Effect of Solution and External Parameters on Fiber Morphology

Parameter	Effect	Reference
Molecular weight of polymer	Pore diameter and frequency, jet bending instability and elongational flow, bead morphology	102–105
Solution component concentration	Fiber diameter, charged jet flight path, fiber morphology	99,103–105
Surface tension	Fiber diameter	106
Applied voltage	Bead formation	99
Flow rate	Fiber diameter	106
Needle diameter	Fiber diameter	107
Humidity	Surface pore diameter, shape, distribution, and frequency	102,108
Capillary tip-to-collector distance	Bead density, fiber diameter	109,110

Molecular weight of polymer(s) used for electrospinning and electrospraying is extremely important in determining fiber morphology. Molecular weight can affect pore formation, where higher molecular weight polymers coupled with humidity result in fibers with larger pores.[102,111] Molecular weight of the polymer can also affect whether or not a jet is formed. The polymer used must be heavy enough to overcome bending instability and maintain elongational flow in order to produce a continuous fiber, where a polymer that is too light may result on a spray instead of a continuous, whipping jet.[103] Bead morphology has also been observed to change with molecular weight. Eda et al. observed a hollow-cup bead morphology for polymers between 111,400-393,400 g/mol. Dish-like beads were observed for polystyrene in the 19,300-393,400 g/mol molecular weight range. Generally, a higher molecular weight polymer resulted in thicker, larger beads.[104] Molecular weight is closely tied to concentration of polymer solution

components. Higher concentrations of polymers or other solution components affect

viscosity. Deitzel et al. found that at viscosities below 1 poise, surface tension becomes

the dominant influence over fiber morphology and there is a higher likelihood that a

spray will form instead of a charged jet. At viscosities higher than 20 poise, the cohesive

nature of viscous solutions inhibits the continuity of the jet. Between 1 and 20 poise,

lower concentrations (4 % (m/v)) resulted in a mixture of droplets and fibers, while

polymer concentrations above 15 % (m/v) produced a 0.5 mm oscillating jet. Fibers

formed from higher concentration polymer solutions were also found to be of larger

diameter.[99] The relationship between molecular weight and concentration was described

by Eda et al. in the following two equations:

$$C^* \approx \frac{1}{[\eta]},$$

where C* is the limiting concentration for dilute solutions and η is the intrinsic viscosity,

and $C_e \approx \frac{\rho M_e^0}{M}$,

where entanglement concentration, C_e, is the concentration above which there is an

increase in zero shear viscosity, M is the molecular mass, ρ is the polymer density, and

M_e^0 is the average molecular mass between entanglements in the undiluted polymer.

Generally, a stable, continuous jet is achieved when the component concentration C is

above that of the entanglement concentration, C > C_e.[103,104] Molecular weight and

concentration of electrospinning solution components both exert such a large influence

on final fiber morphology, thus, it is important to take into account both of these

parameters when selecting materials for electrospun fibers. Surface tension becomes

important during the electrospinning process, when the electrical charge at the fluid surface as the polymer solution is barely pushed out of the capillary tip interacts with external electric field. There is a balance between this surface tension and electrostatic charge repulsion. As the external electric field overcomes the surface tension, an oscillating jet is produced as the fluid stretches toward the grounded collector and away from the capillary tip.[106]

A critical component in overcoming the surface tension of the polymer solution is the voltage applied to the system. Critical voltage, V_c, is the voltage at which the drop at the end of the capillary tip becomes first a Taylor cone and then a stable jet.[99] The distance between the capillary tip where the jet originates and the grounded collector where the jet terminates and the fiber is collected, where an increased distance will yield lower bead density while increasing fiber diameter.[109,110] Before the jet is produced, the pump feed rate and needle diameter can be manipulated to control fiber diameter as well. Using a smaller gauge needle (one with a larger inner diameter) will yield larger diameter fibers.[107] Using low flow rates to pump the polymer solution through the capillary tip will generally yield a smaller diameter.[106] Casper et al. and Medeiros et al. both found that electrospun fibers become porous around 25% relative humidity. Increasing the humidity results in an increased number of pores, larger diameter pores, and a wider pore size distribution.[102,108]

One important limitation of electrospinning under standard conditions is the random nature of the fibers that are produced. The oscillating jet bends in all directions at extremely high speeds, nanomaterials in the polymer solution may not be uniformly

distributed and may be affected by the external electric field, and the fiber placement on the collector is non-uniform unless a special collector is utilized.[112] As part of the internal and/or external morphology of a nanocomposite fiber, the assembly of nanomaterials inside of electrospun fibers becomes important when they play a vital role in the application of the fiber. If the nanomaterials are providing some kind of reactive role, they must be accessible and they should be distributed in a way that is optimal for the application. Park et al. studied the assembly of graphene oxide nanosheets inside poly(vinyl alcohol) electrospun fibers and found that the graphene oxide nanosheets localized toward the surface of the electrospun fibers due to rapid evaporation when water was used as solvent, but that when DMF was used as a solvent, there was a more co-continuous structure where the graphene oxide was more homogeneously distributed throughout the fiber.

2.5.2 Controlling Pore Architecture in Electrospun Fibers

Controlling the pore size, frequency, tortuosity, and interconnectivity in electrospun fiber segments is critical for contaminant transport.[113] Methods of engineering pores on electrospun fibers, summarized in Table 2, include increasing fiber diameter, changing the collector shape, focused, low density, uncompressed nanofiber (FLUF) method, salt leaching, gas foaming, and cryogenic electrospinning.

Table 2.2 Summary of Methods for Engineering Fiber Surface Pores.

Method	Reference
Increasing fiber diameter	114–122
Changes to collector shape	123
Focused, low-density, uncompressed nanofiber (FLUF)	124
Sacrificial polymer	12,113,114,125–128
Salt leaching	129,130
Gas foaming	129,131
Cryogenic electrospinning	132,133

Secondary fiber structures can be obtained by manipulating phase separation during the electrospinning process, a simpler method than making changes to the electrospinning apparatus or using methods such as salt leaching, gas foaming, and cryogenic electrospinning.[113,120] Polymer-polymer or polymer-inorganic mixtures are used to achieve specific secondary architectures. The polymer-polymer mixture method uses a sacrificial polymer as a porogen, where a supporting polymer is co-spun with a sacrificial polymer that is then dissolved or thermally eliminated without affecting the polymer of interest.[12,113,125] Thermal treatments involve heating the as-spun dual-polymer fibers to a high temperature (100-1100°C) to achieve the volatilization of the sacrificial polymer while preserving or calcining the polymer of interest.[125,126] Dissolution of a sacrificial polymer from a dual-polymer system is achieved using any solvent in which the sacrificial polymer is soluble, including water.[12,114,127,128]

A number of thermodynamic events occur as the polymer jet is accelerated during eletrospinning.[134] The formation of porous fibers are a product of competition between solvent evaporation rate and phase separation kinetics.[134–136] Solvent evaporation (also termed demixing) occurs in the sub-second range as the surface of the jet is increased

dramatically in milliseconds as it is accelerated towards the counter electrode (the collector plate). During solvent evaporation, polymer concentration increases as the volatile solvent is lost through the fiber boundary; this diffusion of the solvent through the polymer boundary can be described by Fick's second law as a special case of the Cahn-Hilliard equation:

$$\frac{\partial \phi}{\delta t} = \Lambda \nabla^2 \phi$$
Equation 2.1

Where ϕ is the volume fraction of the polymer, and Λ is the polymer-solvent mutual diffusivity. The fiber radius decreases as the total volume of the fiber decreases due to solvent mass loss over time.[135] Phase boundaries are crossed and phase separation leads to structure formation as solvent mass is lost; solidification is controlled by the glass transition process or by the onset of polymer crystallization.[137,138]

Ternary polymer solutions allow for further alteration of final fiber morphology. When two polymers are mixed in an organic solvent and subsequently spun, the resulting fiber exhibits co-continuous phase morphology (Figure 2.3).[139–141] Co-continuous morphology of polymer blends can be exploited for porous fiber formation via the extraction of one of the polymer components (via the dissolution of the water-soluble polymer in the co-continuous material, for example). Studies have achieved unique secondary structures by spinning polyacrylonitrile (PAN) with polyvinylpyrrolidone (PVP), poly(ethylene oxide) (PEO), and polystyrene (PS) and then selectively dissolving the porogenic component.[112,142,143] Bognitzki et al. (2001) found differing fiber morphology after either annealing or selective removal based on PVP dissolution based on the majority component of ternary precursor solution. Their study concluded that

29

phase separation during the electrospinning process results in co-continuous structures which are preserved by rapid solidification.[141] Co-continuous phase morphology has also been produced by spinning poly(glycolic acid) (PGA) and poly(L-lactic acid) (PLA) blends, PLA/poly(glycolide), PLA/PEO, epoxy/caprolactone, and Nafion/polyacrylonitrile blends, among others.[144–147] Kalra et al. (2008) also report co-continuous fiber structures using 10 wt% nanoparticles in poly(styrene-block-isoprene), with nanoparticles uniformly dispersed in isoprene domains. [139] The formation of co-continuous phase structures in electrospun polymeric and polymeric-nanomaterial blends followed by subsequent extraction of one component exposes more surface area than by spinning one polymer alone, making this method ideal for applications such as water treatment where reactive surface area is critical for performance.[134,139,141]
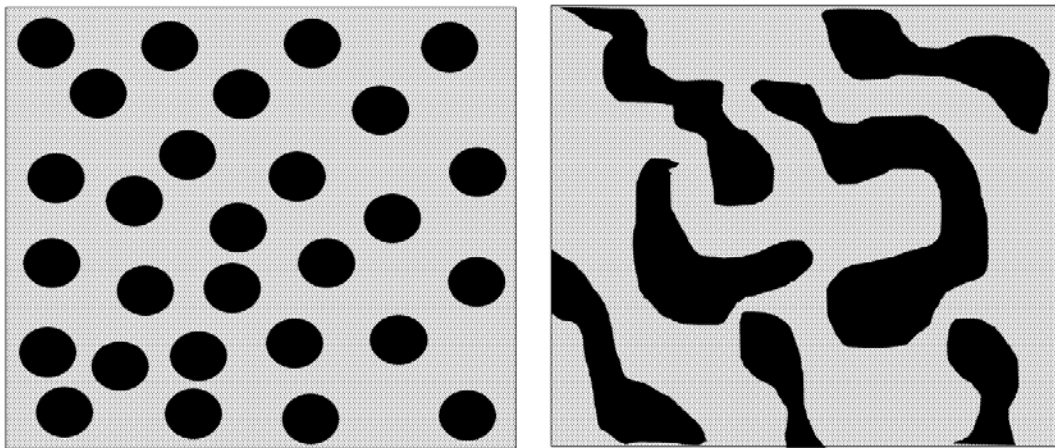
Figure 2.4 Continuous and Co-continuous Fiber Assemblies. Illustration of continuous (left) and co-continuous (right) PVP-PS copolymer morphologies.

2.5.3 Determining Pore Architecture in Polymer Composites

Surface area is related to particle size, particle morphology, surface texture, and porosity. Aqueous pollutants' ability to access reactive surface area of nanomaterials embedded inside polymeric networks governs pollutant transport and their removal from the aqueous matrix. As new adsorbents are developed using unconventional materials, new analysis methods must also be developed to adequately characterize them. Gas adsorption coupled with density functional theory, scanning electron microscopy (SEM), and mercury intrusion porosimetry and are common methods. Many conventional methods of pore size analysis used for hydrogels and ceramics are not well suited for analysis of electrospun polymeric materials, either because they compromise the delicate structures of the material or because of their inability to distinguish between pores on the fiber surface and pores caused by fiber segment overlap.[113]

Gas Adsorption

Gas adsorption measurements are widely used for surface area and pore size distribution for solid surfaces such as adsorbents, catalysts, ceramics, and building materials.[148] Physisorption occurs when a gas enriches the surface of a solid. The first stage of physisorption isotherm interpretation is to identify the isotherm type, thereby distinguishing between three adsorption processes: monolayer-multilayer adsorption, capillary condensation, or micropore filling. Pores less than 2 nm wide are termed micropores, 2-50 nm wide are termed mesopores, and greater than 50 nm are macropores. In the case of adsorbents, mesoporous materials are the most desirable.[8,77,149,150] Micropore filling is distinct from surface coverage which takes place on open macropore

or mesopore walls. Physisorption isotherms can be classified into six types. Mesoporous materials are identified by Type IV isotherms. The characteristic features of a Type IV isotherm are the hysteresis loop, an indicator of capillary condensation occurring in mesopores, as well as limited uptake over higher p/p° ranges. The initial stage of the Type IV isotherm is monolayer-multilayer adsorption. Hysteresis loops are indicative of capillary condensation in mesopore structures and can exhibit different shapes based on pore structure.[148] Brunauer-Emmett-Teller (BET) and Barrett-Joyner-Halenda (BJH) gas adsorption methods are the widely accepted standard for porous materials.

SEM

Scanning electron microscopy (SEM) can be coupled with an image processing program such as ImageJ in order to determine pore size distributions.[72,151–153] By careful preparation and imaging, followed by manually identifying pore-like cavities and measuring their diameter, Doktor (2010) found agreement between pore size distributions determined via ImageJ and pore size distributions measured using mercury porosimetry.[154] Samples, especially polymeric samples, must be coated thickly enough to be imaged clearly, but not so thickly that the coating interferes with accurate imaging of porous surfaces. This method is particularly useful for materials that possess higher numbers of larger mesopores and macropores, as well as irregularly shaped pores that may not be accounted for using existing methods such as BET or BJH. The limitation of this method is human error or difficulty identifying and measuring narrow, slit-like pores.

Mercury Intrusion Porosimetry

Mercury intrusion porosimetry (MIP) exploits the surface tension of liquid mercury and the pressure needed to force mercury into an opening to measure pore size distribution of porous materials. From pressure and intrusion data, the Washburn equation is used to generate pore volume and size distributions.[155] MIP is suitable for materials with large and distinct pores, but may fall short for electrospun materials as the pores may expand with the pressure applied using this method. Another limitation of using MIP for electrospun materials is that pores smaller than 4 micrometers may require such high pressures for intrusion that the entire scaffold may collapse.[113] Similar liquid intrusion methods, such as using ethanol, may overestimate porosity as ethanol diffuses into the fibers.[115]

2.6 Uses of Electrospun Fibers

2.6.1 Broad Applications

Due to the high level of customization afforded by electrospinning, electrospun fibers can be used in many fields, mainly biomedical, energy, and environmental applications. Biomedical engineering uses electrospinning to produce fibers used for tissue scaffolds, drug delivery, and wound healing. For example, the incorporation of water soluble drugs into a biocompatible polymer is engineered to burst at a particular time or even for sustained delivery.[156,157] Electrospun fibers can also be fabricated as conductive polymer membranes which have been studied for use as corrosion protection, energy storage, solar cells, fuel cells, and supercapacitors. Fuel cells are improved by hybridizing carbon and platinum fibers via electrospinning, thereby exploiting the surface area of the fibers and increasing the peak current for anodic catalysis.[158] Environmental applications have focused on the electrospinning of membranes and filters, where the high surface area and porosity of electrospun fibers facilitates the removal of contaminants from air and water. By exploiting the small diameters of electrospun fibers (< 500 nm), a decrease in slip flow resulting in an increase in contaminant impaction and interception increases the efficiency of an air filter compared to a conventional filter made of thicker fibers. [15,110,159,160] The high surface area afforded by the thinner diameters made possible by electrospinning are also heavily exploited for water treatment applications of electrospun fibers.

2.6.2 Applications in Water

Electrospinning provides an alternative method for fabricating micro- and nanofiltration membranes, which target not only water purification, but also disinfection. Electrospun membranes have been found to have increased water flux, and therefore decreased energy requirements, when compared to a commercial membrane due to the porosity afforded by electrospinning versus traditional membrane fabrication methods.[161] Adsorption of cadmium, phenolphthalein, oil, copper, lead, and chromium have been achieved by the manipulation of polymer surfaces and fiber porosity.[111,162–166] The use of silver nanoparticles on the surface of fibers, quaternary ammonium salts, and antibacterial polymers in anti-microbial electrospun fiber filters has been shown to kill over 95% of *E. coli* and *S. aureus*.[167–171] Although fiber alignment, pore size manipulation, surface functionalization, and the tailoring of polymers and polymer surfaces have led to increased applications of electrospinning in water treatment, there are many opportunities remaining for the fine-tuning of fiber efficacy and the exploitation of the unique characteristics which the bottom-up fabrication of electrospun fibers facilitates.

2.6.3 Nanomaterials in Electrospinning

Nanomaterials can be incorporated into electrospun polymeric fibers either by adding them to the polymer solution before electrospinning, or as a post-electrospinning treatment step applied to the spun polymer fiber to make *nanocomposites*. Nanoparticle addition into polymers is known to improve mechanical strength, resistance to wear, and

35

thermal stability.[172] Electrospinning technique allows for the addition of nanomaterials to a polymer solution directly, while electrospraying allows for increased dispersion of nanomaterials along the fiber surface while maintaining polymer integrity through the adhesion of the wet spray onto the dry fiber. Trejo et al. found that electrospraying of nanomaterials onto membranes provides the least likelihood of nanomaterial release from the scaffold.[100] The end product is a non-woven mat of nanomaterial immobilized in a polymer support. Metal oxide nanomaterials, such as titanium dioxide, have been incorporated into electrospun fibers for photocatalytic and anti-bacterial applications, however, these fibers require post-spinning treatment in order to make the metal oxide nanomaterials accessible to the aqueous matrix.[11,14,173–175]

2.8 Summary of Research Needs

There are many papers available on the synthesis, application, and optimization of nanomaterials for air and water remediation, but nanomaterials' small size, high reactivity, and ability to change their intrinsic properties in different environments as they are transported makes the risk of their release a toxicological problem.

As for electrospun polymeric sorbents, the post-spinning functionalization of the constituent polymers via thermal or chemical treatments requires energy and time, and generates toxic chemical waste. These deficiencies provide an opportunity for the union of reactive nanomaterials with a method of immobilization that retains nanomaterial efficacy in removing pollutants while mitigating the risk of nanomaterial release. However, it is not as simple as throwing together some nanomaterials and polymer molecules and spinning the solution. Making a functional, useful nanocomposite via electrospinning requires that nanomaterials be homogeneously dispersed, that their reactive surfaces are made available for the desired reactions to degrade or sequester contaminants, that the fiber itself be made of durable materials that will survive multiple uses, and that resources required are minimized to make a fiber that is competitive with additive sorbent alone. To that end, the parameters of electrospinning described earlier in this work must be manipulated in a way that satisfies the listed criteria.

2.8.1 Key Scientific Questions

- Do nanomaterials have a net positive or net negative effect on sorptive performance when used as an additive for sorptive electrospun fibers?

- How can nanomaterial weight and geometry be best suited for the ideal morphology of a sorptive electrospun fiber?

- How can polymers be manipulated during the electrospinning process to produce large enough pores to expose nanomaterials?

- How can the electrospinning process be optimized to expose reactive nanomaterial surface area?

- How can post-electrospinning treatment necessary for the production of pores be streamlined into a single step?

CHAPTER 3

MORPHOLOGY, STRUCTURE, AND PROPERTIES OF METAL OXIDE/POLYMER NANOCOMPOSITE ELECTROSPUN MATS

Hoogesteijn von Reitzenstein, N.; Bi, X.; Yang, Y.; Hristovski, K.; Westerhoff, P. *J. Appl. Polym. Sci.* **2016**, *133*, 1–9.

3.1 Abstract

Adding nanoparticles into polymer solutions before electrospinning creates unique hierarchical morphologies dispersed throughout small diameter nanoparticle-polymeric fibers. Effects of polymer composition, nanoparticle (NP) type, loading, and electrospinning voltage conditions were studied. As examples, indium, iron, and titanium oxide engineered nanoparticles (NPs) were dispersed into polyvinylpyrrolidone or polystyrene and electrospun. NP loadings below 5 % (m/v) did not affect critical voltage required for Taylor cone formation, whereas higher NP loadings require higher critical voltages. Polymeric fiber thickness and macroscopic morphology is not impacted by up to 5 % (m/v) NP loadings, and NP dispersion throughout the fibers were similar to their dispersion in initial polymer suspension. NP loadings above 5 % (m/v) increased viscosity, which decrease subsequent fiber diameter. Experiments in water containing inorganic and organic pollutants in water demonstrate that the polymer is largely non-porous. This work enables design of multifunctional nanomaterial-polymer composite fibers for wide-ranging applications such as water and air treatment.

3.2 Introduction

Electrospun polymer fibers with diameters in the submicron to nanometer range have unique characteristics that led to increasing interest in their applications as reinforcements for composite materials, air or water filtration, soft tissue prostheses, wound dressing, cosmetics, protective clothing, and sensors.[110,176] Electrospinning uses an electrically charged jet of polymer solution to produce polymer filaments by applying a high voltage potential between 10-40 kV and a grounded collector. The surface tension on the fluid droplet at the syringe tip is overcome by the strength of the electric field and a charged jet of fluid stretches from the syringe tip and deposits onto the grounded collector, forming a mat of fibers with diameters in the micro- and nanometer scale. Nanoparticle (NP) addition into polymers produces nanocomposites known to improve mechanical strength, resistance to wear, and thermal stability.[172] Additionally, NP-polymer electrospun fiber composites also enhance the fiber performance due to the multifunctionality of NPs as biocides, sorbents, and photocatalysts. As NP-polymer composites are being synthesized, limited information across multiple NP types exists regarding impacts of NPs on polymer spinning behavior.

Synergistic effects of physical parameters dictate the structure and morphology of electrospun fibers.[99] The electrospinning process is a balance of parameters including, but not limited to, conditions such as relative humidity, polymer weight, distance between capillary tip and collector plate, feed rate of solution, and solution composition.[102,108,177] For example, adjusting the relative humidity in the environment affects the number,

diameter, shape, and distribution of pores on the surface of electrospun fibers.[102] Electrostatically, there is a balance between the induced charge on the polymer surface and the surface tension of that polymer. Surface tension is overcome by applying voltage. Viscosity dictates whether the polymer jet will break into droplets or travel as a continuous stream to the collector plate. High viscosity liquids will become jets, while low viscosity liquids will break up.[99] By altering physical parameters and manipulating electrostatic forces, the fibers produced by electrospinning can have a variety of morphologies suited to different purposes. For example, fiber diameter may be manipulated via solution viscosity and applied voltage. Depending on the final use of electrospun fiber mats (i.e., non-woven textiles), controlling fiber diameter can be controlled. In this work, fiber diameter is shown to vary as an effect of NP addition. The addition of NP into solution adds another dimension to the process and its product. There are few examples in the literature of the effect of NP addition to polymer solutions prior to spinning and few investigations of the effect of NP on electrospinning process parameters.[178,179] The effect of NP content on the formation of a Taylor cone in polymer solutions for electrospinning presents a gap in the literature that is important for future investigations of electrospun fibers using NPs for functionalization.

Interest exists in coupling the benefits of metal oxide nanoparticles with the process of electrospinning, affording several applications of economically produced, micrometer and nanometer-scale fibers.[180] For example, adding antimicrobial silver NP to a mat of electrospun fibers grafted onto a membrane could help prevent bacterial

41

membrane fouling.[168] Electrospinning polymeric fibers for water treatment applications requires use of non-water soluble polymers, and hence dissolution in non-aqueous solvents is required. Titanium dioxide (TiO_2) is an inexpensive and effective photocatalyst and chemical sensor in environmental remediation, photovoltaics, and optics, and applications for electrospun fibers made with TiO_2 are beginning to be explored.[181–184] Research on interactions of individual metal oxide nanoparticles with polymers during electrospinning have begun. For example, varying weight percentages of TiO_2 in a polyaniline solution affected nanocomposite fiber diameter, while operating parameters such as TiO_2 loading content, humidity, and temperature affected the physical properties, such as strength and brittleness, of electrospun polyacrylonitrile (PAN)-TiO_2 fibers.[178,179] Less has been reported about the systematic influence of NP addition to polymer solutions on electrospinning parameters (e.g., solution viscosity) and resulting critical voltage or implications for fiber morphology.

This study investigated hybridizing electrospun fibers with NP and evaluated how the NP addition influenced polymer properties, electrospinning conditions, and electrospun fiber morphology. Specifically, we quantified the differences in critical voltage needed to produce an unstable and stable Taylor cone by loading two polymer solutions with different NP weight percentages. Voltage was slowly increased until a stable Taylor cone was observed. Nanoparticle-polymer composite solution viscosity was tested using rheometry. Metal oxide nanoparticles (TiO_2, indium oxide (In_2O_3), hematite (Fe_2O_3)) and electrospun polymeric fibers where characterized using transmission

electron microscopy (TEM) and energy dispersive X-ray analysis (EDX). TiO_2 was

chosen because of its widespread use as a photocatalyst and arsenic absorbent, while

In_2O_3 was chosen due to its use in semiconductor industries plus its visual color

observation ability and high sensitivity of morphology using scanning electron

microscopy (SEM) in order to observe NP distribution in the fibers. Fe_2O_3 was chosen

because it is a good adsorbent of inorganic pollutants (such as arsenic) in drinking water.

The results are intended to aid in optimization of electrospinning nano-composites by

showing how adding different NP mass fractions can affect viscosity, voltage, surface

morphology, and diameter of fibers.

3.3 Experimental Methods
Materials

Two polymers (Polyvinylpyrrolidone [PVP] K90 (MW 360,000 g/mol, Fluka

Analytical) and Polystyrene (PS, MW 350,000 g/mol, Aldrich Chemistry)) were used for

electrospinning. These polymers were chosen based on their high molecular weights

suitable for electrospinning. N,n-dimethylformamide (DMF, Sigma-Aldrich) was used as

the organic solvent to dissolve both of the polymers.

Nanoparticles used for loading include indium oxide nanopowder from U.S.

Research Nanomaterials, Inc. (Houston, TX) and Degussa AG Aeroxide P25 TiO_2

(Frankfurt am Main, Germany). Fe_2O_3 NPs were synthesized by modifying a previously

published method [185]. Briefly, anhydrous ferric acid (Sigma-Aldrich) was prepared over

heat in a 4 mM HCl solution and 0.25 M $FeCl_3$ stock. The solution was then placed in a

laboratory oven (HP 5890 series II) at 100°C and incubated for 10 hours. The Fe_2O_3 NPs

were centrifuged and washed five times with nanopure water. After rinsing, the Fe_2O_3 NPs were stored at 4°C.

In$_2$O$_3$-polymer composite, TiO$_2$-polymer composite, and Fe$_2$O$_3$-polymer composite solutions were prepared by dispersing various NP concentrations (0, 0.05, 0.5, and 5 % (m/v)) in DMF by one hour of bath sonication (Branson 2510, Branson Ultrasonic, Dansbury, CT, USA). NP weight percentage loadings (0.05-5 % (m/v)) into the polymers were chosen to span multiple orders of magnitude. Polymer (20 % (m/v) of either PS or PVP) was added to the solution and gently stirred for 24 hours at 40°C.

NPs (Figure 3.1) were analyzed using transmission electron microscopy (TEM) and X-ray Diffraction (XRD). 500 particles of each material were counted by hand using ImageJ [186]. TiO$_2$ NPs averaged 27±7 nm in size, In$_2$O$_3$ NP averaged 80±17 nm, and Fe$_2$O$_3$ averaged 46±3 nm. The XRD reflections of In$_2$O$_3$ NPs are characteristic of phase-pure nanocuboids. TiO$_2$ was mostly anatase. Fe$_2$O$_3$ crystalline phase identification was confirmed by comparing XRD reflections with the pattern of the Joint Committee on Powder diffraction Standards database (see Appendix A, figures A-1 - A-3).
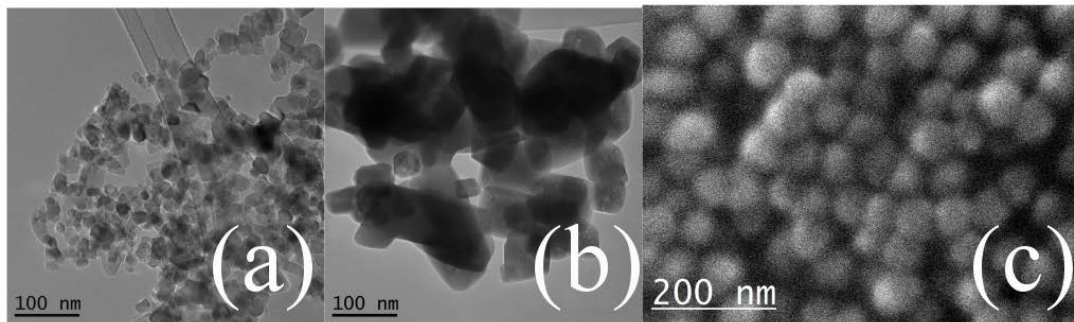
Figure 3.1 TEM Images of Associated Nanomaterials. TEM Images of (a) TiO₂, (b) In₂O₃, and (c) Fe₂O₃ nanoparticles utilized for fiber hybridization.

ELECTROSPINNING. An apparatus similar to previously published electrospinning systems was constructed.[102,160,187–189] Briefly, electrospinning was performed using a high voltage power supply that provided up to 40 kV (Gamma High Voltage, Ormond Beach, FL), a syringe pump (New Era NE-300, Farmingdale, NY), a 10 mL plastic syringe, and a grounded aluminum foil coated collector that was placed 15 cm away from the syringe tip. The experimental procedure involved loading the solution into a plastic 10 mL syringe fitted with a stainless steel needle that was connected to the high voltage power supply. The NP-polymer composite solution was injected at 20 µL/hour through a stainless steel, 22-gauge needle (Sigma-Aldrich stainless steel 304 syringe needle) with an alligator clip attached to charge the needle and the polymer solution as it exited the capillary tip. The entire system was enclosed to mitigate the effects of air currents on the system and for safety. Humidity was measured using a Xikar hygrometer and was maintained at 40% at 75°F using a sponge saturated with deionized water inside the electrospinning enclosure. All experiments were run grouped by metal oxide on the same day in quick succession to maintain similar ambient experimental conditions.

Analytical Methods

Nanoparticles were characterized using a Philips CM200-FEG transmission electron microscope and a Siemens D5000 powder X-ray diffractometer. SEM images of fibers were obtained using a JEOL 2010F. Viscosity of polymer solutions was measured using a TA Instruments AR-G2 rheometer. Fiber diameters were measured using ImageJ software (National Institutes of Health, Washington, D.C., USA).

3.4 Results and Discussion

Effect of nanoparticle addition on critical voltages to produce Taylor cones

Taylor cone formation is an important feature of the electrospinning process because it indicates that the voltage applied affects the surface tension of the solution, and because it is a precursor to a stable, continuous polymer jet. The charged jet is the distinguishing characteristic between electrospinning and electrospraying, where the end result of electrospraying is charged polymer droplets without fiber formation. The critical voltage occurs when the jet forms. Droplet shape at the tip varies with applied voltage. At lower voltages, the originating drop at the capillary tip is larger than the diameter of the capillary tip. As voltage increases, the jet originates first from the bottom of the drop, and then the drop diameter decreases with increasing voltage until the jet emerges from the solution within the syringe tip.[99] Little is known about the dependence of these voltages on NP loadings in polymers.

Figure 3.2 shows critical voltages for In_2O_3 and TiO_2 NPs at different loadings in PS. Figure A-4 in Appendix A shows a companion plot using PVP. For both polymers, the critical voltage did not vary for NP loadings lower than 0.5 % (m/v). The critical voltage needed to produce a Taylor cone without NP in solution was 10 kV. The critical voltage needed to form a stable Taylor cone increased ($p<0.05$, Student's t-test) by roughly 25% when adding up to 5 % (m/v) TiO_2 and In_2O_3 in PS or PVP. The increase in voltage needed to form a Taylor cone may be attributed to increasing viscosity caused by NP addition. Interestingly, there was not a statistical difference ($p<0.05$) between 0.05 %

(m/v) and 0.5 % (m/v) NP to increase critical voltage or polymer solution viscosity. Similar variability has been seen for small weight percentages (0-10 % (m/v) PS NPs) in linear PS chains; the mechanism is yet to be explained.[190]
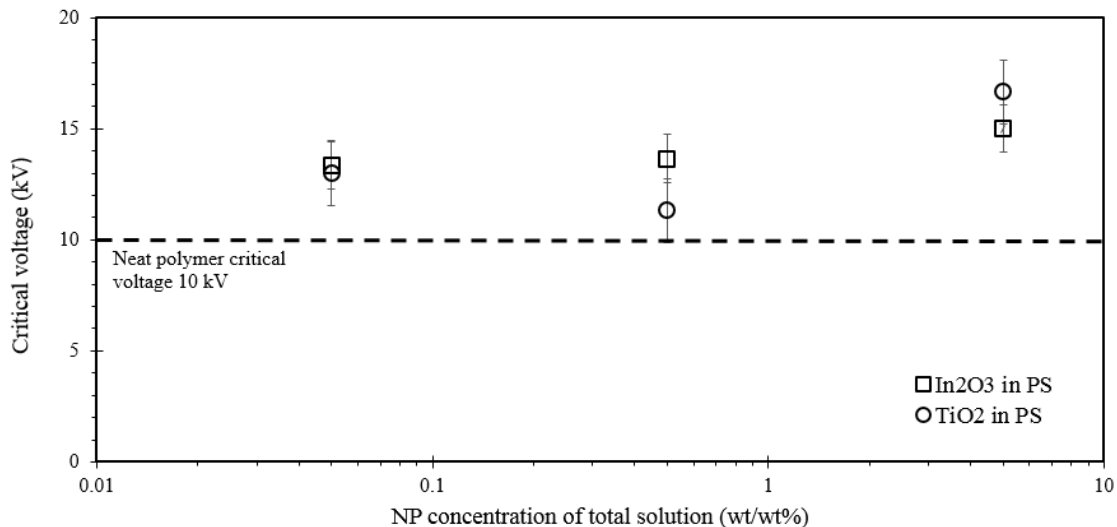
Figure 3.2 Critical Voltage to Produce a Taylor Cone in PS Solutions (for PVP, see A-3).

Solution viscosity can influence the voltage needed to successfully produce a polymer jet in electrospinning and also affect fiber diameter, droplet shape, and jet trajectory.[99,191] Viscosity increased ($p<0.05$, Student's t-test) with higher mass fraction of nanoparticles (Figure 3.3). Increasing solution viscosity requires increased voltage to produce a Taylor cone and a charged jet.[99,103] According to the Einstein-Batchelor law for spherical particle suspensions, adding particles should increase the viscosity of their host polymer.[192,193] However, this is not the case for all NP loadings. Polymer nanocomposites display a variety of unexpected behavior, most notably a reduction in viscosity.[172,190]

47

Reduced viscosity has been observed in PS solutions containing dispersed fullerene and magnetite NPs.[190] This phenomenon has been attributed to a decrease in excluded volume due to a change in polymer conformation; the viscosity of polymer melts do not follow convention when NPs are introduced.[172,190,194]
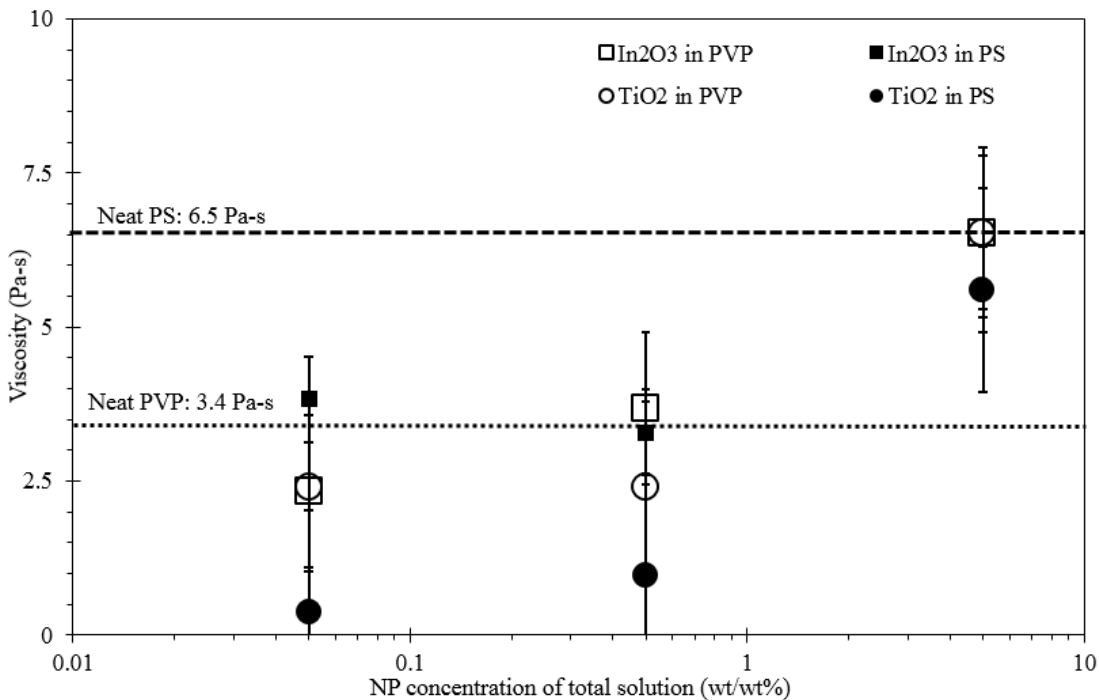
Figure 3.3 Viscosity of PVP and PS Solutions Measured Using a Rheometer.

Morphology of nanoparticle-polymer fibers

      Changes in viscosity are known to affect morphology of electrospun fibers.[102,108,195,196] For example, beading in polymer fibers refers to segments of polymer that are thicker than adjacent elongated fiber. Beading is usually round in nature, much like pearls on a necklace (Figure 3.5). Beads form in electrospun fibers due to the competition between capillary forces and electrical stress.[197] Polymer molecular weight

48

and solution concentration have been linked to beading and branching in electrospun fibers by causing increases in solution viscosity and surface tension.[99,103,198] Fibers spun without added NPs are smooth fibers, with constant diameter thickness, and show no beading (Figure 3.4). In contrast, fiber morphologies with 0.05 % (m/v), 0.5 % (m/v), and 5 % (m/v) mass fractions of In_2O_3 and TiO_2 shown in Figure 3.4 are not continuous fibers like those spun without NP; the NP-polymer fibers show beading and branching. These morphology changes reflect the changes in solution composition. Generally, increases in solution viscosity will cause increases in beading and other defects in electrospun fibers.[14,199] In this case, the beading observed is not detrimental for the purposes of this study.

In₂O₃ in PS TiO₂ in PS

No NP

0.05 % (m/v) NP
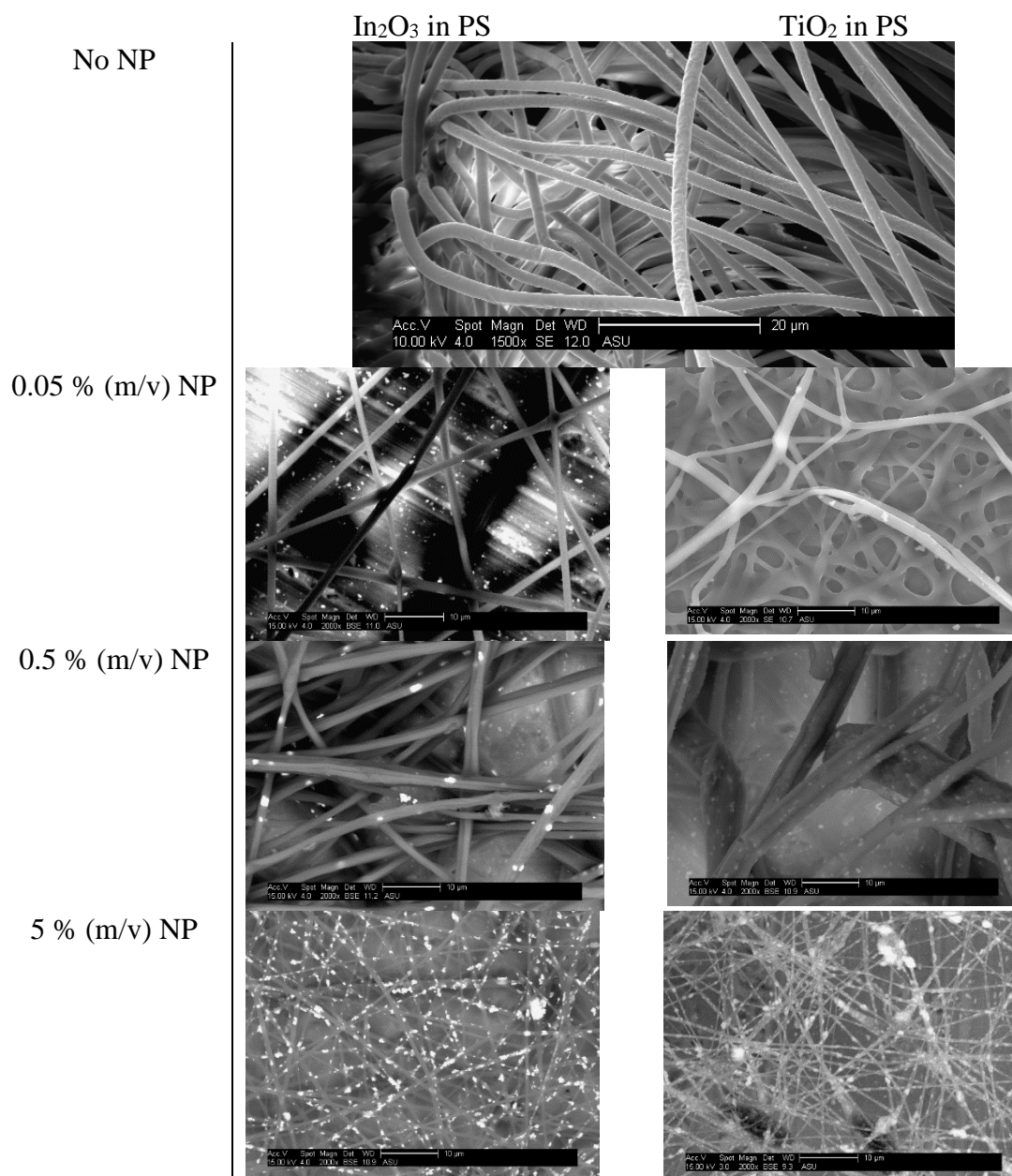
0.5 % (m/v) NP

5 % (m/v) NP

Figure 3.4 SEM Images of PS Fibers with In₂O₃ and TiO₂.

With NP addition, fiber diameter remained constant between 1 and 3 µm (Table

3.1). PVP solutions with no NPs had a diameter of 1.6 µm, increasing by a few microns

with the addition of 0.05 % (m/v) NPs, then decreasing by roughly half with the addition

of 0.5 % (m/v) and 5 % (m/v) NPs. For PS, fiber diameter was 0.8 µm without any NPs, which is consistent with the higher viscosity of PS. The PS fiber diameters double with the addition of 0.05 % (m/v) and 0.5 % (m/v) NPs. However, with the addition of 5 % (m/v) NP, diameter decreased in size by roughly half ($p < 0.05$, Student's t-test). Based upon what is known about spinning solutions with higher viscosity and surface tension, we believe a variation in fiber diameter of polymer solutions containing NPs was caused by the increased voltage needed to form a charged jet.[102,110,188]

Table 3.1 Effect of NP Loading and Polymer on Electrospun Fiber Diameter.

Sample	Fiber Diameter (µm ±1 SD)			
	No NP	0.05 % (m/v) NP	0.5 % (m/v) NP	5 % (m/v) NP
In_2O_3 in PVP	1.6±0.25	1.93±0.53	0.59±0.15	0.81±0.23
TiO_2 in PVP	1.6±0.25	1.75±0.41	0.68±0.20	0.83±0.35
In_2O_3 in PS	0.81±0.20	1.9±0.43	1.8±0.52	0.82±0.20
TiO_2 in PS	0.81±0.20	1.45±0.53	3.8±1.8	0.72±0.48

Distribution of NPs in electrospun fibers

The distribution of NPs in fibers becomes important for certain applications, for example, when NPs in fiber function as reactive sites for sorbents.[166] In order for nanocomposite electrospun fibers to be useful, NPs must be readily accessible.[14] Figures 3.4 through 3.6 show NP distributions in the fibers. The 5 % (m/v) NP-polymer solutions shown in Figure 3.4 are the best example of desirable distribution of NPs obtained in this study. Nanoparticle aggregates were counted manually inside 10 µm² areas using TEM images like those found in Figure 3.4 (n=500 aggregates). The 5 % (m/v) In_2O_3 shows the most uniform distribution, with an average of 6±2 NP cluster/10 µm² area, versus 4±1 cluster/10 µm² area for 5 % (m/v) TiO_2. EDX analysis confirmed indium and titanium presence in electrospun fibers observed utilizing backscatter SEM imaging (Figure 3.5). Figure 3.5 also shows magnified images of PVP fibers with 1 % (m/v) In_2O_3 added, which formed both polymer beads and aggregated In_2O_3 beads. NP aggregations may occur due to polymer-nanoparticle interactions, as well as electrostatic forces between the nanoparticles themselves. NP distributions in polymers are not well understood; this is due to a lack of theoretical studies, systematic experimental results, and the challenges of

processing nanocomposites.[200] Existing literature reports suggest a lack in consensus on a single quantitative method for the evaluation of the state of dispersion of nanoparticles in suspensions. Khare et al. (2010) proposed a method for obtaining free space length (L_f).[201] L_f is described as the characteristic size of unreinforced polymer domains within nanoparticle suspensions. By quantifying the size of these unreinforced particle domains, dispersion states can be distinguished between polymer suspensions. L_f is reduced as a product of more uniform dispersion, decreasing particle size, and increased nanoparticle loading.[201] The L_f of a 5% TiO_2 suspension before and after spinning was found using the TEM images shown in Figure 3.6 in accordance with the previously published method[201]. The L_f of 5% TiO_2 in PS before spinning was 161±16 nm, while that of 5% TiO_2 in PS after spinning was 155±6 nm. Changes in the state of dispersion of NPs can influence electrospinning performance; in this case, the state of dispersion of the TiO_2 suspensions in polystyrene was similar before and after spinning despite the method of data interpretation.

Element	Wt%	At%
CK	87.64	90.42
OK	12.36	09.58
Matrix	Correction	ZAF

Element	Wt%	At%
CK	25.62	63.77
OK	10.48	19.59
InL	63.89	16.64
Matrix	Correction	ZAF
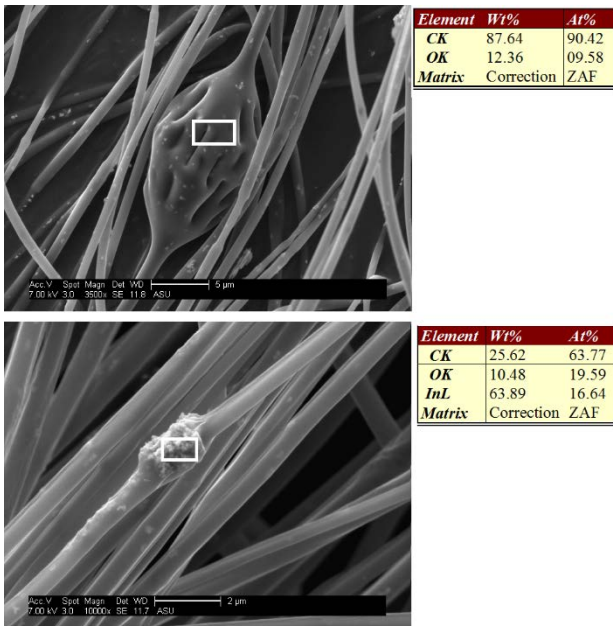
Figure 3.5 Images of 1 % (m/v) In_2O_3 in PVP. Beading is common in electrospun fibers.
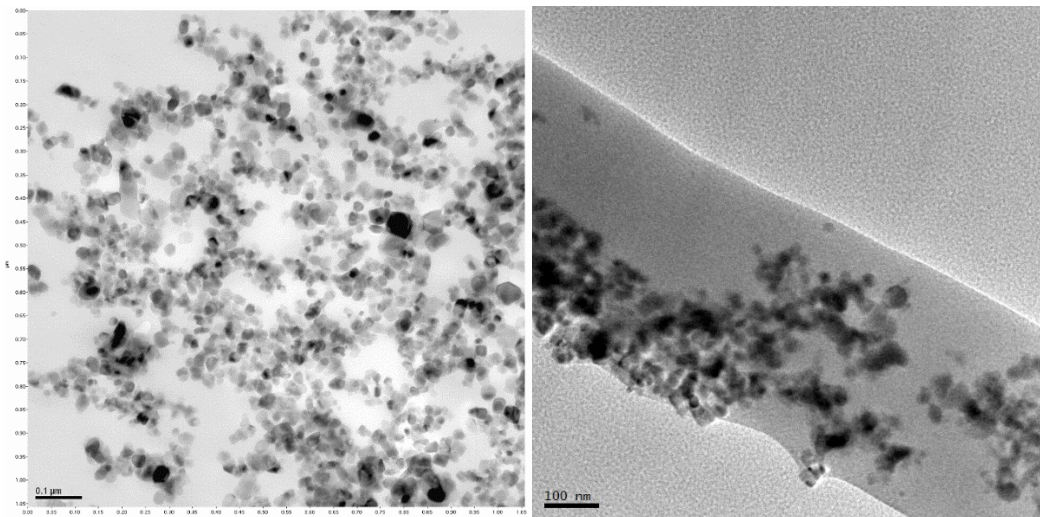
Figure 3.6 5% TiO_2 in PS before electrospinning (left) and after electrospinning (right).

In addition to assessing the state of dispersion of 5% TiO_2 in PS, the particle size distributions of this suspension were evaluated. Particles were manually counted and measured using ImageJ (n=500 particles). Figure 3.7 shows the particle sizes distributions for loose TiO_2 NPs, 5% TiO_2 in PS prior to spinning, and 5% TiO_2 in PS after spinning. The figure indicates that between the three phases of the experiment the NPs were in the 10-20 nm range in size and could not exert effects on nanoparticle dispersion or electrospinning performance by changing diameter. Coupled with the uniformity of state of dispersion throughout the experiment, these results indicate little to no influence on electrospinning performance by interactions of nanoparticles with the polymer matrix or within the nanoparticle aggregates. The nanoparticles formed aggregates as soon as they were suspended, despite sonication, and maintained their state through the experiment.
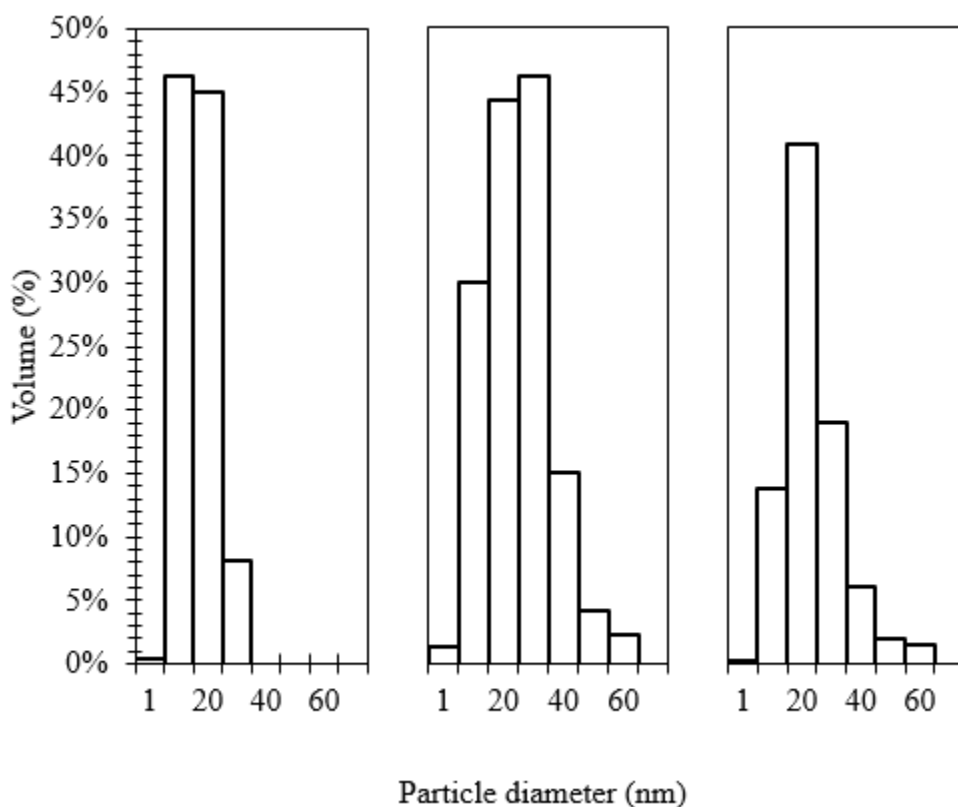
Figure 3.7 Particle Size Distributions (n=500) of TiO$_2$ NP for (left to right) loose TiO$_2$ particles, 5% TiO$_2$ in PS suspension prior to spinning, and 5% TiO$_2$ in PS suspension after spinning.

Figure 3.8 shows SEM magnifications of Fe$_2$O$_3$ in PS. Fe$_2$O$_3$ NPs were added to PS solution for comparison against TiO$_2$ and In$_2$O$_3$. Electrospinning is based on the manipulation of charge. Nanoscale Fe$_2$O$_3$ is highly conductive, displays behavior unique to nanoparticles, and may behave differently in the electrospinning system. Similar with TiO$_2$ and In$_2$O$_3$, the Fe$_2$O$_3$ nanoparticles are discernible at 0.5 % (m/v) in the fiber, and are well distributed through the polymer filament.
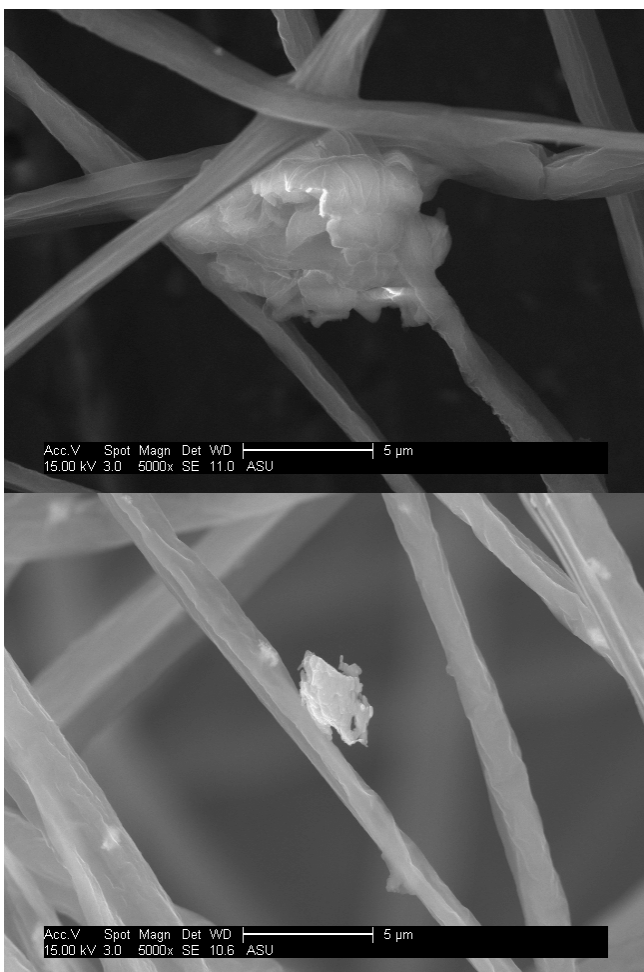
Figure 3.8 Fe₂O₃ in PS. 0.05 % (m/v) (top) and 0.5 % (m/v) Fe₂O₃ (bottom).

Demonstration of adsorption by a TiO₂-PS composite fiber

A motivation for the experiments detailed in this paper was to effectively harness

the potential benefits of suspending nanoparticles such as TiO_2 in a polymer scaffold in

order to facilitate their use as active sites for remediation processes, such as adsorption.

The aim was to make a hybrid NP-polymer fiber in a single step, without post-treatment

(e.g., attachment of NP after spinning a polymer fiber, calcination of a non-polymeric

metal sol). Our control experiments with TiO_2 alone in water confirmed literature reports

demonstrating its ability to remove As(V).[202] Therefore, a single-point arsenate (As(V)) adsorption experiment was conducted using a hybrid NP-polymeric fiber created from a dispersion of 5 % (m/v) TiO_2 in polystyrene and DMF. With the incorporation of TiO_2 in the fiber, sorption of As(V) was expected; however, upon experimentation, no As(V) sorbed onto the composite fiber. We hypothesized that while TiO_2 is well dispersed in the polymeric fiber, the fiber was smooth and all measurements indicated that it was non-porous. Separately, recent work (Hoogesteijn von Reitzenstein et al, in prep) shows that dispersing graphene platelets in PS/DMF prior to electrospinning created fibers with surface porosity. These pores provide access points between the aqueous phase and the graphene embedded within the polymeric fibers. Therefore, we spun a hybrid NP-polymeric fiber by dispersing both TiO_2 and graphene together in PS/DMF. The resulting fibers are porous (Figure 3.9), but did not adsorb As(V). To prove the porosity could allow sorption of pollutants by NPs within the polymeric fiber adsorption experiments using a non-polar organic pollutant (phenanthrene ($C_{14}H_{10}$)) confirmed >50 times more adsorption on the hybrid fiber than a polymer-only (control) fiber (no NP). The phenanthrene sorption, on a mass removal basis (mg phenanthrene per g graphene) is equivalent between a dispersion of graphene in water (no fiber) and the hybrid NP-polymer fiber, thus proving the organic pollutant adsorbs only to the graphene and that the graphene NP surface is available within the pores of the fiber for phenanthrene. We suspect that the lack of As(V) sorption in the hybrid TiO_2/graphene-polymer fiber was not due to the lack of pore formation but rather that the polymer still encompassed the TiO_2 NP within the fiber. A way to create pores and allow connectivity between As(V) in

58

water and TiO_2 could be to use new TiO_2-graphene nanoparticles. Multifunctional TiO_2-graphene composite nanomaterials have been synthesized with TiO_2 encapsulated within crumpled graphene sheets.[203,204] These types of materials may provide a one-step method to synthesize water-stable hybrid NP-polymeric fibers and non-woven textiles capable of pollutant removal from water.
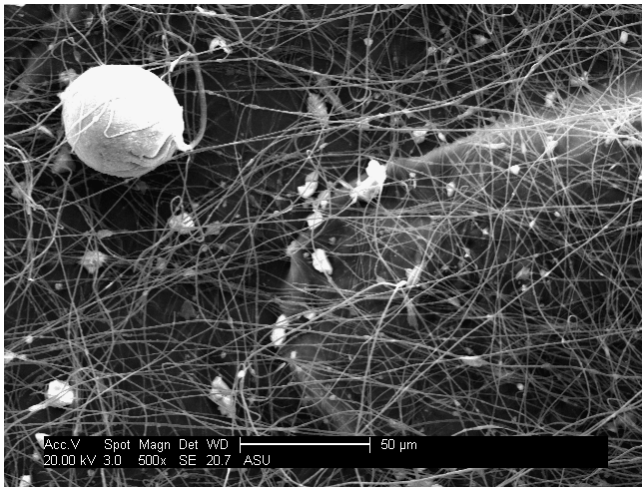
Figure 3.9 TiO_2-Graphene PS Fiber Bead. SEM image of a 5 % (m/v) TiO_2-1 % (m/v) graphene platelet PS fiber bead.
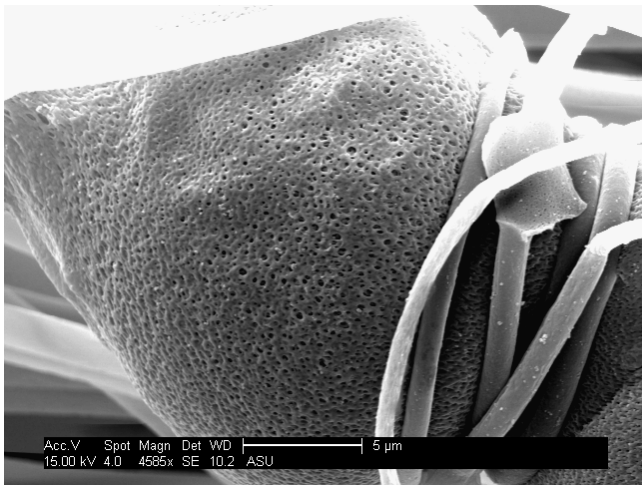
Figure 3.10 Graphene PS Fiber. SEM image of a 5 % (m/v) graphene platelet PS fiber.. Pores are clearly visible.

3.5 Summary & Conclusions

- Effect of 0-5% (w/v) metal oxide NP (TiO_2, In_2O_3) addition to PS fibers on viscosity, critical voltage, and fiber morphology was investigated;

- Viscosity and critical voltage increased with increasing weight percentage of NP in polymer solution;

- Critical voltage needed to produce Taylor cone was higher for PS than for PVP;

- A 50% increase in fiber diameter for 5% (w/v) was observed as a result of increased viscosity and surface tension; otherwise no significant differences observed;

- Even distribution of NP in fibers was observed.

Research Question 1:

Do metal oxide nanoparticle loadings at 0.05, 0.5, and 5% (m/v) increase electrospinning solution viscosity, increase voltage required to observe a Taylor cone, or increase electrospun fiber diameter?

Hypothesis 1:

Adding nanomaterials of any quantity will increase solution viscosity, therefore requiring higher voltage and resulting in larger fiber diameters than neat polymer fibers.

This project began with the construction of an electrospinning apparatus from various components due to cost restraints, as opposed to purchasing a conventional electrospinning device built specifically for this purpose. Once the electrospinning apparatus setup and wiring was complete, various polymers and organic solvents were tested in different ratios in order to produce a continuous fiber. Two solutions, one of 20% (w/v) of PS in DMF and the other 20% (w/v) PVP in DMF, were chosen as the polymeric scaffold material. Next, nanomaterials were added in different mass ratios (based on polymer content) in order to observe the effect of nanomaterial loading. *Hypothesis 1 was partially confirmed* when nanomaterial dispersions above 5% (w/v) in both PS and PVP showed increased viscosity and required higher critical voltage to produce a Taylor cone. Fiber diameter decreased with increasing nanomaterial loading as a product of increased viscosity and surface tension in the charged jet during fiber spinning. Nanomaterial distribution was conserved throughout the spinning process.

Research Question 2:

Can metal oxide nanomaterials be incorporated into electrospun fibers without post-spinning treatment to enable arsenate adsorption by the composite nanofiber?

Hypothesis 2:

The use of volatile organic solvents, such as Dimethylformamide (DMF), will induce a fiber surface porosity which will provide access points for target contaminants, such as Arsenic, to be removed from aqueous solution via nanosorbents (TiO_2) embedded in the fiber.

A TiO_2-PS fiber was tested as a sorbent for arsenic. The fiber failed to adsorb Arsenic, leading to the conclusion that the material was not porous, therefore *rejecting Hypothesis 2*. This project led to the conclusion that, although nanomaterials could be successfully incorporated into electrospun fibers, the fiber would not necessarily be porous enough to provide access points between a pollutant in an aqueous matrix and the reactive nanomaterial inside. Thus, an investigation into methods of increasing the porosity of electrospun fibers began.

CHAPTER 4

SUPERFINE POWDERED ACTIVATED CARBON INCORPORATED INTO ELECTROSPUN POLYSTYRENE FIBERS PRESERVE ADSORPTION CAPACITY

Von Reitzenstein contribution: 50% ideation, 50% experimental, 20% written.

4.1 Abstract

A composite material consisted of superfine powdered activated carbon (SPAC) and fibrous polystyrene (PS) was fabricated for the first time by electrospinning. SPAC is produced by pulverizing PAC. The diameter of SPAC (100–400 nm) is more than one hundred times smaller than conventional powdered activated carbon, but it maintains the internal pore structure based on organic micropollutant adsorption isotherms and specific surface area measurements. Co-spinning SPAC into PS fibers increased specific surface area from 6 m^2/g to 43 m^2/g. Unlike metal oxide nanoparticles, which are non-accessible for sorption from solution, electrospinning with SPAC created porous fibers. Composite SPAC-PS electrospun fibers, containing only 10% SPAC, had 30% greater phenanthrene sorption (based on average adsorption capacity) compared against PS fibers alone. SPAC particles embedded within the polymer were either partially or fully incorporated, and the accessibility of terminal adsorption sites were conserved. Conserving the adsorptive functionality of SPAC particles in electrospun non-woven polymeric fiber scaffolding

can enable their application in environmental applications such as drinking water

treatment.

4.2 Introduction

Electrospun non-woven polymeric fibers have a great potential for application in a multitude of areas including biomedicine, textile, electronics, optics and environmental remediation.[110,205] Fibrous structure of non-woven fabrics provide scaffolding advantages with tunable surface properties as well as high air and water permeability. In addition, electrospinning allows integration of functional nano- and submicro-sized particles to the fibrous macrostructure that can be applied in drinking water treatment. Providing access to clean water and maintaining the growing needs for quality and quantity is a National Academy of Engineering Grand Challenge that requires innovation and new strategies to treat water.[206] Activated carbon adsorption is an existing best available technology capable of removing a broad spectrum of organic micropollutants.[31] Recently, superfine powdered activated carbon (SPAC), which is activated carbon pulverized to sub-micron sizes, is gaining attention because of its favorable inherent properties as an adsorbent including very fine particle size, high porosity and large specific surface area.[207–209] SPAC enables high adsorption capacity and fast adsorption kinetics because of its small size. Smaller SPAC particles contain a simpler inner pore structure, which subdues competition between natural organic matter and organic pollutants.[207,208] However, it can be operationally challenging to settle SPAC from flowing water due to its small particle size and low density. As such, incorporating SPAC particles into a superior macroscale structure that preserves rapid adsorptive properties of SPAC would be desirable for treating water in large basins or as non-woven fabric reactor designs.

To create such a macroscale structure, composite sorbent was fabricated by co-spinning SPAC and polystyrene (PS), and a composite electrospun non-woven fabric matrix was produced. Electrospinning is a scalable, and cost-effective nano-fabrication method.[110,210,211] Electrospinning uses an electrically charged jet of polymer solution to produce polymer filaments by applying a high electrical potential difference (i.e., 10–40 kV). The surface tension on the fluid droplet at the tip of the syringe is overcome by the strength of the electric field, and a charged jet of fluid stretches and deposits onto the grounded collector, forming a layer of fibers with diameters in the micro- and nanometer scale. These fibers can be used in non-woven fabrics without post-treatment for a range of applications. To date, nano-additives including metal oxides,[11] single- and multi-walled carbon nanotubes,[199,212–214] graphene,[215,216] and graphene oxide[210] have been embedded as additives to enhance the mechanical, electrical and thermal stability of the electrospun fibers.[216]

In this study, we aim to demonstrate incorporation of porous SPAC particles into electrospun polymeric matrices in a single step without post-treatment while preserving accessibility to SPAC's inner pore network. This novel material is demonstrated to remove organic pollutants from water when embedded in a polymeric fiber. SPAC particles were produced from parent powdered activated carbon via wet milling and then incorporated into PS via electrospinning. To the best of our knowledge, there is no previous literature related to incorporating SPAC particles into electrospun polymeric matrices. Freely suspended SPAC particles were tested side-by-side with SPAC-PS composite sorbents for nitrogen gas and phenanthrene (PNT) adsorption.

4.3 Experimental Methods

Preparation of Superfine Powdered Activated Carbon (SPAC) by Wet Milling

Previous work with SPAC characterization was used to guide selection of bulk powdered activated carbon.[208] Coal-based powdered activated carbon (PAC, WaterCarb-800) obtained from Standard Purification (Palm Beach Gardens, FL) was pulverized to sub-micron particle size via wet bead milling. The pulverization was conducted by a Netzsch Premier Technologies LLC (Exton, PA) MiniCer Horizontal Bead Mill using 0.5 mm steel beads as grinding media. The milling chamber was 85% full of beads. An aliquot of 200 grams parent PAC was suspended in about 800 grams of deionized water, with additional water (a few hundred grams) added incrementally to decrease viscosity during milling. The slurry was recirculated through the machine for a total milling time of seven hours, with an agitator speed of 3935 rpm. SPAC-slurry was dried overnight in a vacuum oven at 105 °C.

Characterization of Superfine Powdered Activated Carbon (SPAC)

Specific surface area measurements were conducted with 30 mg of material degassed for ~18 hours at 60 or 300 °C prior to nitrogen gas adsorption experiments. Lower temperature (i.e., 60 ^{0}C) was selected for polymer-containing samples to prevent structural losses via thermal decomposition. Nitrogen adsorption at 77 K was performed with a physisorption analyzer (Micromeritics ASAP 2020). The Brunauer-Emmett-Teller (BET) equation was used to calculate surface areas from nitrogen gas adsorption isotherms. The density functional theory (DFT) model was used to calculate the pore size

distribution. Total pore volume (V_T) was calculated from single point adsorption capacity at $P/P_0 = 0.99$.

Elemental analysis was performed using a Flash Elemental Analyzer 1112 series (Thermo Electron Corporation). Sizes for particles less than 6 µm in diameter were measured using dynamic light scattering (DLS) with a Zetasizer NanoZS (Malvern, Worcestershire, UK). Readings were taken in distilled water after bath sonication, and z-avg hydrodynamic diameters are reported. Particles larger than 6 µm were measured by optical microscopy imaging using a Zeiss Axioskop 2 Plus optical microscope with a Zeiss AxioCam MRc5 camera attachment running AxioVision AC version 4.2 software. Particles were sonicated before imaging, and Zeiss Immersionsol 518C immersion oil was used to view the particles at 40x magnification. The images were processed using ImageJ, an image processing software (Schneider et al., 2012), to determine the average diameter of the particles.

pH_{PZC} in the bulk material was measured by a pH drift method where the point of zero charge is defined as the pH where no drift occurs after 48 hours. For each pH point and carbon, 100 mg of dry SPAC was added to 20 mL of pH adjusted 0.1 M NaCl in a CO_2-free background. After a minimum of 48 hours on a shaker table, pH was measured in each vial and compared to a no-carbon blank.[208]

Fabrication of SPAC-PS Composite Material

Pristine PS pellets (MW 350,000 g/mol) and organic solvent (N,n-dimethylformamide, DMF) were purchased from Sigma-Aldrich (St. Louis, MO). SPAC-PS composite sorbents were prepared by dispersing 5% (m/v) of SPAC in DMF by bath

sonication (Branson 2510, Branson Ultrasonic, Danbury, CT, USA). SPAC was weighed on a laboratory scale and poured from a plastic weigh boat into a 40 mL borosilicate glass vial with a Teflon-lined septa screw cap. An aliquot of 10 mL of DMF was then added to the SPAC inside the glass vial. The SPAC and the DMF were sonicated for one hour in a bath sonicator. Finally, PS was weighed on a laboratory scale and mixed with the SPAC/DMF suspension. A small magnetic stirrer was added to the vial, and the vial was set on a heated stir plate at 300 rpm for 24 hours at 55 °C. Polystyrene was added last to avoid its gelation when contacted SPAC in the sonicator. Bath sonication was used to minimize SPAC aggregation.

An electrospinning apparatus (see Figure B-1 in Appendix B for a schematic diagram) similar to previously published electrospinning systems was utilized for fabricating neat (i.e., pristine with no additives) and composite fibers.[102,160,187–189] Following our previously published procedure, electrospinning was performed using a high voltage power supply that provided 40 kV (Gamma High Voltage, Ormond Beach, FL), a syringe pump (New Era NE-300, Farmingdale, NY), a 10 mL plastic syringe, and a grounded aluminum foil coated collector that was placed 15 cm away from the syringe tip.[11] The SPAC-PS suspension was placed into a plastic 10 mL syringe fitted with a stainless steel needle that was connected to the high voltage power supply. The polymer suspension was injected at 1 mL/hour through a stainless steel, 22-gauge needle (Sigma-Aldrich stainless steel 304 syringe needle). An alligator clip was attached to the needle to charge the polymer solution as it exited the capillary tip. The entire system was enclosed

to mitigate the effects of air currents on the system. The humidity of the electrospinning

chamber was between 20-22% as relative humidity. Ambient temperature was $22\pm1\ ^0C$.

Visual and Microanalysis Characterization of SPAC-PS Composite Fibers

Visual characterization of the media was conducted via high resolution

transmission electron microscopy (HR-TEM) and scanning electron microscopy (SEM).

TEM was used to locate the graphitic allotropes of SPAC particles within the polymeric

matrix. For TEM imaging: the powdered SPACs (~0.125 grams each) were suspended in

40 mL of NanoPure™ water and sonicated for 30 minutes to disperse particles. The

solution (~20 µL) was pipetted onto a TedPella carbon type B, 200 mesh copper TEM

grid and allowed to dry overnight. The PS and SPAC-PS composite fibers were brushed

lightly against a TedPella carbon type B, 200 mesh copper TEM grid allowing the fibers

to electrostatically adhere to the TEM grid. Microscopy was performed on a Philips

CM200 TEM equipped with energy-dispersive X-ray spectroscopy (EDS) for elemental

analysis. Particle and fiber sizing was performed using ImageJ (Schneider et al., 2012).

The scale bar was used to set the scale for calculating the width of each particle and fiber

using ImageJ software.

SEM was used to characterize the fibrous structure of electrospun fiber and the

distribution of SPAC particles. Samples were mounted on stainless steel stubs on carbon

tape and sputter coated (Pt-Au) for SEM imaging. SEM micrographs were obtained using

a JEOL 2010F. The SEM images were processed using ImageJ software to determine the

average particle diameter.

The XRF measurements were performed to characterize the elemental composition of PS pellets, neat PS fibers and PS-SPAC composite fibers. A handheld X-Ray Fluorescence device (Niton XL3t GOLDD+, Thermo Fisher Scientific) equipped with an Ag anode (6 - 50 kV, 0 - 200 µA, 10mm spot size) and Silicon Drift Detector was used to analyze samples. Four proprietary primary filters, with a measurement time of 60 seconds each, allow for analysis of Mg – U elements. The filters optimize excitation energies in four ranges, reducing spectral background under analyte lines, to selectively filter primary X-Rays from the tube. The portable XRF directly reports concentration of elements and error (i.e., two standard deviation).

Surface contact angle measurements were conducted to test the hydrophobicity of the surfaces. Spun fiber samples were pressed into 10-20 mm^2 flat surfaces to increase uniformity and consistency of measurements. Samples were analyzed by sessile water drop method using a Theta Optical Tensiometer TL100. Water droplet (~5 µL) of nanopure water was dropped on each pellet and approximately 300 measurements were taken from the equilibrated water-surface interface within 20 seconds via a high definition camera. Each sample was analyzed in triplicates.

Programmable Thermal Analysis (PTA) analysis was performed to quantify the mass of SPAC in electrospun PS matrix.[217] Samples (3 mg) were placed in a beaker, and 10 mL chloroform and 5 mL hexafluoro-2-propanol were added. The top of the beaker was covered with aluminum foil, and samples were agitated mixed for 5 min. The solid residue was collected by syringe filter on quartz fiber filter after the polymer completely dissolves. Each sample was preheated for 400 seconds under inert conditions (100% He)

to remove volatile organic carbon. Sample chamber was then switched to oxidizing conditions (90% He and 10% O) and thermos-gravimetric analysis was performed. The moisture contents of fibers were calculated by the weight difference of samples after 48 hour residence in 90^0C drying oven.

Phenanthrene Adsorption Experiments under pseudo-Equilibrium Conditions

To assess the adsorption capacity of neat PS, SPAC-PS and SPAC powder, constant carbon dose aqueous phase adsorption isotherm experiments with PNT (Sigma-Aldrich; St. Louis, MO) were conducted. PNT is a polycyclic aromatic hydrocarbon classified as a priority pollutant in drinking water by US Environmental Protection Agency. Molecular properties of PNT is tabulated in Table S1. The simple molecular structure (three conjugated benzene rings with a planar configuration) allows the analysis of intermolecular interactions between PNT molecules and the sorbent surface. The isotherm experiments were designed targeting 20-80% removal of initial PNT concentration based on preliminary adsorption tests. Constant adsorbent doses of 8 and 80 mg/L were used for SPAC powder and fibers (neat PS and SPAC-PS composite), respectively. Concentrated (1000 mg/L) stock solution of PNT was prepared in methanol, and predetermined volumes (between 10 – 125 μL) of the stock solution were spiked to headspace-free 125 mL isotherm bottles sealed with Teflon lined screw caps that contain adsorbent and NanoPure™ water. The ratio of methanol to water was kept below 0.1% (v/v) to eliminate any co-solvent effects on adsorption. The reactors were tumbled for 24 hours to reach pseudo-equilibrium. Preliminary experiments showed that 4-hr contact time is sufficient for PNT and SPAC to reach equilibrium. PNT loss was not observed in

control samples without added sorbents. Aqueous PNT concentrations were measured spectrophotometrically at 250 nm (HACH DR3000). Non-linear Freundlich isotherm model was employed to fit the experimental data and describe the isotherms (see SI in Appendix B for detailed description).

4.4 Results & Discussion

Preparation of Superfine Powdered Activated Carbon (SPAC) by Wet Milling

Wet milling crushed PAC into superfine particles smaller than 1 µm. Table 1 summarizes selected physicochemical characteristics of PAC before and after wet milling. The mean particle diameter decreased by two orders of magnitude to 200 nm. The specific surface area and total pore volume also decreased (i.e., 24% and 38%, respectively). There was a notable shift in pore size distribution from primarily microporous (<2 nm) to primarily macroporous (>50 nm). This indicates that the porous network was altered after wet milling. Reductions in surface area and total pore volume were attributed to destruction or blockage of pores during crushing. The oxygen content on the surface increased from ~3% to 11%, suggesting surface oxidation. This rationale is further supported by the decrease in pH_{pzc} by 1.1 pH units—presumably associated with acidic oxygen containing functional groups (e.g., hydroxyl, carboxyl, carbonyl, phenols, enols, lactones, quinones).[218] Presence of oxygen containing functional groups can influence the adsorption of organic contaminants by changing electrostatic interactions with ionic adsorbates and increasing water cluster formation on the adsorbent surfaces. Partlan et al. (2016) recently reported effects of wet bead milling on physicochemical

properties of PAC.[208] The observations of our study such as the shift in pore size distribution and the increase in oxygen content align well with their findings where they postulated that high level of friction and oxidizing conditions during milling at the SPAC surface.
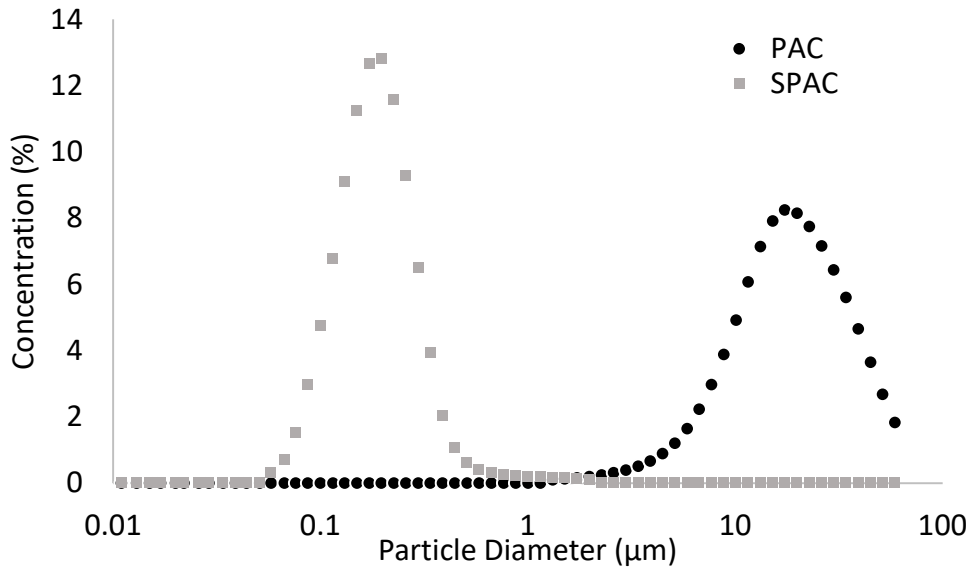
Figure 4.1 Particle Size Distribution of PAC (parent material) and SPAC (final product).

Table 4.1 Physicochemical Properties of PAC (Parent Material) and SPAC.

	PAC	SPAC
Mean Particle Diameter (µm)	21	0.2
Specific Surface Area (m^2/g)	713	574
V_T - Total Volume (cm^3/g)	0.5	0.8
micropore (% of V_T)	47	18
mesopore (% of V_T)	31	23
macropore (% of V_T)	22	59
Oxygen Content (%)	2.9	11
pH$_{pzc}$	10	8.9

Fabrication of SPAC-PS Composite Material

SPAC was embedded in the polystyrene matrix by electrospinning SPAC suspension prepared in viscous PS-DMF mixture. Three limitations that must be overcome to successfully incorporate SPAC in electrospinning. First, the fluid SPAC-PS suspension must be viscous enough (larger than 1.2 Poise), but not too viscous (smaller than 20 Poise) so that it could be extruded through a needle tip with the charged jet in an electric field without gravitational interference or forming droplets.[110] Second, the SPAC particles/bundles need to be small and homogeneous enough to be injected without clogging the needle tip (i.e., smaller than the inner diameter of the needle, 412 µm). To achieve this, SPAC was sonicated in DMF for one hour to facilitate dispersion of SPAC aggregates. PS was added last to the SPAC/DMF mixture to avoid gelation in the sonicator. Gentle mixing at elevated temperatures (55 °C) allowed SPAC powder to be suspended and spun successfully at 20 kV and 1 mL/hr pump rate. Lastly, the dielectric properties of the SPAC particles should not interfere with the electric field in the electrospinning apparatus.

75

As illustrated in Figure 4.2, the color of neat electrospun PS was white, and SPAC-PS composite was black. The moisture contents of neat PS and SPAC-PS composite were 0.5 and 1.3 wt.%, respectively. The slight increase in the moisture content of the composite was attributed to 7.2 wt.% moisture content of the SPAC powder, which was maintained in the fiber matrix. The integrity and durability of both materials were very similar per visual and manual inspection. The SPAC-PS composite material had a uniform color suggesting a homogeneous distribution of SPAC within the matrix. Manual disintegration of the SPAC-PS composite did not release visible powdered SPAC particles, indicating its relatively strong integrity. Programmable thermal analysis (PTA) detected ~0.1 wt.% and ~10 wt.% elemental carbon mass in the neat PS fiber and the composite SPAC-PS fiber, respectively. PTA analysis was repeated for the same samples after aqueous phase PNT adsorption experiments, and no decrease in SPAC content was detected (see Table B-2), indicating successful integration of SPAC to the composite fiber. The increase in the elemental carbon mass after PNT adsorption may be attributed to pyrolytically generated elemental carbon from a fraction of PNT that did not undergo volatilization during preheating. Therefore, monitoring residual SPAC in the treated water can also be essential to ensure the quality of treated water.
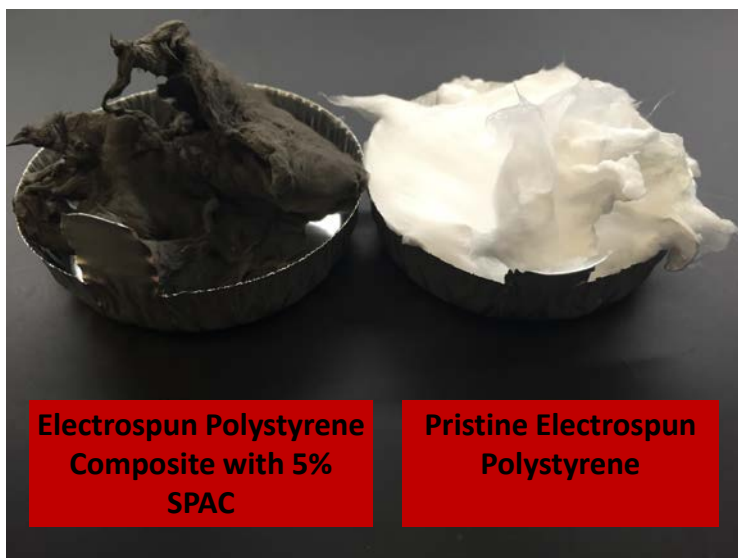
Figure 4.2 Color Difference between Fibers..Neat electrospun PS fibers (on right) and SPAC-PS composite fibers (on left).

Figure 4.3A and 5.3B illustrate representative TEM images of neat PS fiber and SPAC powder, respectively. SPAC has a greater density than PS. As such, SPAC shows black and PS shows light gray on the TEM micrographs. TEM paired with EDS shows the distinct difference between the elemental composition of SPAC powder and the PS fiber. SPAC powder (Figure 4.3B) contains metallic impurities (i.e., iron, magnesium, aluminum, magnesium, silica) unlike neat polystyrene fiber (Figure 4.3A). The metallic impurities were attributed to the addition of SPAC and they were quantified by XRF as presented in Table B-3. The copper detected in all samples was associated with the TEM grids used in the analysis. The SPAC-PS composite samples show that the incorporation of SPAC occurred either by complete encapsulation of carbon particles within the PS fibers (Figure 4.3C) or partial attachment of particles to the PS fiber surface (Figure 4.3D). The elemental EDX analysis of SPAC encapsulated in the fiber or coated on the

surface show identical peaks with SPAC powder, which affirms the integration of SPAC
into the polystyrene matrix.
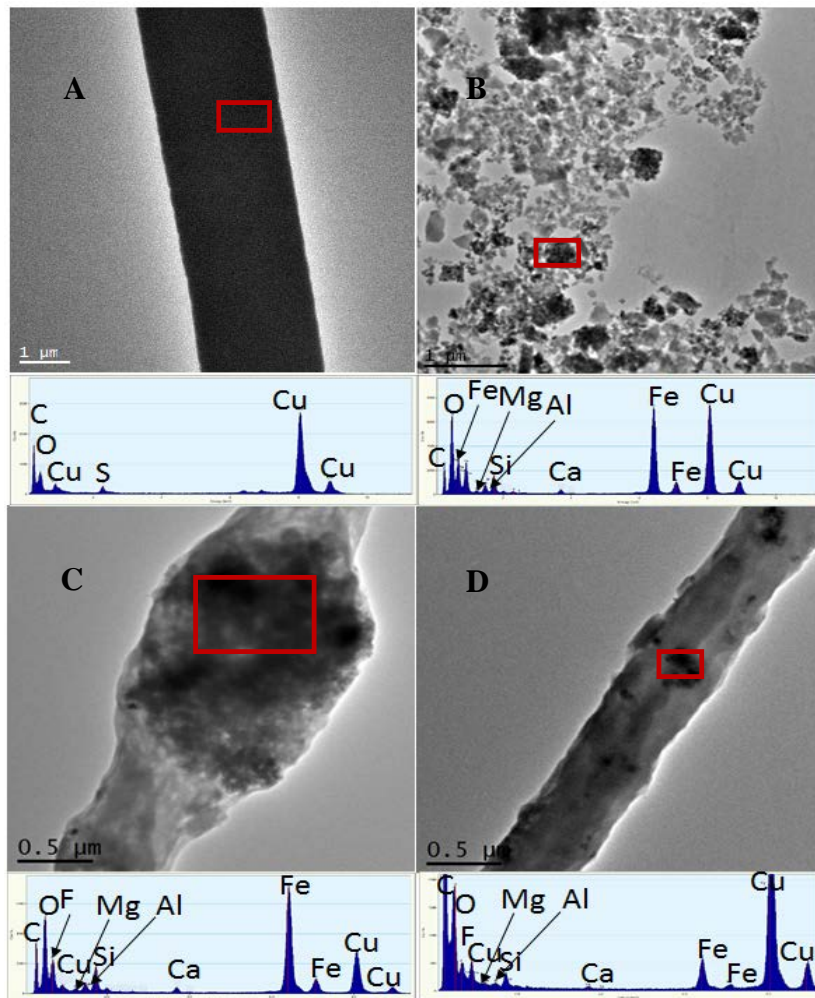
Figure 4.3 TEM Images and Corresponding EDX Analysis of (A): neat electrospun polystyrene, (B): SPAC powder and (C, D): SPAC-PS composite.

The macrostructure of the fibrous material with incorporated SPAC particles is
shown in SEM images (Figure 4.4). The macrostructure maintained its fibrous bundle
structure after SPAC incorporation (Figure 4.4B and 4.4D). The individual fibers also

preserved their shape and morphology such as surface porosity and size. The diameter of

PS fibers with and without SPAC was 0.41 ± 0.39 and 0.52 ± 0.38 μm, respectively;

based on 100 measurements for individual fibers from SEM images via ImageJ. The

close-up images (Figure 4.4A and 4.4B) compare the neat PS and SPAC-PS composite

side-by-side confirming the incorporation of SPAC on the fibrous bundle macrostructure.
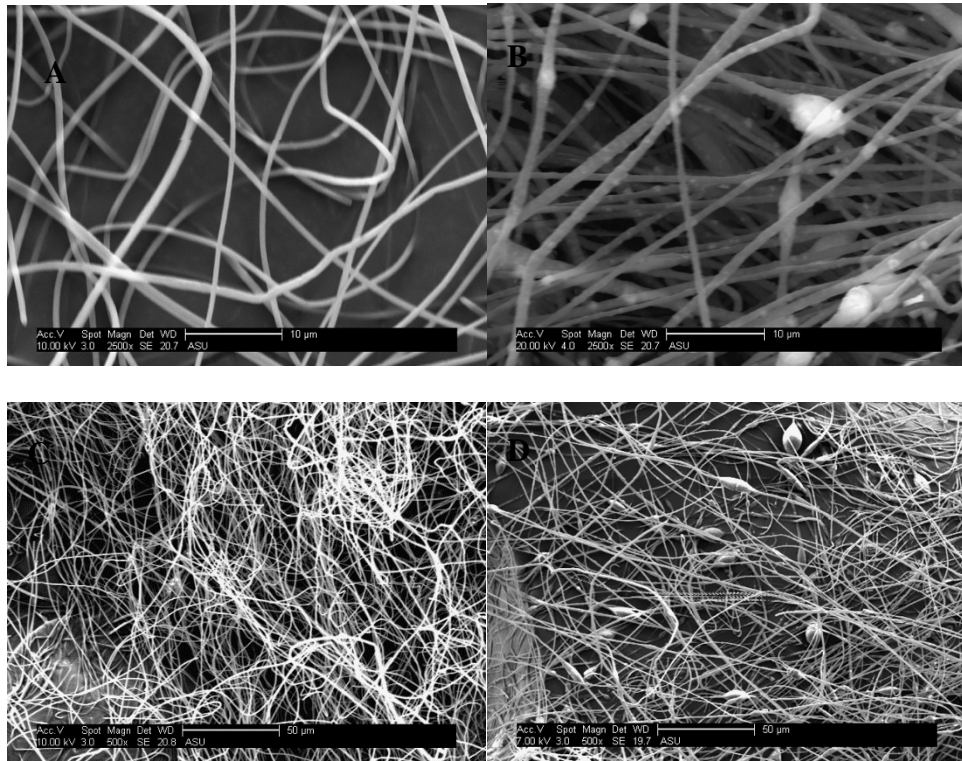
Figure 4.4 SEM Images of PS and SPAC-PS: (A, C): neat electrospun polystyrene, and (B, D): SPAC-PS composite.

The disposition of SPAC particles on polystyrene surface would dictate the

availability of pores. Although some SPAC particles are inside the PS, larger SPAC

particles may be anchored by PS fibers allowing partial exposure of SPAC to the

surrounding aqueous matrix. SPAC is speculated to maintain its porous structure in the

PS matrix, and being dispersed in the polymeric matrix may reveal sorption sites that were not available prior to electrospinning due to aggregation; because, SPAC particles aggregate over time yielding larger bundles (3-7 μm) in water.[219]

Adsorption of Phenanthrene by SPAC-PS Composite Material

Figure 4.5 shows PNT adsorption isotherms and fitted Freundlich equations for SPAC powder, neat PS fiber and SPAC-PS composite. Neat PS demonstrated low adsorption capacity for PNT per dry adsorbent mass. SPAC-PS composite had a considerably higher adsorption capacity for PNT than neat PS at all tested concentrations. This was attributed to higher specific surface area of SPAC-PS composite (43 m^2/g) than neat PS (6 m^2/g) as a result of incorporating porous SPAC particles. The increases in adsorption capacity of SPAC-PS composite validates the accessibility of SPAC's inner pores for sorption of pollutants from water.

$$q_e = 1.13\ C_e^{\ 0.50}$$
$$r^2 = 0.95$$

$$q_e = 0.97\ C_e^{\ 0.39}$$
$$r^2 = 0.81$$

$$q_e = 0.15\ C_e^{\ 0.54}$$
$$r^2 = 0.97$$
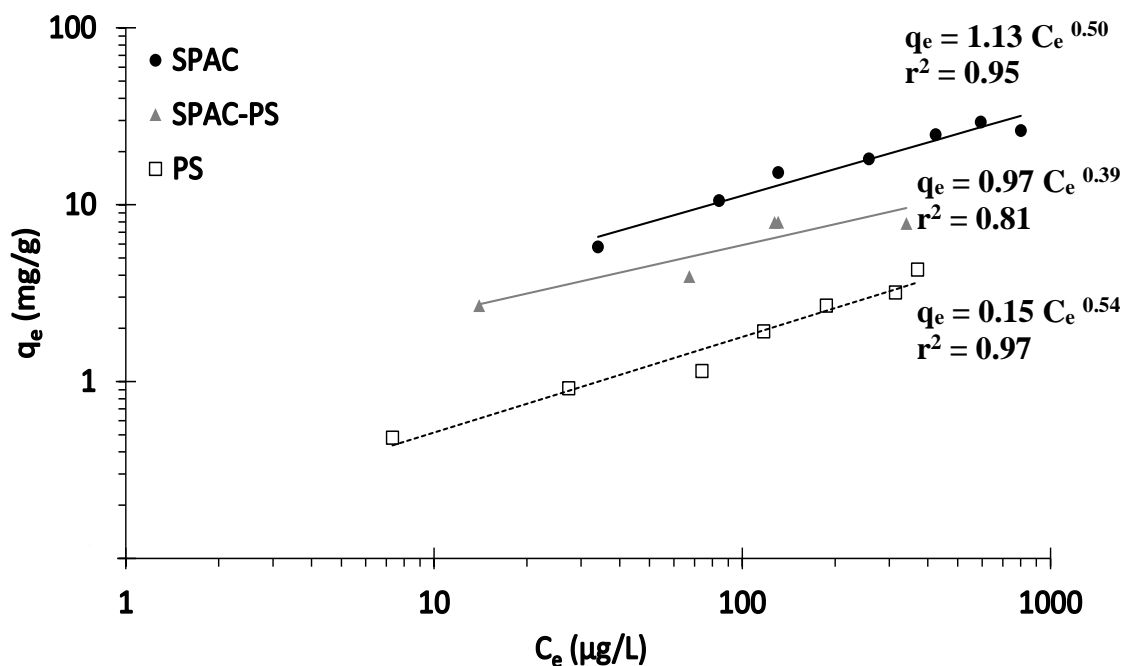
Figure 4.5 Liquid Phase Adsorption Isotherms of Phenanthrene on SPAC alone, SPAC-PS composite and neat PS on dry mass basis. The lines and the equations represent Freundlich model fit.

The SPAC alone has about two folds higher adsorption capacity at saturation concentrations (C_e) between 30 - 300 μg/L than SPAC-PS composite with 10% SPAC based upon PTA measurements, despite the composite containing only a tenth of the SPAC mass. In addition, the SPAC-PS composite showed a slightly lower Freundlich intensity parameter (n) than the SPAC isotherm, indicating more favorable sorption process, which could be attributed to the heterogeneity of sorption sites and sorption energies of the SPAC-PS composite consisted of two materials. The adsorption capacity per mass of adsorbent were in the order of suspended SPAC > SPAC-PS composite > neat PS fiber. Figure B-3 in Appendix B shows the same adsorption data plotted as isotherms normalized to BET specific surface area. In decreasing order, the adsorption

capacity per unit specific surface area were: neat PS fiber > SPAC-PS composite > suspended SPAC. Higher adsorption capacity of neat PS per unit surface area indicates that polycyclic aromatic structure of PS is attracting aromatic PNT molecules via intermolecular attractive forces. This can be attributed to the higher hydrophobicity of neat PS compared to PS-SPAC composite, which was shown by contact angle measurements in Figure B-4 in Appendix B. However, very low specific surface area of the fibers reduced their adsorption capacity as seen for neat PS despite the high hydrophobicity. The disposition of SPAC particles in the bundles of polystyrene fiber depends on the particle size of SPAC as well as the fiber formation and diameter. The particles can be either completely or partially encapsulated by the polymer during electrospinning. Complete encapsulation may inhibit penetration of PNT molecules inside the pores because the polystyrene may occupy or block the accessibility of pores. Alternatively, surface coating may stably disperse the SPAC powder and generate more accessible sorption sites by disintegrating SPAC bundles.

To further investigate the accessibility of inner sorption sites, adsorption capacities for SPAC-PS composite at low and high C_e concentrations (i.e., 40 and 400 µg/L) within the tested isotherm range were calculated from experimental measurements by taking the weighted average of SPAC and PS adsorption capacities (see Figure B-5 and Table B-4 in Appendix B). The calculations take the adsorption capacities of both neat PS fibers and SPAC powder into account using a 90:10 PS:SPAC mass ratio. Individual adsorption capacities were used (i.e., assuming no synergy or hindrance associated with the SPAC and PS interactions). Calculated adsorption capacities

82

($q_{e\_calculated}$) at 40 and 400 µg/L were 2 and 6 mg/g, respectively. The experimental adsorption capacities ($q_{e\_measured}$) at 40 and 400 µg/L were 4 and 10 mg/g, respectively. This improvement in the adsorption capacity of the composite indicates that co-spinning of SPAC and PS have enhanced the adsorption capacity of the materials when evaluated separately. The results suggest that physical and chemical changes of the PS fibers with addition of SPAC and/or the changes in the dispersion state and disposition of SPAC particles in the polymeric matrix (vs. water) compensates for the potential losses and blockages of accessible pores due to encapsulation or partial coating of SPAC surface with polystyrene.

4.5 Summary & Conclusions

- Effect of 5% (w/v) superfine powdered activated carbon (SPAC) addition to polystyrene (PS) electrospun fibers and subsequent performance of fibers as phenanthrene (PNT) sorbent were investigated

- PTA analysis found 10% (w/w) in fiber

- Using neat PS as reference material, SPAC-PS fiber surface area increased six fold (from 6 m^2/g to 43 m^2/g)

- SPAC-PS fibers were found to be porous; accessibility of terminal adsorption sites was conserved

Research Question 3:

Can superfine powdered activated carbon be incorporated into electrospun polystyrene fibers in a single step while preserving accessibility to SPAC's inner pore network?

Hypothesis 3:

Hypothesis 3. SPAC can be incorporated into electrospun polymeric matrices in a single step without post-treatment while preserving accessibility to SPAC's inner pore network.

Hypothesis 3 was confirmed by the porous structure seen in the SEM micrographs of the SPAC-PS composite, and further confirmed by both nitrogen adsorption-desorption experiments coupled with BET surface area modeling and PNT adsorption experiments. The SPAC-PS had six times higher BET surface area than the neat PS fiber and 30% higher adsorption capacity for PNT.

CHAPTER 5

MORPHOLOGY OF POLYMERIC ELECTROSPUN FIBERS CONTAINING MULTI-DIMENSIONAL NANOMATERIALS FOR WATER PURIFICATION

Von Reitzenstein contribution 100% experimental, 95% written.

5.1 Abstract

Carbon nanomaterials (CNMs) present a unique opportunity to tailor nanoscale adsorbents for efficient removal of pollutants from water. Enmeshing CNM sorbents into different macro-scale systems allows a broad range of applications. Electrospinning is a simple method of immobilizing CNMs in a flexible polymer and is used herein to enmesh C_{60} fullerenes, multi-walled carbon nanotubes (MWCNT), and graphene oxide (GO) into polystyrene (PS) fibers in a single-step process. We tested three related hypotheses: 1) the porous nature of hybrid CNM composites leads to increases in diameter, pore size, and number of pores compared to a neat polymer fiber; 2) dimethylformamide (DMF) evaporation from the NM inside the polymer leaves behind inter-connected pores in the solidified polymer; and 3) CNM addition during electrospinning enhances pore formation and improves phenanthrene (PNT) sorption. Separate CNM-PS fibers consisted of $8\pm1\%$ (w/w) MWCNT, $4\pm0.3\%$ (w/w) C_{60}, and $3\pm1\%$ (w/w) GO. The integration of CNMs into fibers increased the fiber diameter but did not change fiber surface pore diameter distribution or number of pores. Pore diameters were 410 ± 390 nm for neat PS, 650 ± 190 nm for MWCNT-PS, 1700 ± 840 for GO-PS, and 1700 ± 870 for C_{60}-PS. We hypothesized that CNM-PS composites would increase sorption of a model hydrophobic pollutant

(PNT) from water. However, sorption was similar using neat PS (q_e=2.9 mg PNT/g sorbent), GO-PS (3.9 mg PNT/g sorbent), MWCNT-PS (2.6 mg PNT/g sorbent), and C_{60}-PS (1.8 mg PNT/g sorbent). PNT removal by PS and CNM-PS fibers occurred due to hydrophobic interactions between PNT and the polymeric fibers. The major finding of this study was that although CNM addition may affect fiber diameter, only incremental benefits were observed in pore diameter, pore number, fiber surface area, or and pollutant adsorption performance. Further advances in fiber synthesis that enable higher CNM loadings in fibers and create continuous pores are needed to achieve higher or faster pollutant removal.

5.2 Introduction

Nanomaterials (NMs) are defined as materials possessing at least one dimension in the nanoscale, 0–100 nm [6,46,47]. They can be designed from the bottom up (i.e., synthesized from gases or parent reactants), forming inherently heterogeneous structures that are assemblies of nanoscale building blocks and the regions between those building blocks. This heterogeneous bundle structure on the nanoscale may distinguish these materials from other materials [7]. Dimensionality and size of engineered NMs are the two main characteristics responsible for their specific properties [49]. Pokropivny and Skorokhod classified nanostructured materials into elementary units based on structure: zero-dimensional (0D), one-dimensional (1D), two-dimensional (2D), and three-dimensional (3D) structures [49]. Zero-dimensional NM example structures include fullerenes, quantum dots, and hollow spheres. One-dimensional NMs are long and tubular in shape, including nanotubes, nanowires, and nanorods. Two-dimensional NMs include nanowalls, nanosheets, and nanoplatets. Three-dimensional structures are collections or crystals of lower-dimension NMs that have been linked to form a larger network, such as zeolites. Using NMs for water purification is difficult because they need to be separated from the aqueous matrix after their use. Embedding NMs in electrospun fibers is emerging as a viable strategy for retaining NM function while easing their recovery [2,220].

Carbonaceous NMs have inherent characteristics conducive to water treatment such as high surface area, tunable surface chemistry, porous bundle structure, and favorable electronic properties [221,222,231,232,223–230]. In addition, high surface area to volume ratio of NMs, coupled with tunable surface chemistry, can overcome limitations of

traditional carbon-based bulk sorbents (e.g., granular and powdered activated carbons). The efficacy of adsorption onto traditional carbon-based bulk sorbents is limited by intraparticle mass transport diffusion rates and pore blockage, increasing the amount of material needed [53,233,234]. Traditional physical and chemical treatment are the top-down synthesis methods for activated carbon activation. Physical activation is where wood, peat, or coal is crushed and the char is activated via carbon dioxide and steam, while chemical activation uses chemical agents to carbonize and dehydrate the precursor [235]. There are very few existing water treatment processes that utilize materials designed from the bottom up, such as freely dispersed carbon nanomaterial (CNM) slurries, due to concerns about the efficient recovery of CNMs from the aqueous matrix they are intended to treat. Thus, the exploration of a technique that simultaneously supports CNMs while allowing unblocked mass transport of aqueous phase pollutants to the CNM surface is important. Electrospinning and electrospraying methods can generate CNM/polymer hybrids that provide a means of immobilizing different shapes of NMs while still exposing their surfaces and retaining their sorptive functionalities.

In electrospinning, an electrically charged jet of polymer solution produces polymer fibers by applying a high voltage potential (i.e., 10–40 kV) between a capillary tip and a grounded collector. The electric field overcomes the surface tension of the fluid droplet at the capillary tip, and the charged jet stretches and deposits polymeric fibers onto the grounded collector, forming a mat of fibers at micro- and nanoscale diameters. Electrospraying functions similarly and uses a lower viscosity fluid to produce a fine spray instead of a charged jet [100,101]. NMs can be incorporated into these polymeric fibers

either in a single-step process by adding them to the polymer solution before electrospinning or in a multi-step process where thermal or chemical treatment is applied post-electrospinning to the spun polymer fiber. Electrospinning enables direct addition of NMs to a polymer solution, while concurrent electrospraying allows for increased dispersion of NMs along the fiber surface. Electrospinning and electrospraying maintain polymer integrity through the adhesion of the wet spray onto the fiber matrix.

In this paper, we present a single-step electrospinning method that maintains nano-sorptive functionalities when integrating 0D, 1D, and 2D CNMs into a polymeric matrix. No post-electrospinning processing of the fiber was conducted to increase porosity because such strategies increase manufacturing costs [120]. While literature exists on adsorption capacity of both CNMs and PS fibers individually, there is no study that investigates and compares different CNM-PS composites to our knowledge. This study incorporates CNMs of three different dimensions (0D, 1D, and 2D) into porous polymer fibers via electrospinning to observe the effect of NM dimensionality on fiber morphology and to quantify the adsorption of phenanthrene (PNT) as a model aqueous organic contaminant. We designed experiments to test three inter-related hypotheses: 1) the porous nature of hybrid CNM composites leads to increases in diameter, pore size, and pore frequency compared to a neat polymer fiber; 2) dimethylformamide (DMF) solvent evaporation from the NM inside the polymer leaves behind inter-connected pores in the solidified polymer; and 3) CNM addition during electrospinning enhances pore formation and improves PNT sorption.

5.3 Experimental Methods

5.3.1 Preparation of electrospinning suspension

Polystyrene (PS, MW 350,000 g/mol, Sigma-Aldrich, St. Louis, MO) was selected for electrospinning because of its high hydrophobicity and mechanical integrity. N,n-dimethylformamide (DMF, Sigma-Aldrich, St. Louis, MO) was used as the organic solvent for dissolution of PS prior to electrospinning. NMs tested in this study include graphene oxide platelets (GO; N002-PDE, Angstron Materials, Dayton, OH, Oxygen content: 10–30%, Carbon content: 60–80%, specific surface area 400 m^2/g), multi-walled carbon nanotubes (MWCNT; OH functionalized MWCNT 10–20 nm, SKU 050203, Cheap Tubes, Grafton, VT, Specific Surface Area 100 m^2/g), and C_{60} fullerenes (C_{60}, catalog number MR6LP, 99+%, MER Materials, Tucson, AZ). All CNM-PS composites were produced by mixing 1% (m/v) NM with DMF and sonicating the solutions with a probe (Misonix, New York) for 15 minutes using the CEINT/NIST Preparation of Nanoparticle Dispersions from Powdered Material Using Ultrasonic Disruption [236]. 20% (m/v) PS was then added to the DMF-NM suspension. The final suspensions were stirred at 40°C for 12 hours.

5.3.2 Electrospinning set-up and parameters

An apparatus similar to previously published electrospinning systems (see Figure C-1 in SI) was constructed [11,102,160,187–189]. Briefly, electrospinning was performed using a high voltage power supply that provided up to 40 kV (Gamma High Voltage, Ormond Beach, FL), a syringe pump (New Era NE-300, Farmingdale, NY), a 10 mL plastic

syringe, and a grounded aluminum foil collector that was placed 15 cm away from the syringe tip. The experimental procedure consisted of loading the solution into the syringe fitted with a stainless steel needle that was connected to the high voltage power supply. The NM-PS composite solution was injected at 1 mL/h through a stainless steel, 22-gauge needle (Stainless Steel 304 syringe needle, Sigma Aldrich, St. Louis, MO) with an alligator clip attached to charge the needle and the polymer solution as it exited the capillary tip. The entire system was enclosed to mitigate the effects of air currents on the system and for safety. Humidity was measured using a Xikar hygrometer and was maintained at 40% at 25°C using a sponge saturated with deionized water inside the electrospinning enclosure.

5.3.3 Fiber characterization

Fibers were imaged using a Philips CM12 transmission electron microscope (TEM), and scanning electron microscope (SEM) images of fibers were obtained using a JEOL 2010F. Fiber pore diameter (n-500) and surface pore diameter (n-100) measurements were taken using ImageJ software (National Institutes of Health, Washington, D.C., USA). Brunauer-Emmett-Teller (BET) surface areas using N_2 adsorption-desorption isotherms for C_{60}, MWCNT, GO, and neat PS fibers were analyzed using a Micrometrics TriStar II 3020 surface area analyzer. Wettability was determined via water contact angle measurements run in triplicate on an Attension Theta contact angle meter (Biolin Scientific, Stockholm, Sweden) in conjunction with OneAttension software. Adsorption capacity was tested using PNT as a model pollutant.

5.3.4 Phenanthrene adsorption experiments under pseudo-equilibrium conditions

All PNT adsorption experiments were conducted in ultrapure water (Barnstead™ GenPure™, ThermoFisher Scientific, Waltham, MA) in completely mixed batch reactors. Briefly, 0.02 grams of CNM-PS fibers or 0.0002 grams of loose CNMs were placed in empty 40 mL glass bottles capped with Teflon-lined septa caps. Vials were then filled with distilled and deionized water and spiked with predetermined amounts of concentrated PNT stock solution. The concentrated PNT stock solution (1000 mg/L) was prepared in methanol. The ratio of methanol to water was kept below 0.1% (v/v) to eliminate any co-solvent effects on adsorption. After spiking, additional ultrapure water was added to eliminate headspace in the reactors, which were then placed sideways on a shaker table at 200 rpm for up to six days with samples measured at time points: 0.5, 1, 3, 6, 24, 72, and 144 hours. pH was measured but not manipulated in order to replicate ambient environmental conditions (pH=6.5–8.1). After removing the reactors from the shaker table, supernatants were filtered using Whatman GF/F 0.7 µm filters. Aqueous PNT concentrations were measured spectrophotometrically at $\lambda = 250$ nm using UV-visible spectroscopy (Hach DR2000, Hach USA, Loveland, CO). A broader spectrum ($\lambda = 200–800$ nm) was analyzed to ensure there was no unexpected interferences from dissolution of PS and loose CNMs. The amount of PNT adsorbed onto an adsorbent at time t, q_t, was calculated using Equation 5.1 as it has been applied elsewhere for pollutant kinetic removal by NMs [237]:

$$q_t \left(\frac{mg}{g} \right) = \frac{(C_0 - C_t) * V}{1000 * M} \qquad \text{(Equation 5.1)}$$

where;

C_0 (mg/L)   initial PNT concentration

C_t (mg/L)   PNT concentration at time t

V (L)   volume of PNT stock solution

M (g)   mass of adsorbent

A pseudo second order model was used to fit the kinetics data across the three CNM networks. The linearized Lagergren second-order kinetic equation may be represented as:

$$\frac{t}{q_t} = \frac{1}{k_2 q_e^2} + \frac{1}{q_e} t \qquad \text{(Equation 5.2)}$$

Where:

k_2 (g/mg/hour)   pseudo-second-order rate constant

t (hr)   time

q_t (mg/g)   amount of PNT adsorbed onto an adsorbent at time t

q_e (mg/g)   amount of PNT adsorbed onto adsorbent at pseudo-equilibrium

5.4 Results & Discussion
5.4.1 Comparison of fiber morphologies hybridized with 0D, 1D, and 2D CNM

Electrospun fibers with different types of CNMs were synthesized to test the hypothesis that the porous nature of hybrid CNM composites would lead to increases in diameter, pore size, and number of pores compared to a neat PS fiber. Figure 5.1 shows

SEM images of electrospun PS fibers neat and hybridized with C_{60}, MWCNT, and GO NMs. Common morphological changes due to CNM addition include wrinkled, rough fiber surfaces, beads, broken fibers, and adhered parallel fibers [98,140,238–240]. The left column of images in Figure 5.1 shows the macroscale structures of the four fiber types, and the middle and rightmost columns show the surface morphologies at increasing magnification. Beads (visible in left and middle columns and marked by white asterisks in image) are a common occurrence in electrospun fibers because increases in viscosity of the electrospinning solution prevent stretching into fiber segments [140]. The C_{60}-PS composite fiber showed long, continuous segments with no visible beads at macroscale. The MWCNT-PS composite fiber showed some beading. GO-PS and neat PS showed relatively higher bead frequency. Increased magnification on the polymer beads and fiber segments in the rightmost column began to reveal pores on the fiber surface (i.e., surface pores, as opposed to pores formed by overlapping fiber strands). The beads and fiber segments in all samples had rough and porous surfaces. These images indicated a possible internal porosity of CNM-PS composite fibers similar to that of a churro.[125]
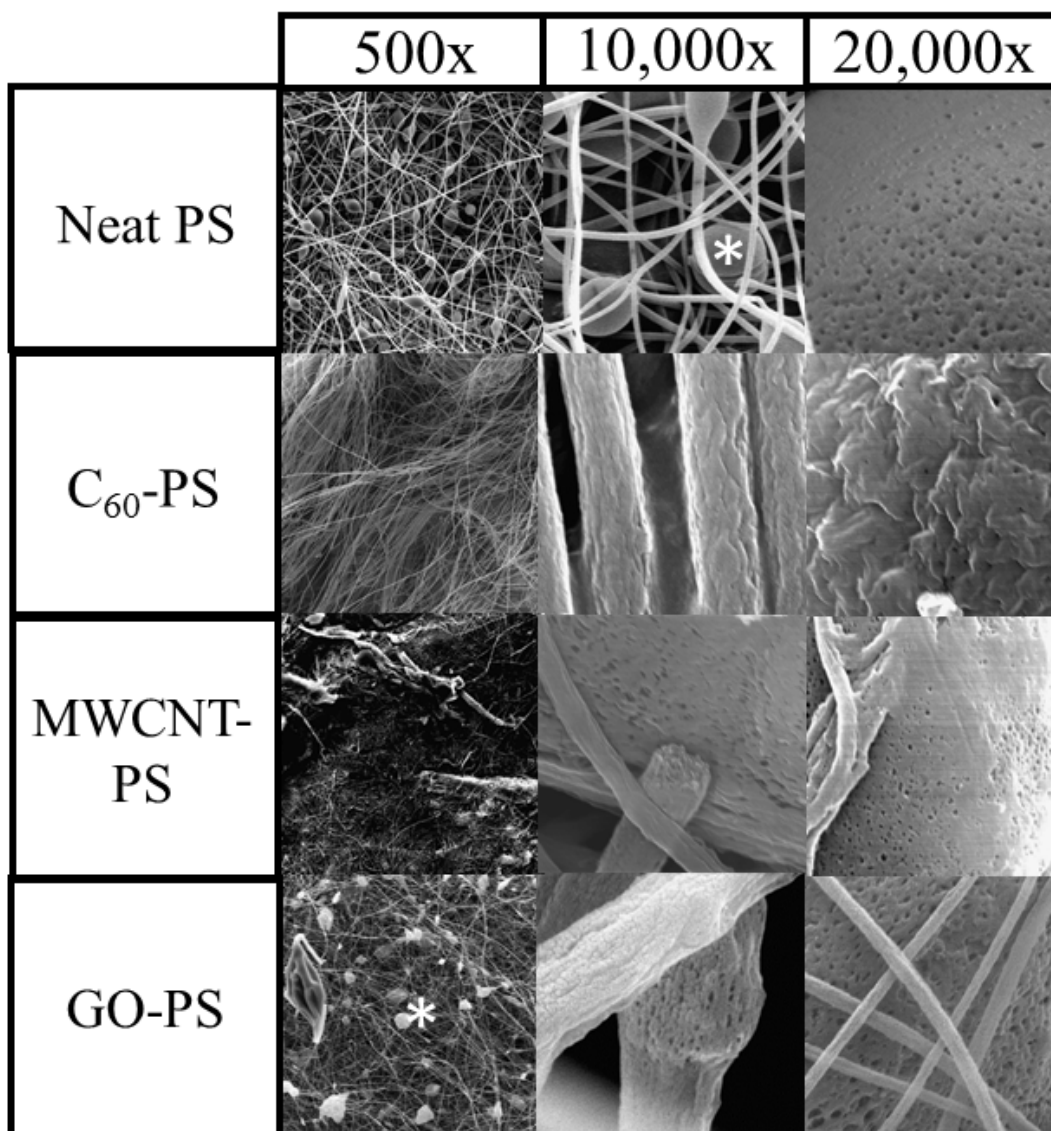
Figure 5.1 SEM Images of Neat PS, C$_{60}$-PS, MWCNT-PS, and GO-PS showing morphology at increasing magnification. Beading (marked by asterisks) is clearly discernible in top middle and lowest left neat PS image as well as bottom left GO-PS image. Pores are discernible on the surfaces of beads and fiber segments for all CNN-PS samples.

Surface porosity can be produced by the imprints of water vapor volatizing into the air, often seen on the surface of neat polymer fibers.[11,108,134] Pores form as the organic solvent evaporates from the polymer jet during electrospinning.[105,113,136] Because DMF rapidly evaporates from polymer molecules during electrospinning, we hypothesized that it would also evaporate from CNMs enmeshed in polymer chains, leaving behind inter-connected pores in the solidified polymer. These inter-connected pores may function as access points for pollutants in water and the encapsulated sorptive NM inside the polymer fiber (Figure 5.2). As such, we hypothesized that pore formation—and thus PNT sorption—would be enhanced by CNM addition and affected by differences in CNM surface area based on dimensionality. Surface pore diameter distributions (Figure 5.3) were quantified using SEM images (Figure 5.1). All four fibers had similar pore diameter distributions in the range of 80–140 nm: C_{60}-PS fibers (80±30 nm), neat PS (100±20 nm), MWCNT-PS fibers (120±30 nm), and GO-PS fibers (140±40 nm). Thus, our first hypothesis was partially rejected because pore diameter and number of pores did not increase with CNM addition.
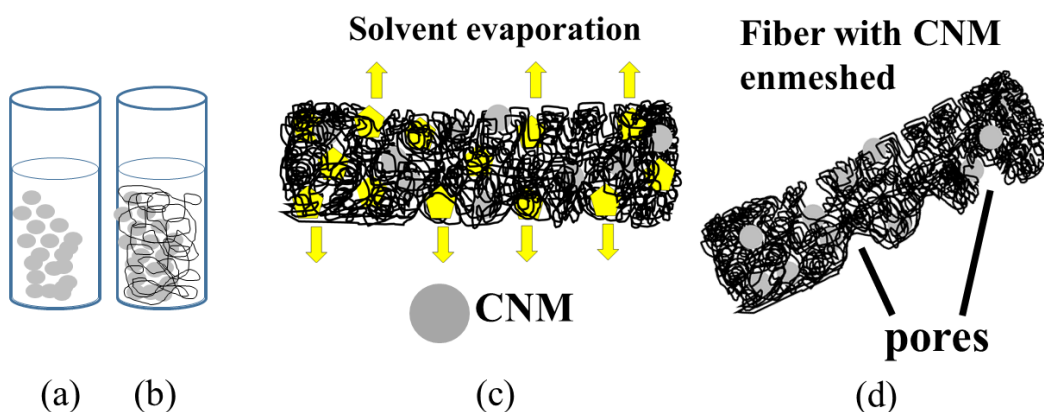
Figure 5.2 Procedural Schematic of Experimental Methods and resulting formation of pores: (a) CNM and DMF were probe sonicated, (b) PS was added to CNM and DMF mixture and stirred overnight, (c) CNM PS fiber was produced, where DMF molecules (yellow) sorbed to CNM instantly volatize in 20 kV field, leaving behind pores, and (d) DMF volatized, resulting in final porous CNM-PS fiber containing 4% CNM.

Due to the resolution limits of the SEM instrument, the surface pore diameter analysis utilized in Figure 5.3 is generally limited to macropores (>25 nm/1,000 Å). Nitrogen adsorption-desorption isotherms were performed to obtain additional information about the pore structure within the fiber at the meso- and micro-pore scale (mesoporous 100–1,000 Å, microporous <100 Å). Pore size distributions for the four fibers shown in Figure 5.4 were calculated using the Kelvin equation approximating each pore as cylindrical and using the Halsey film thickness approximation generated from Figure C-2 (see SI). The neat PS and the GO-PS had pores of similar sizes. Neat PS had pores distributed tightly around 25 Å and higher distributions between 50 and 250 Å. The GO-PS distributions are shifted on the x-axis, toward slightly larger pores with the largest at approximately 30 Å, and also showed distributions between 50 and 250 Å. The C_{60}-PS fiber had a small peak at 34 Å and a higher distribution of pores from 35 to 100 Å.

MWCNT-PS fiber pore volumes had no sharp peaks and were within 10 to 55 Å; no pores larger than 55 Å were detected. Neat PS had the highest surface area of all four materials (Table 5.1). In comparison, the PNT molecule measured 11.7 Å x 8 Å x 3.4 Å in size, which would not preclude its access to adsorbent CNM inside electrospun fibers [241]. Pore size was expected to increase as higher surface area CNM addition would sorb more DMF during the polymer solution mixing step versus neat polymer alone. More DMF would then separate from the interior of the fiber, leaving behind deeper, larger pores caused by evaporation during spinning. Our second hypothesis was rejected because CNM addition did not increase pore diameter or frequency or result in large inter-connected pores; in fact, addition of GO, C_{60}, and MWCNT led to decreased surface area using this analysis technique.
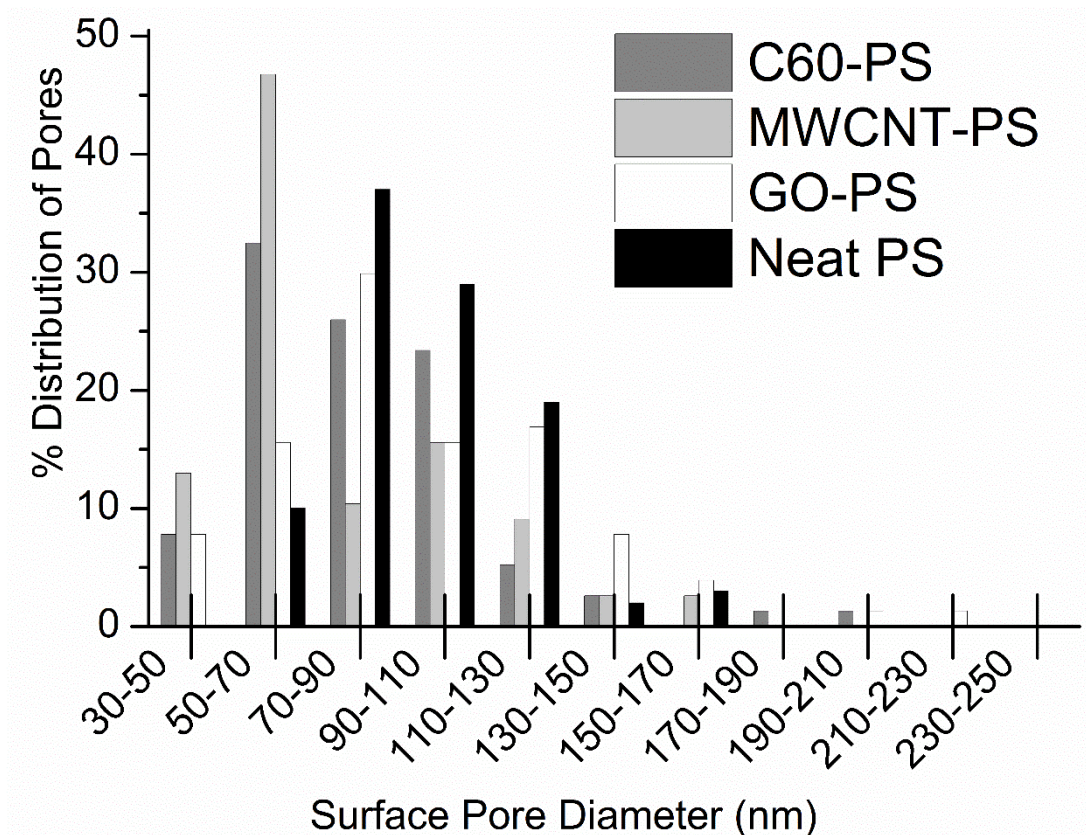
Figure 5.3 Distribution of CNM-PS Fiber Pore Diameters quantified from SEM images. C$_{60}$-PS averaged 80±30 nm, the neat PS averaged 100±20 nm, MWCNT-PS averaged 120±30 nm, and GO-PS averaged 140±40 nm.

To verify presence of CNM inside fiber and further reject the first and second hypothesis, TEM micrographs of CNM-PS composite fibers were examined. The CNMs were visible inside the polymeric fibers along the entire fiber length visible in the TEM image (Figure 5.5). The GO inside the fiber can be identified by its flaky appearance, particularly visible near the surface of the fiber segment. GO is known to localize in the surface regions of electrospun polymer fibers due to rapid solvent evaporation [140]. The MWCNT can be seen as tangled threads inside and outside of the main fiber segment.

The C_{60} fiber segment appears very dense and opaque; however, C_{60} aggregates can be distinguished by the flaky edge of the fiber segment.
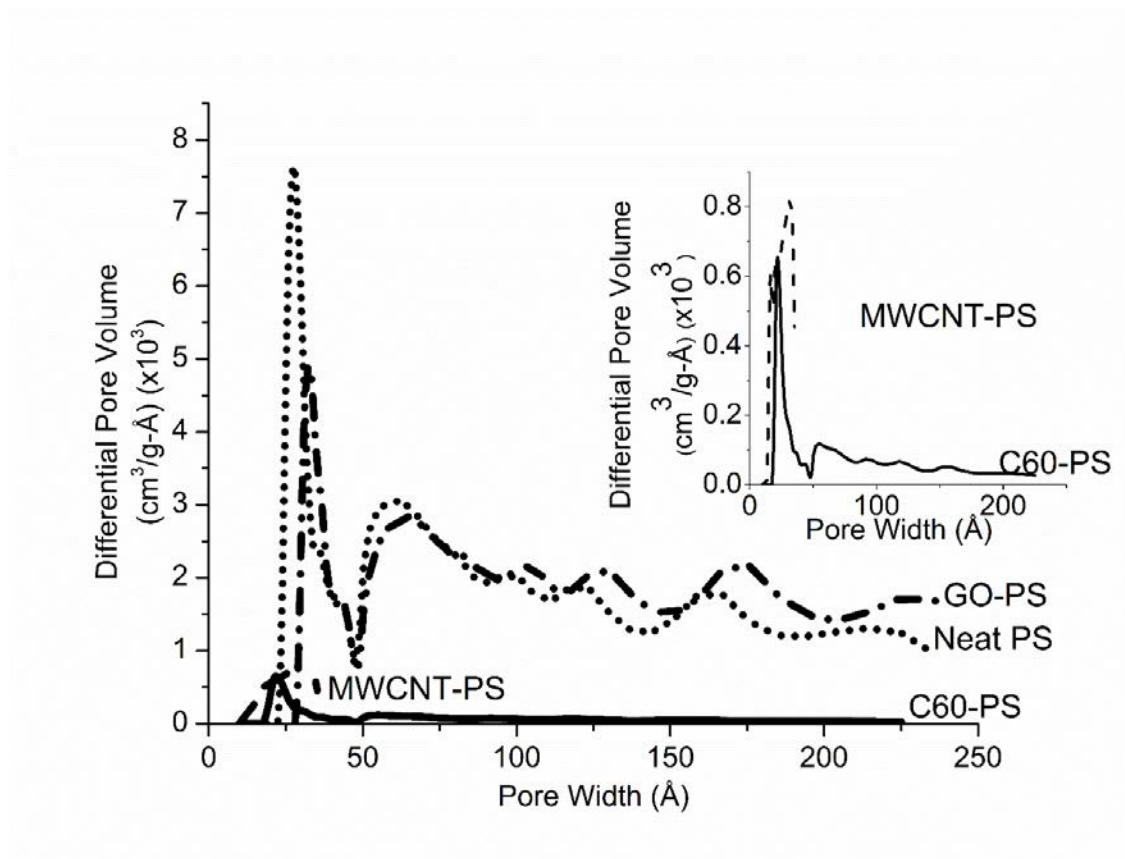
Figure 5.4 Differential Pore Volume based on N_2 deposition as a function of pore width for neat PS, C_{60}-PS, MWCNT-PS, and GO-PS fibers. Inset (right) shows MWCNT-PS and C60-PS data in greater detail.

Multiple sets of CNM-PS fibers were synthesized in different batches throughout this project. To approximate the CNM mass present in the final fibers, programmable thermal analysis (PTA) was used for GO-PS and MWCNT-PS fibers. Although care was taken to analyze representative samples (n=10), some variability is expected due to the unpredictability of aggregation and final jet path. The differences in CNM percentages

101

detected are evidence of this electrospinning condition. Based on multiple measurements of the same fiber, PTA detected carbonaceous NMs in the fibers at $3\pm1\%$ (m/v) for GO and at 8 ± 1 % (m/v) for MWCNT. C_{60}-PS proved too thermally unstable to use PTA, so a method was used where C_{60}-PS composites were dissolved in toluene, and their C_{60} content was measured using UV-visible spectroscopy. After taking various measurements, it was determined that the C_{60} content of these fibers was $4\pm0.3\%$ (m/v). Although CNM mass composition varied slightly, all fibers were found to contain CNM, confirming the rejection of CNMs leading to increased pore volume, frequency, and inter-connected pore formation stated in the first and second hypotheses.
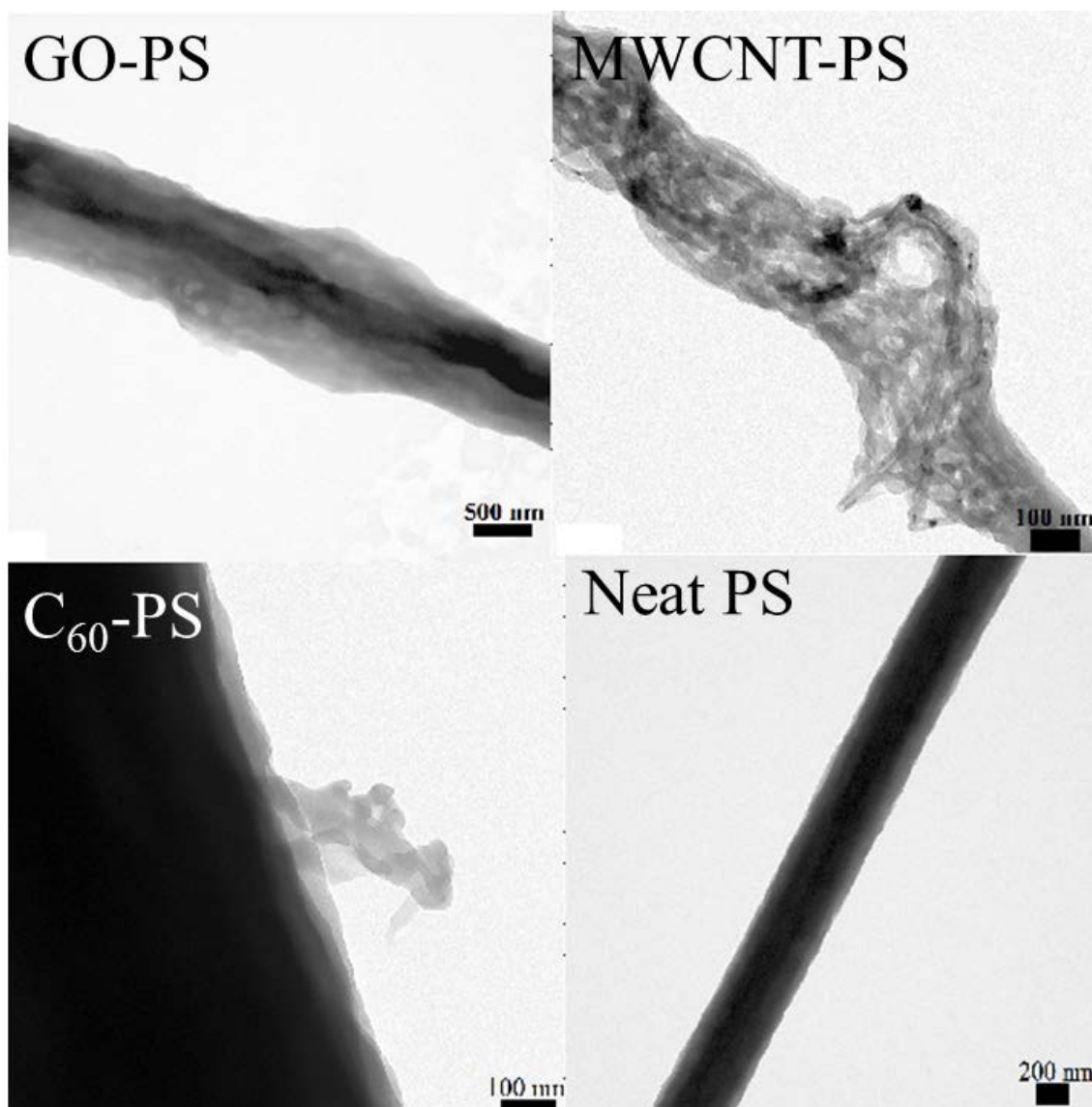
Figure 5.5 TEM Images of Neat PS and CNM-PS Composite Fibers showing CNM additives inside fiber lengths.

Fiber diameters of CNM-PS fibers ranged from about 400 to 1700 nm (Table 1).

C_{60}-PS and GO-PS fibers had the largest diameters, 1700±870 nm and 1700±840 nm,

respectively. The MWCNT-PS fibers had a diameter of 650±190 nm, and the neat PS had

the smallest diameter, 410±390 nm. Diameters of electrospun fibers vary with process

parameters such as viscosity and conductivity of solution and increases in voltage needed

to successfully form a charged jet [102,110,184]. Adding NMs increases the viscosity of electrospinning solutions; generally, more viscous solutions will produce fibers with higher fiber diameters [99,191]. This condition can be overcome by increasing the solution conductivity, facilitating the formation and maintenance of a charged jet of electrospinning solution between the needle tip and the collector plate. The presence of the MWCNT in the polymer solution can increase the charge-carrying capacity of the solution, which facilitates further jet stretching and results in smaller diameter fibers [212]. The fiber diameters for neat PS are the smallest due to the absence of any viscosity-increasing NMs. These findings support the first hypothesis that the addition of CNMs would lead to increases in diameter compared to a neat polymer fiber.

Table 5.1. Fiber and Particle Diameters, BET Surface Area, and Water Contact Angle measurement for suspended CNMs and CNM-PS fibers. Error is one standard deviation in each direction.

Material	Fiber/Particle Diameter (nm)	BET Surface Area (m^2/g)	Water Contact Angle
Neat PS	410 ± 390*	91	110 ± 7
C60-PS	1700 ± 870*	6	103 ± 3
C60	0.7a	n/a (unstable)	--
MWCNT-PS	650 ± 190*	16	105 ± 8
MWCNT	15a	140	--
GO-PS	1700 ± 840*	73	116 ± 2
GO	2-3 thick, 7000 longa	91	--

*=measured via ImageJ (n=500 measurements) from SEM images
a=from manufacturer

5.4.2 Pollutant removal from water using different CNM-PS composite fiber morphologies

We hypothesized that CNM addition during electrospinning would enhance pore formation and improve PNT sorption. Figure 5.6 shows PNT adsorption kinetics for GO-PS, C_{60}-PS, MWCNT-PS, and neat PS. Sample blanks' (no CNMs or CNM-PS composites) PNT concentrations were unchanged over time, showing there were negligible PNT losses. The neat PS fiber reached pseudo-equilibrium in one day and removed over 90% of PNT from solution. Neat PS fibers are previously reported to adsorb hydrocarbons onto their hydrophobic, porous surfaces [105,111,164,165]. Despite variations in fiber morphology, the CNM-PS composite fibers exhibited similar PNT

removal profiles as the neat PS fiber (Figure 5.6). The surface pores that formed did not

act as access points and therefore did not expose the sorptive CNM in the interior of the

fiber as hypothesized, and CNM addition inhibited PNT adsorption performance.
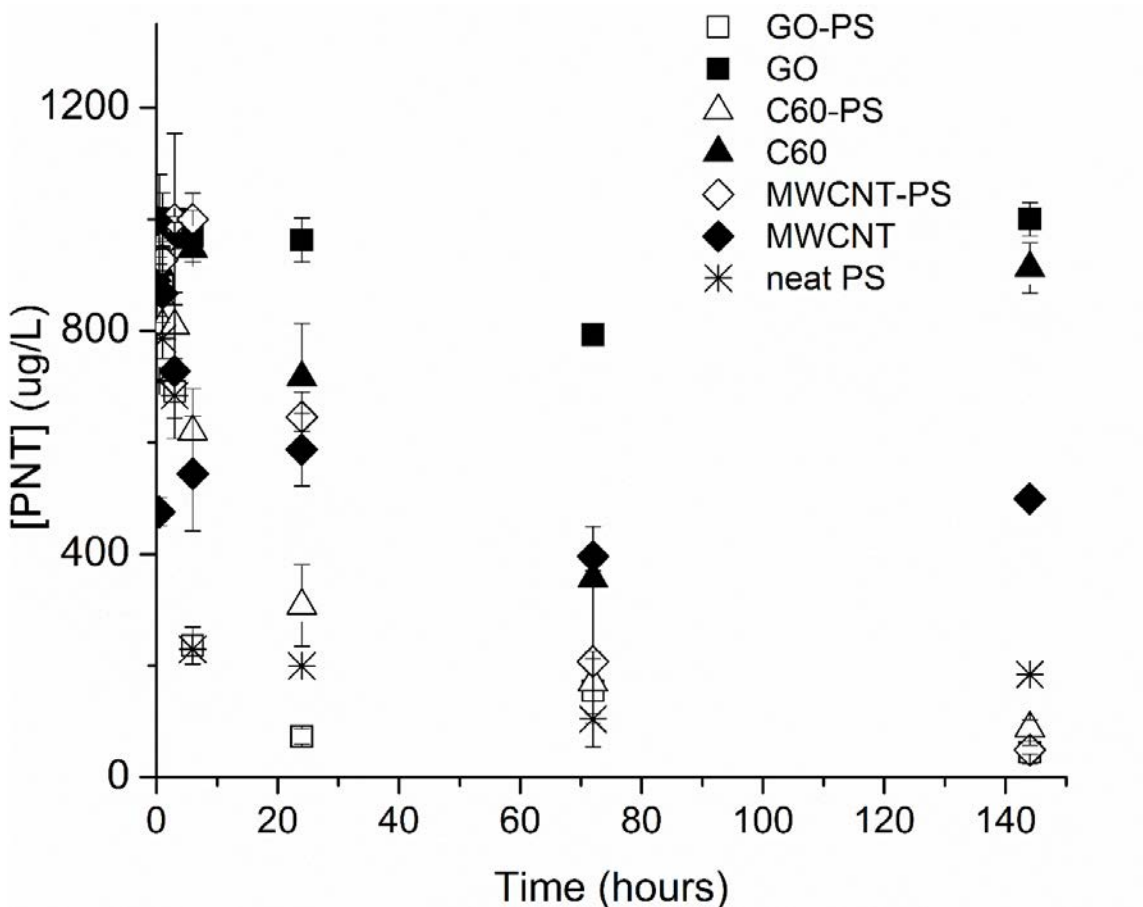
Figure 5.6 Phenanthrene Concentration Over Time across all CNM-PS composites and all suspended CNMs. Error bars are one standard deviation in each direction.

GO-PS, MWCNT-PS, C_{60}-PS, and neat PS fibers all reached pseudo-equilibrium

after about 24 hours. The adsorption capacities at pseudo-equilibrium (after 6 days, q_e)

were calculated using Equation 5.1 and are summarized in Figure 5.7. GO-PS, neat PS,

MWCNT-PS, and C_{60}-PS had adsorption capacities of 3.9, 2.9, 2.6, and 1.8 mg PNT/g

sorbent, respectively (see Figure C-3 in SI for q_t data). GO-PS and neat-PS had higher

adsorption capacities after 144 hours than MWCNT-PS and C_{60}-PS ($p<0.05$ according to Student's t-test). The BET surface area measurements (Table 5.1) showed that neat PS and GO-PS sorb more nitrogen. Similarities in PNT adsorption performance of the four fibers coupled with the hydrophobic character of PS-based fibers (see Table 5.1 for wettability data) indicated that PNT removal by CNM-PS fibers was a product of the hydrophobic effect. All four fibers had a contact angle greater than 90° (Table 5.1) and were thus hydrophobic. Contact angle testing illuminates the interaction between the fiber, PNT, and water molecules within a batch system. When the PNT and PS are in proximity, entropy within the water-fiber-PNT system increases as the water molecules surrounding both the nonpolar molecules release. This makes the PS-PNT association thermodynamically favorable and forms a nonpolar aggregate that leads to the extraction of PNT from the aqueous matrix along with the PS [242]. In this particular study, the PNT either preferentially sorbed to the polymer or was size-excluded by the polymer, preventing the PNT molecules from reaching the CNM inside, although the latter is unlikely considering the fiber surface pore size discussed previously.
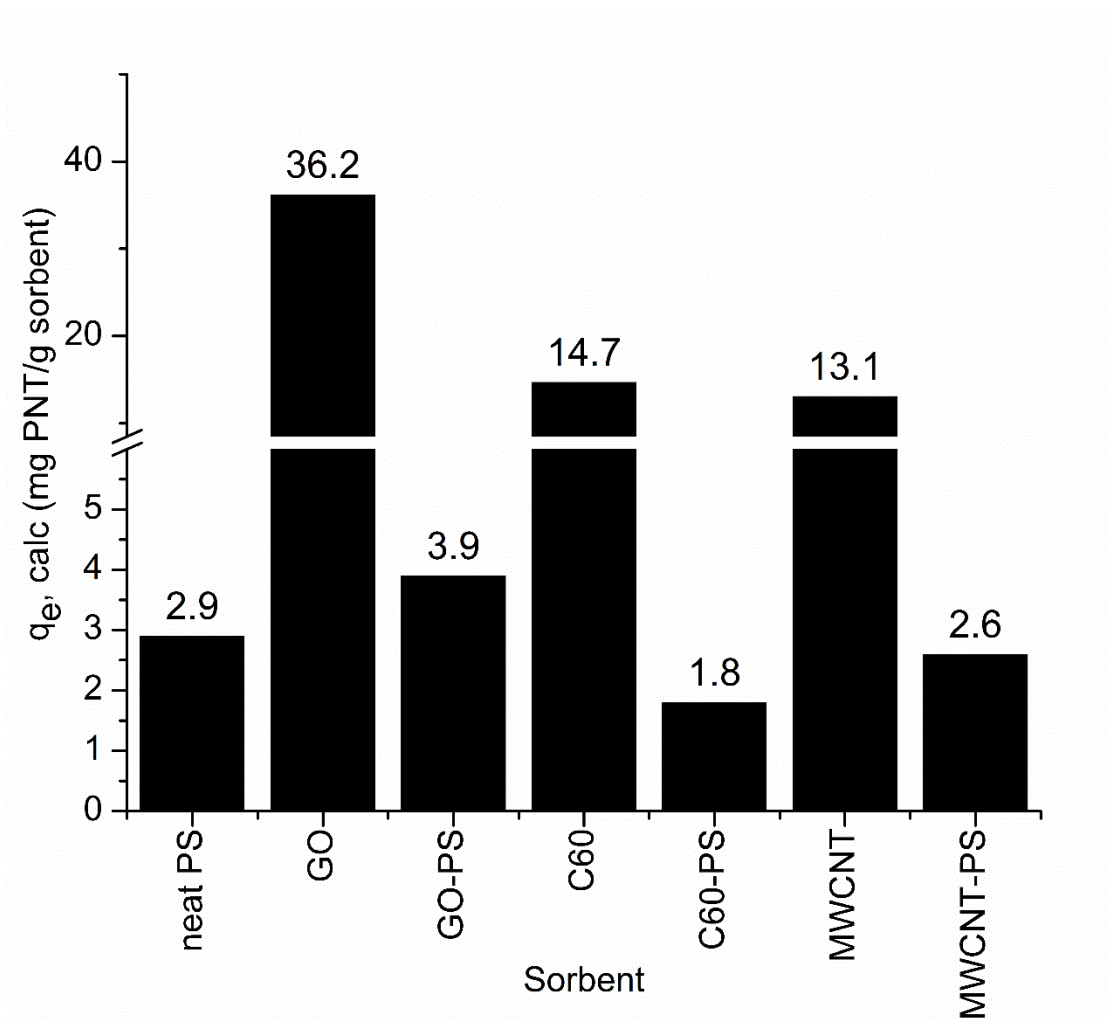
Figure 5.7 Calculated Adsorption Capacity (q_e, mg PNT/g sorbent) using equations 5.1 and 5.2. CNMs enmeshed in PS fibers had significantly lower adsorption capacity compared to their suspended counterparts.

In parallel, kinetic adsorption data was generated for suspended CNM (i.e., without PS fibers) in water (see Figures 5.6 and 5.7). The order of adsorption capacity for each material after 144 hours was graphene oxide>MWCNT=C_{60} (results statistically verified using Student's t-test, $p < 0.05$; see Figure C-4 in SI for q_t data). Yang et al. found that the adsorption affinity of PNT on single-walled carbon nanotubes (SWCNT), MWCNT, and C_{60} follow the order SWCNT>MWCNT> C_{60} [8]. Suspended CNM had

higher adsorption capacity than their CNM-PS composite counterparts for all fibers. This confirms the loss of surface area upon CNM addition observed using the BET surface area technique listed in Table 5.1.

We hypothesized that that the porous nature of hybrid CNM composites would lead to increases in diameter, pore size, and pore frequency compared to a neat polymer fiber and that enhanced pore formation would improve PNT sorption. Although suspended CNMs removed PNT as described in Figure 5.6, the same CNMs did not affect PNT uptake when incorporated into electrospun PS fibers, despite the presence of pores on the fiber surface. This could be attributed to interstitial sorption sites formed during aggregation of suspended CNMs, unlike CNMs dispersed in PS macrostructure. Instead, the hydrophobic effect between the PS and PNT exerted more influence in removing PNT than the CNMs incorporated in the polymer. Therefore, we reject our hypothesis that CNM addition would enhance pore formation and improve PNT sorption.

5.5 Summary & Conclusions

- Three carbon-based nanomaterials (0D fullerenes, 1D carbon nanotubes, and 2D graphene platelets) were incorporated into polystyrene electrospun fibers and 3 related hypotheses were tested:
  - The porous nature of hybrid CNM composites leads to increases in diameter, pore size, and pore frequency compared to a neat polymer fiber;
  - DMF evaporation from the NM inside the polymer leaves behind inter-connected pores in the solidified polymer; and
  - CNM addition during electrospinning enhances pore formation and improves PNT sorption.
- Fiber diameter increased with CNM addition; pore size, pore frequency, and PNT adsorption performance did not change compared to neat PS fibers; no interconnected pores were observed.

Research Question 4:

How does the incorporation of different carbonaceous nanomaterial geometries into electrospun polystyrene fibers change the pore diameter, frequency, or shape?

Hypothesis 4.

The porous nature of hybrid CNM composites leads to increases in diameter, pore size, and number of pores compared to a neat polymer fiber, while Dimethylformamide (DMF) evaporation from the NM inside the polymer leaves behind inter-connected pores in the solidified polymer.

The porous nature of CNMs coupled with the variation in geometry was hypothesized to lead to distinct fiber morphologies, specifically, that the fiber pore diameter and frequency would increase with increasing dimensionality based in increasing edge and corner sites of the CNM, and further, that DMF volatilization from within the CNM in the interior of the polymer jet coupled with phase separation and rapid solidification of the fiber would produce inter-connected pore networks within the fibers. *Hypothesis 4 was rejected* based on nitrogen adsorption-desorption experiments with BET surface area modeling coupled with PNT adsorption testing. The surface area of PS fibers decreased with the addition of C_{60} fullerenes, multiwalled carbon nanotubes, and graphene platelets, and the PNT adsorption capacity did not significantly increase based on kinetics experiments.

CHAPTER 6

HIERARCHICAL PORE STRUCTURES OF ELECTROSPUN TITANIUM DIOXIDE/GRAPHENE OXIDE NANOCOMPOSITES FOR ARSENATE AND P-CHLOROBENZOIC ACID REMOVAL

Abstract

A porous titanium dioxide (TiO_2), graphene oxide (GO), and polystyrene (PS) composite electrospun sorbent for point-of-use (POU) water treatment was developed using a single-step synthesis process. Porous fiber morphology was achieved using polyvinylpyrrolidone (PVP) as a porogenic sacrificial polymer, which was subsequently solubilized in water after being co-spun with TiO_2 and PS. The aim of this technique was to produce a fiber with micro- and macro-porous morphology in order to facilitate the interaction of embedded TiO_2 with aqueous arsenic. The effect of using PVP as a porogen on fiber morphology was evaluated using scanning electron microscopy (SEM), nitrogen porosimetry, Fourier-transform infrared spectroscopy (FTIR), programmed thermal analysis (PTA), and thermogravimetric analysis (TGA). NM fibers were found to contain between 3-30% NM content. SEM imaging shows increased surface features after PVP was eliminated without altering fiber diameter and maintaining even distribution of TiO_2 in the polymeric network. Nitrogen porosimetry coupled with Brunauer-Emmett-Teller (BET) modeling show an initial surface area of 6 m^2/g for neat PS fiber, 2.1 m^2/g for TiO_2-PS-PVP fiber, and 14.9 m^2/g for TiO_2-PS fiber after PVP elimination. Barrett-Joyner-Halenda (BJH) modeling shows pore width distributions between 10-200 nm.

FTIR and TGA analysis show some residual PVP (20% (w/w)) remains in the polymeric network after immersion in water. Whereas previous work has shown that TiO_2-PS without a porogen did not sorb arsenic, using PVP as a porogen in the electrospinning process yielded sorbent fibers with a Freundlich coefficient (K_f) of $3x10^{-4}$ µg As/ mg TiO_2 and favorable adsorption energy (1/n=0.6). Statistically significant pCBA and arsenic removal by TiO_2-PS, GO-PS, and TiO_2-GO-PS was observed via a single-point removal test and differential batch column testing and modeled using the Pore Surface Diffusion Model (PSDM). Titanium dioxide leaching during both the removal test and DCBR test was negligible (<0.01% by mass based on mass composition of fiber adsorbent).

6.1 Introduction

Drinking water treatment systems depend on physical-chemical sorption processes for contaminant reduction. Nanomaterials (NM) exhibit bulk physical-chemical behaviors such as electrostatics and hydrophobicity as well as large surface area and specific functionality.[230–232] NMs' high surface area to volume ratio coupled with tunable pore size and surface chemistry overcome many limitations of traditional bulk sorbents in small-scale systems, whose efficacy can be limited by pore diffusion and mass of material needed.[53,233,234] Nanoscale versions of bulk metal oxide adsorbents, such as titanium dioxide, can be synthesized from the bottom up to control shape and edge structures which can improve adsorption capacity and selectivity towards aqueous organic pollutants.[243,244] NMs' high surface area coupled with shorter intraparticle diffusion distance translate to higher adsorption capacity and faster kinetics when compared to conventional bulk macroporous sorbents.[245,246] These properties make NMs particularly attractive for point-of-use (POU) water treatment applications where centralized water treatment infrastructure is unavailable.[2,66,247,248] However, simply adding NMs as free particles to water is not feasible in POU systems due to the need to completely remove the particles prior to consumption of treated water. There is a need to incorporate NMs into macroscale structures without losing NM benefits. Thus, the exploration of entrapment techniques such as electrospinning that simultaneously supports NMs while allowing rapid diffusion of aqueous phase pollutants to the NM surface is relevant to advancing small-scale system water treatment technologies.

114

Electrospinning allows for the facile incorporation of nanomaterials into polymer solutions which are then extruded into nano- and micrometer-diameter porous fibers which hold nanomaterials in place while allowing the nanomaterials to be effective adsorbents or photocatalysts.[179,183,239,249] The advantage of electrospinning is that virtually any nanomaterial can be incorporated into the polymer precursor solutions. Examples from the literature include carbon-based nanomaterials (nanotubes, graphene oxide, fullerenes) as well as metal oxides which may be used for environmental remediation (iron oxides, titanium dioxide, and gold).[11,100,173,220,248,250–252] Studies examining the potential for application of nanomaterial-polymer electrospun composites indicate that fiber morphology is a critical component in maintaining the accessibility of the nanomaterials incorporated into polymer for processes such as adsorption.[11,100,220] Once the nanomaterial is embedded inside of a polymer fiber, fiber surface pores are the main access point between nanomaterials' reactive surfaces and their target pollutants in aqueous solution; thus, engineering a pore structure which is conducive to environmental remediation processes such as adsorption is a critical part of nanomaterial-polymer electrospun fiber fabrication.[12,113,124,125,134,136]

Sorbent, sorbate, and liquid matrix properties influence adsorption kinetics. Pore size, frequency, and tortuosity are important attributes of adsorbent materials used for contaminant remediation. The characteristics of pores dictate transport of contaminants out of aqueous matrices, specifically diffusion. The Pore-Surface Diffusion Model (PSDM) dictates that adsorption takes place in four steps: 1) bulk diffusion, 2) film diffusion, 3) intra-particle diffusion, and 4) attachment to the sorbent surface.[253] Film and

115

intra-particle diffusion are key in determining adsorption kinetics. Pore diffusion is specific to the pore liquid. The PSDM assumes a constant flow rate, plug flow conditions, local bulk phase mass flux at the exterior surface of the adsorbent as a linear driving force, a local adsorption equilibrium between the adsorbed solute and the pore liquid adsorbate concentration, and no interactions between the adsorbing compounds during the diffusion process.[254]

The material balance for pore diffusion reads:

$$\Delta \dot{n}_P 4\pi r^2 \Delta t = \Delta q 4\pi 4^2 \Delta r \rho_P + \in_P \Delta c_P 4\pi 4^2 \Delta r \qquad \text{Equation 6.1}$$

Where $\dot{n}_P$ is the mass transfer rate per unit of surface area, r is the radial coordinate, C_p is the adsorbate concentration in the pore fluid, q is the adsorbent loading, and $\in_P$ is the particle porosity, and ρ_P is the particle density. For pore diffusion, the mass transfer rate per unit of surface area is given by

$$\dot{n}_p = D_P \frac{\partial c_P}{\partial r} \qquad \text{Equation 6.2}$$

Where D_P is the pore diffusion coefficient. Combining the two equations:

$$\rho_P \frac{\partial q}{\partial t} + \in_P \frac{\partial c_P}{\partial t} = D_P \left(\frac{\partial^2 c_P}{\partial r^2} + \frac{2}{r} \frac{\partial c_P}{\partial r} \right) \qquad \text{Equation 6.3}$$

Applying the chain rule and introducing an apparent pore diffusion coefficient, Da:

$$D_a = \frac{D_P}{\rho_P \frac{\partial q}{\partial c_P} + \in_P} \qquad \text{Equation 6.4}$$

For the Freundlich isotherm, the slope becomes:

$$\frac{\partial q}{\partial c_P} = nK c_p{}_p^{n-1} \qquad \text{Equation 6.5}$$

Equation 6.3 then becomes:

$$\frac{\partial q}{\partial c_P} = D_a\left(\frac{\partial^2 c_P}{\partial r^2} + \frac{2}{r}\frac{\partial c_P}{\partial r}\right)$$

Equation 6.6

Initial and boundary conditions for the batch reactor are:

$q=0$, $c_P=0$ at $t=0$ and $0 \leq r \leq r_P$

$c=c_0$ at $t=0$

$$\frac{\partial c_P}{\partial r} = 0 \; at \; t > 0 \; and \; r = 0$$

$$D_P\frac{\partial c_P}{\partial r} = -\frac{\epsilon_B}{a_{VR}}\frac{\partial c}{\partial t} \; at \; t > 0 \; and \; r = r_P$$

Equation 6.7

Where a_{VR} is the external surface area related to reactor volume.[255]

The pore structure of a material determines the quantity of a pollutant it can adsorb.[51] The transport of a contaminant molecule may be inhibited or delayed by the path it must take inside of a sorbent pore, which in turn affects the kinetics of the adsorption reaction.[31] Controlling the pore size, frequency, tortuosity, and interconnectivity in electrospun fiber segments is important for contaminant transport.[113] The simplest means of manipulating pore size via post-electrospinning modification is the use of a sacrificial material, where a supporting polymer is co-spun with a sacrificial polymer which acts as a porogen. The porogen is then eliminated via dissolution or thermal treatment without affecting the supporting polymer.[12,113,125] Thermal treatments involve heating the as-spun dual-polymer fibers to a high temperature (100-1100°C) to achieve the volatilization of the sacrificial polymer while preserving or calcining the polymer of interest.[125,126] Dissolution of a sacrificial polymer from a dual-polymer system is achieved using any solvent in which the sacrificial polymer is soluble, including water.[12,114,127,128]

Arsenic is a health concern for many consumers who rely on private groundwater wells for their drinking water supply both in and outside of the United States.[256–259] Although reverse osmosis and ion exchange are currently the only EPA-approved methods of arsenic compliance, POU technologies can help decrease the risk of arsenic exposure in private drinking water supplies.[5] Arsenic may be adsorbed by metal oxides by forming inner-sphere complexes.[28,202,247] Titanium dioxide is a widely available, cost-efficient meal oxide used in consumer products as well as photocatalytic applications.[28,84,260–264] Adsorption is a step in the photocatalytic process, making TiO_2 a candidate for the removal of arsenic in aqueous solutions via sorption processes.[63,202,247] Para-chlorobenzoic acid (pCBA) is a polar organic model pollutant representative of highly carcinogenic chlorinated organic pollutants found in pesticides.[265] Groundwater may become contaminated with these compounds via fertilizer application, sewage infiltration from leaking sewage system pipes, or land application of sewage sludge.[266] Graphene oxide has been found to adsorb compounds such as pCBA via π-π bonding and hydrophobic effects.[267]

In this study, we incorporate titanium dioxide and graphene oxide nanoparticles into polystyrene solution and co-spin with polyvinylpyrrolidone as a porogen to increase GO/TiO_2 surface area available for arsenic adsorption. We hypothesized that co-spinning with and subsequent elimination of the porogenic polymer, PVP, would increase the GO and TiO_2 surface area available for reactions with aqueous arsenic and pCBA (respectively) by leaving behind a porous fiber architecture extending from the fiber surface to the interior, where GO/TiO_2 is embedded. We specifically hypothesized a

meso- and microporous fiber structure as verified by arsenic adsorption isotherm and kinetic experiments.

6.2 Experimental Methods
6.2.1 Fiber Synthesis

Preparation of electrospinning suspension

Polystyrene (PS, MW 350,000 g/mol, Sigma-Aldrich, St. Louis, MO) was selected for electrospinning because of its high hydrophobicity and mechanical integrity. N,n-dimethylformamide (DMF, Sigma-Aldrich, St. Louis, MO) was chosen as the organic solvent for dissolution of PS and PVP prior to electrospinning for its high dielectric constant. Polyinvylpyrrolidone (PVP) was chosen as a sacrificial polymer due to its high water solubility and ease of co-spinning with PS and DMF. Titanium dioxide (Degussa P95, Sigma-Aldrich, St. Louis, MO) and graphene oxide (N002-PDE-HD, Angstron Materials, Dayton, OH) were incorporated by mixing 25% (m/m) NM:polymer with 10 mL DMF and sonicating the solutions with a probe (Misonix, New York) for 15 minutes using the CEINT/NIST Preparation of Nanoparticle Dispersions from Powdered Material Using Ultrasonic Disruption.[236] 10% (m/v) PS was then added to the DMF-NM suspension and mixed over 55°C for 12 hours. 10% (m/v) PVP was then added to make a TiO_2-PS-PVP suspension. The final suspensions were stirred at 55°C for 12 hours prior to spinning.

119

Electrospinning system and conditions

An apparatus similar to previously published electrospinning systems (see Figure D-1 in SI) was constructed.[11,102,160,187–189] Electrospinning was performed using a high voltage power supply that provided up to 40 kV (Gamma High Voltage, Ormond Beach, FL), a syringe pump (New Era NE-300, Farmingdale, NY), a 10 mL plastic syringe, and a grounded aluminum foil collector that was placed 15 cm away from the syringe tip. The experimental procedure consisted of loading the solution into the syringe fitted with a stainless steel needle that was connected to the high voltage power supply. The TiO_2-PS-PVP composite solution was injected at 2 mL/h through a stainless steel, 22-gauge needle (Stainless Steel 304 syringe needle, Sigma Aldrich, St. Louis, MO) with an alligator clip attached to charge the needle and the polymer solution as it exited the capillary tip. The entire system was enclosed to mitigate the effects of air currents on the system and for safety. Humidity was measured using a Xikar hygrometer and was maintained at 40% at 25°C using a sponge saturated with deionized water inside the electrospinning enclosure. TiO_2-PS-PVP fibers were collected and PVP was subsequently eliminated via 24-hour water submersion prior to characterization as TiO_2-PS.

Determination of optimal PS:PVP ratio for mechanical integrity

Varying PS:PVP ratio can be optimized to maximize the surface area of TiO_2-PS exposed upon PVP elimination, while still maintaining fiber integrity in a turbulent aqueous environment. For this study, three ratios of PS:PVP were prepared: 3:1, 1:1, and 1:3 based on previously published work and verified by preliminary fiber integrity experiments.[12] Fibers were weighed and then immersed in water for 24 hours in capped

bottles with magnetic stirrers set at 350 revolutions per minute in order to dissolve PVP and test the integrity of the remaining TiO_2-PS after mixing. The fibers were then gently extracted using blunt tweezers, set on squares of aluminum foil, and dried in an oven at 50°C for 10 hours and subsequently allowed to cool. Upon cooling, fibers were gently separated from the foil and weighed again until the actual weight was within 5% of their theoretically predicted weight after PVP elimination via washing. Fibers were then manually abraded to determine their mechanical integrity.

6.2.2 Fiber Characterization & Adsorption Testing

Scanning electron microscope (SEM) images of fibers were obtained using a JEOL 2010F. N_2 adsorption-desorption isotherms coupled with Brunauer-Emmett-Teller (BET) and Barrett-Joyner-Halenda (BJH) models were obtained for TiO_2-PS-PVP and TiO_2-PS using a Micrometrics TriStar II 3020 surface area analyzer.[268] Thermogravimetric analysis was used to confirm the mass composition of electrospun TiO_2-PS fibers by comparing the amount of ash produced by neat PS with the amount of ash produced by TiO_2-PS. The fibers were thermally degraded using a Labsys Evo 1600°C in Helium at a heating rate of 20°C/min up to 425°C. Fourier-Transform Infrared Spectroscopy (Bruker IFS66V/S, Bruker, Madison, WI) was used to characterize the composition of TiO_2-PS fibers after immersion in water.

Adsorption isotherms were run using sodium arsenate heptahydrate (As(V); Sigma-Aldrich, St. Louis, MO). All adsorption isotherm experiments were conducted in ultrapure water (Barnstead™ GenPure™, ThermoFisher Scientific, Waltham, MA) in completely mixed batch reactors. Briefly, 0-1000 mg/L of P25 TiO_2 powder ((Aeroxide

P25, Millipore Sigma, Darmstadt, Germany) or NM-polymer composite fiber (as

TiO_2/GO) were placed in empty 250 mL glass bottles capped with Teflon-lined septa

caps. Bottles were then filled with distilled and deionized water and spiked with

predetermined amounts of concentrated arsenic stock solution. The As(V) test solution

(20 µg/L) was prepared in ultrapure water buffered with 10 mM $NaHCO_3$, and adjusted

to pH 7±0.1 with 0.1 M nitric acid (HNO_3) to replicate POU conditions, then the reactors

were completely filled and placed sideways on a shaker table at 200 rpm for six days to

ensure equilibration. After removing the reactors from the shaker table, supernatants were

filtered using ThermoFisher Target2 0.45 µm syringe filters (ThermoFisher Scientific,

Waltham, MA, USA). Aqueous arsenic concentrations were measured using ICP-MS

(ThermoFisher XSERIES 2, ThermoFisher Scientific, Waltham, MA) after being

acidified to (2% (v/v) HNO_3) using EPA Method 6020A.

A simple adsorption test was run using sodium arsenate heptahydrate and pCBA

(para-chlorobenzoic acid; Sigma-Aldrich, St. Louis, MO) as a model pollutants. Two

doses of sorbent (100 mg/L and 150 mg/L) were tested in triplicate using a solution of 1

mg/L pCBA, 20 µg/L Sodium arsenate, and 10 mM $NaHCO_3$ in ultrapure water (250 mL

bottles) adjusted to pH 7 using 0.1 M hydrochloric acid. The bottles were put on a shaker

table at 200 rpm for 9 days, after which samples were collected and filtered using

ThermoFisher Target2 0.45 µm syringe filters. Aqueous arsenic concentrations were

measured using ICP-MS after being acidified using EPA Method 6020A. High

performance liquid chromatography (HPLC) analysis was performed using a Waters

separation module 2695 (Milford, MA, USA) with a reverse-phase analytical column

(RP18) to measure pCBA. The mobile phase consisted of 55% methanol and 45% 10 nM phosphoric acid at 1 mL/min. A Waters 2996 Photodiode Array Detector set to a wavelength of 234 nm was used for detection. pH was measured with a Thermo Scientific Orion STAR A329 portable meter.

Finally, a differential batch reactor column (DCBR; see Figure 6.1) was used to test kinetics of arsenic adsorption on TiO_2-GO-PS.[253] 20 ug/L arsenic and 1 mg/L pCBA test solution and was recirculated from a completely mixed feed container (4 L) at 700 mL/min (high Reynolds number condition; Re≈300)[253] in order to eliminate the effect of film diffusion. TiO_2-GO-PS mass (1 g) was calculated from batch isotherm data with the goal of achieving 50% arsenate removal after 9 days. The DCBR was constructed using Teflon tubing (Thomas Scientific, Swedesboro, NJ), a stainless steel column (2 cm in diameter, 6 cm in length), nylon sponge supports, stainless steel fittings (Swagelok), and a peristaltic pump (Masterflex, Vernon Hills, IL). The column was run in upflow, as shown in Figure 6.1. Sample aliquots (7 mL) were collected over time and the same volume of test solution was then added back into the feeding tank. Data was modeled using AdDesignS software.[254]
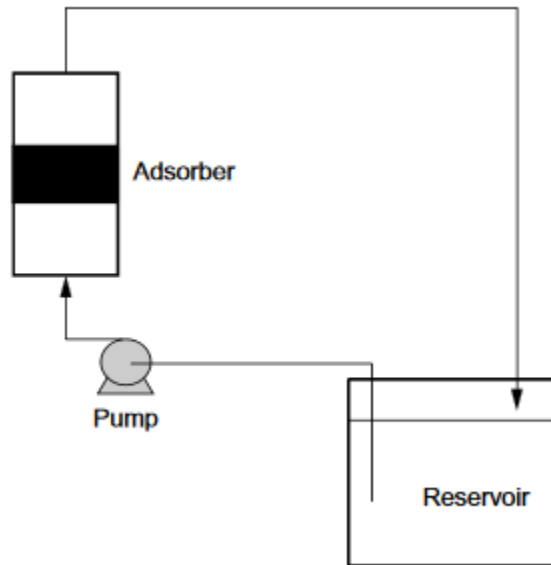
Figure 6.1 Differential Column Batch Reactor schematic adapted from Worch, 2012.[255]

6.3 Results & Discussion

6.3.2 Fiber Characterization

Based on washing and chemical integrity tests, 1:1 PS:PVP was found to be the most consistently in agreement with its theoretical predicted weight after washing while simultaneously staying intact during abrasion, making it the optimal choice for further development as a nanocomposite fiber for POU adsorption application.

SEM imaging shows fiber morphology changes after PVP elimination via dissolution in water. Figure 6.2 shows TiO_2-PS-PVP fibers have smooth surfaces with no prominent surface features at 1000x magnification. After PVP elimination, fibers become tightly packed and develop surface features, including wrinkles, channels, and cavities resembling pores. Similar effects have been observed in other studies using sacrificial polymers for the engineering of rough electrospun polymeric fiber surfaces, where fiber

morphology features including channels and pores have been produced using sacrificial polymers.[113,120,269] Figure 6.2 shows that fiber integrity is preserved after washing. Fiber diameter measurements made using ImageJ (n=300) show no change in fiber diameter despite a theoretical decrease in mass due to PVP elimination (Table 6.1). In Figure 6.3, backscatter electron detection imaging of TiO_2-PS reveals a rich network of nanoscale titania embedded throughout the fiber segments. Thus, the nanomaterial dispersion has been preserved in the fiber after PVP elimination while producing a porous surface morphology.

Table 6.1 Fiber Diameter and BET Surface Area of TiO_2-PS-PVP and TiO_2-PS Fibers.

Sample ID	Fiber diameter (µm)	BET surface area (m^2/g)	% (m/m) TiO_2, calculated	% (m/m) TiO_2, measured	As(V) Freundlich isotherm parameters		
					K^a $\frac{ug\ As}{mg\ TiO_2}$	$1/n^a$	R^2
TiO_2-PS-PVP	1.1±0.2	2.1	25	--	--	--	--
TiO_2-PS	1.2±0.3	15	50	30	$3x10^{-4}$	0.6	0.84
TiO_2	--	56^{270}	100	100	$1x10^{-4}$	0.9	0.98
Neat PS	0.81±0.2	6.0	<1	<1	0	0	--
[a] Freundlich equation $q=KC_e^{1/n}$							
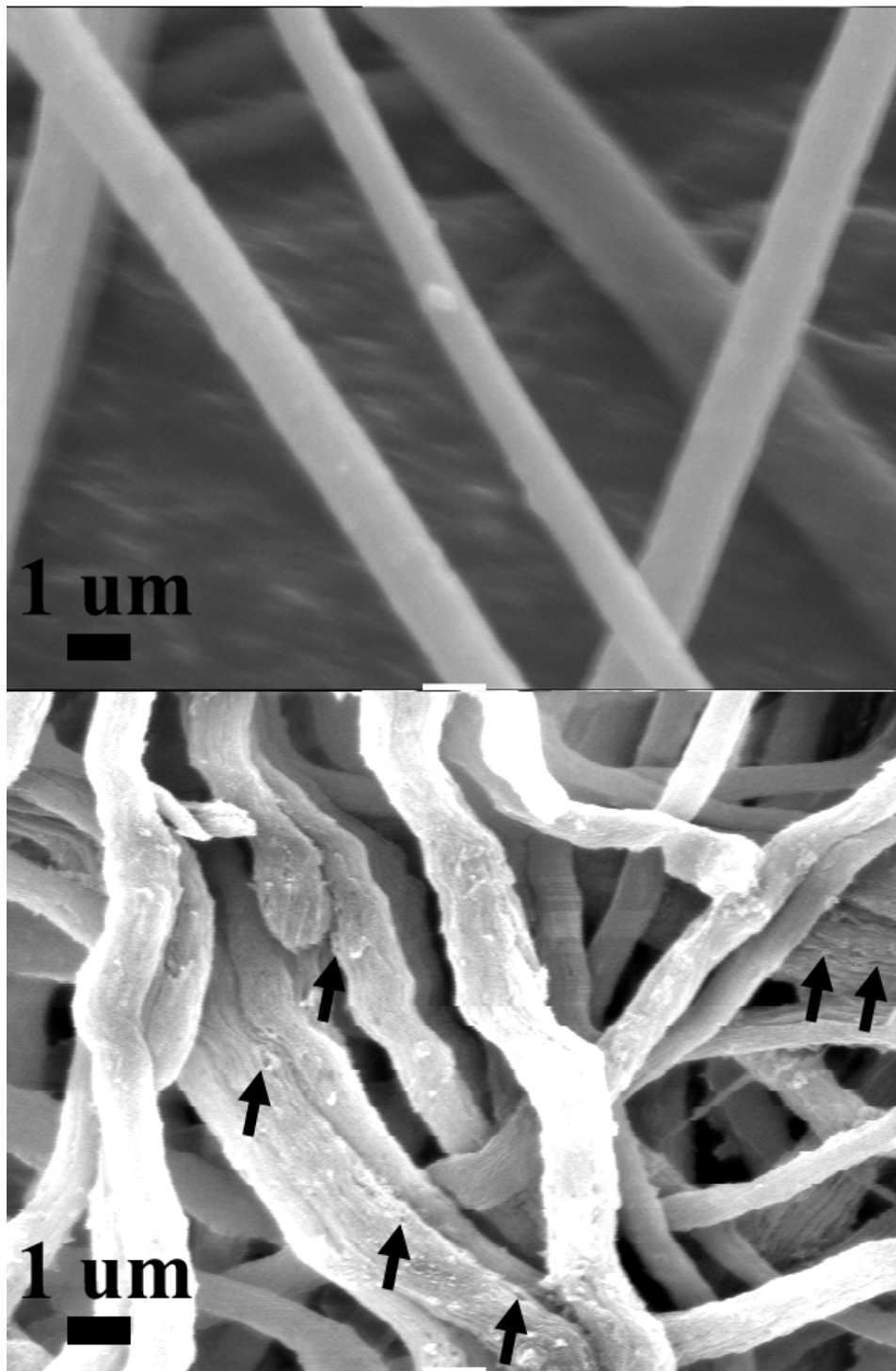
Figure 6.2 SEM Images of Fibers Before and After PVP Elimination. TiO₂-PS-PVP (top) and TiO₂-PS (bottom). Arrows in bottom image point to channels and cavities resembling pores along the fiber surface.
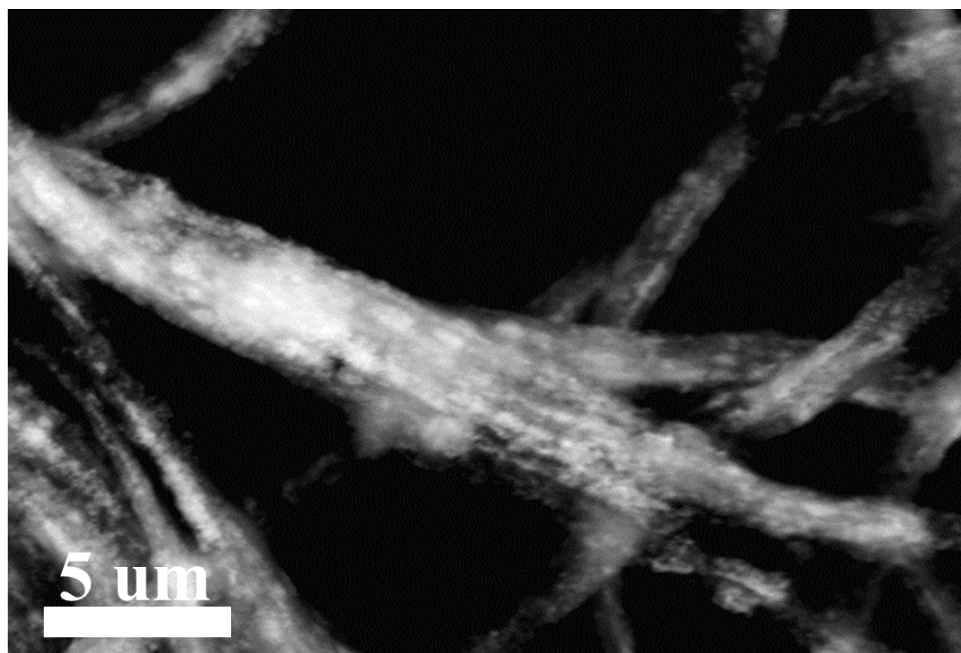
Figure 6.3 Backscatter Mode SEM image of TiO$_2$-PS showing TiO$_2$ distribution inside of polymeric electrospun fiber.

Nitrogen porosimetry carried out at 77 K coupled with BET surface area measurements show consistent isotherm shape for both TiO$_2$-PS-PVP and TiO$_2$-PS (Figure 6.4). The surface area increases sevenfold from 2.1 m^2/g to 14.6 m^2/g after PVP elimination (Table 6.1). The amount of nitrogen taken up by TiO$_2$-PS is higher than that of TiO$_2$-PS-PVP due to the decrease of polymer mass relative to TiO$_2$ caused by PVP removal in addition to the increased porosity of the TiO$_2$-PS compared to dense TiO$_2$-PS-PVP fibers. Nitrogen sorption isotherm hysteresis (loop type H3) indicates slit-shaped pores in TiO$_2$-PS, which are visible in Figure 6.2.[148]

BJH pore size distribution curves (Figure 6.5) show the co-existence of meso- and macro-porosity on the surface of TiO$_2$-PS. Cumulative pore volume of TiO$_2$-PS is 20 times higher than that of TiO$_2$-PS-PVP. Meso- and macro-porosity is established by the Type IV isotherm shown in Figure 6.3. The absence of saturation at partial

127

pressure, $p/p_0 \approx 1$, further confirms the presence of macropores (pores wider than 50 nm).

A variety of pore sizes can be observed on the surface of TiO_2-PS fibers shown in the

SEM image (Figure 6.2). For reference, the As(V) ion is about 0.8 nm in size.[271]
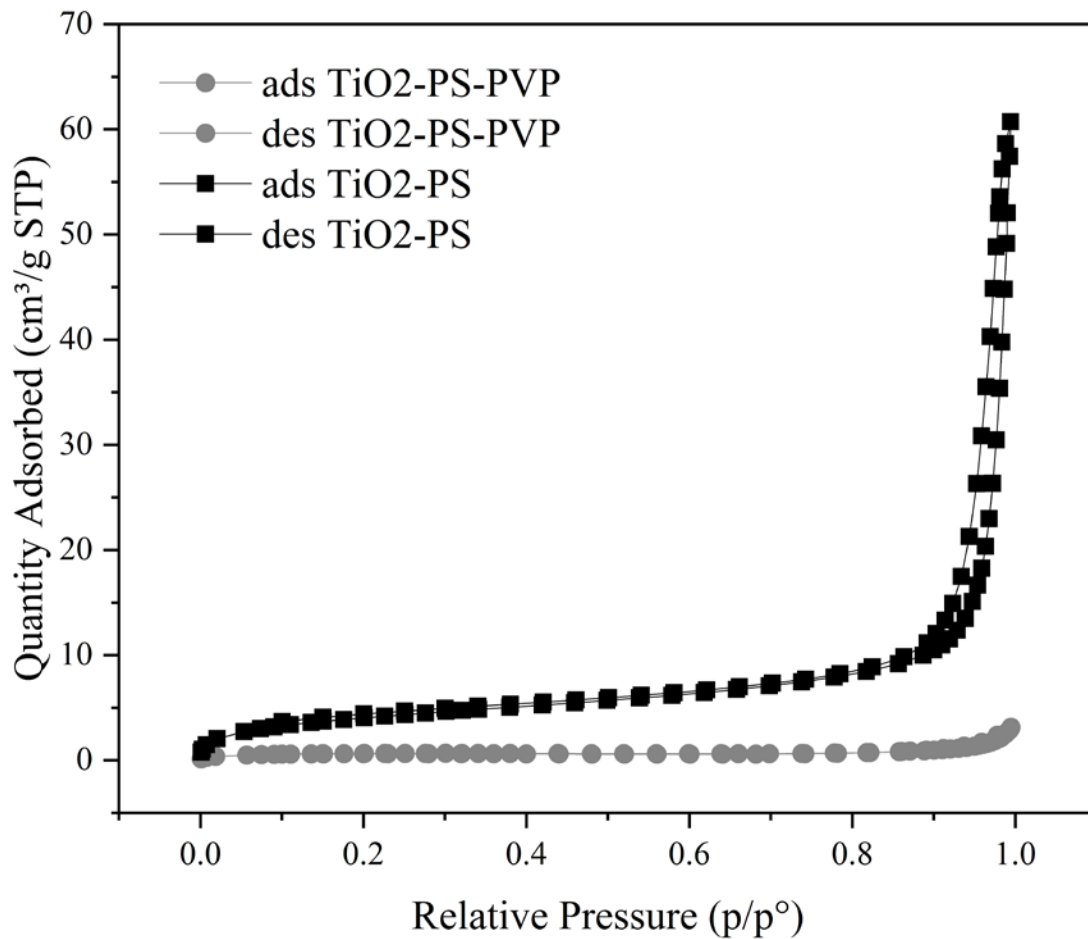
Figure 6.4 Nitrogen Adsorption and Desorption Isotherms for TiO₂-PS-PVP and TiO₂-PS.
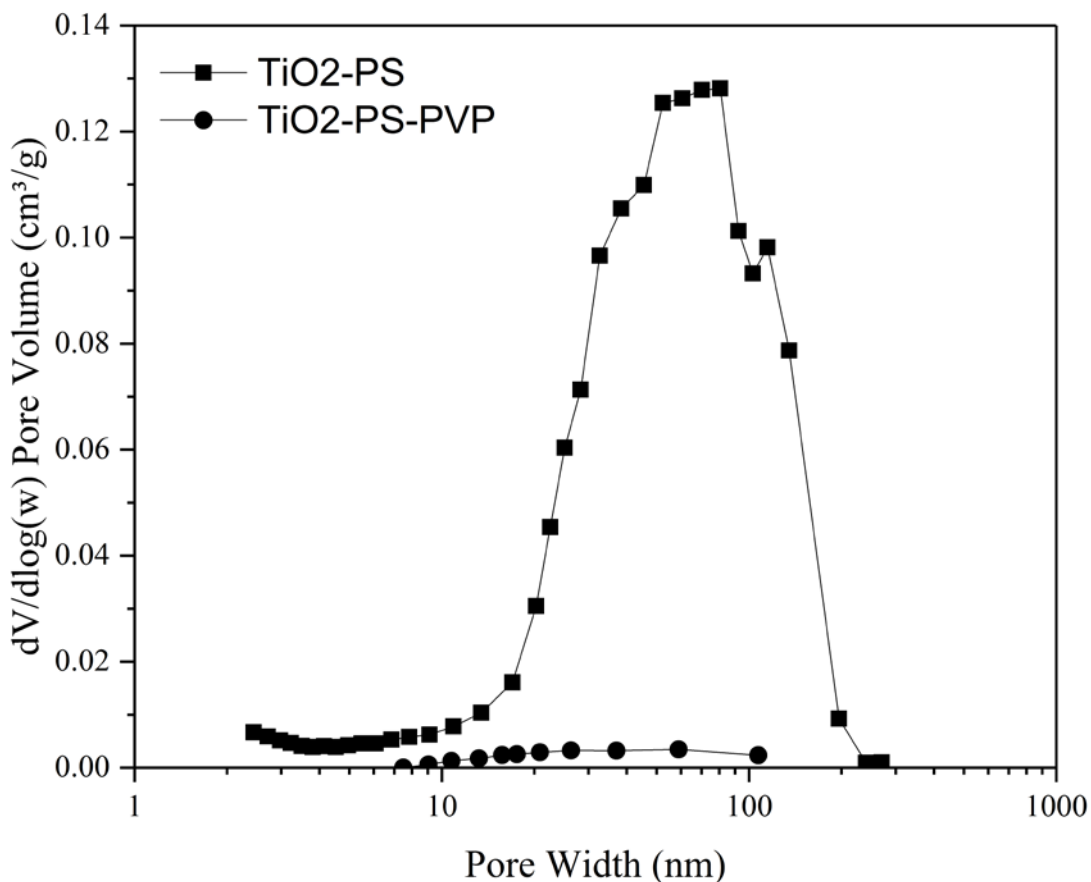
Figure 6.5 BJH Pore Size Distribution Curves for TiO$_2$-PS-PVP and TiO$_2$-PS.

Thermogravimetric analysis (TGA) measurements were utilized to determine the mass composition of neat PS and TiO$_2$-PS fibers. Neat PS and TiO$_2$-PS were degraded completely (Figure D-1) and the final masses were compared. After reaching 500°C, less than 1% of the initial sample mass remained for neat PS, indicating few impurities. The final mass of TiO$_2$-PS fiber samples was 30±0.007%. The final mass of TiO2-PS-GO fibers was 21%±0.02. The sintering temperature of nanoscale TiO$_2$ is above 500°C in helium, thus, the remaining ash was assumed to be TiO$_2$.[272] The calculated TiO$_2$ residual mass is 50%. The discrepancy between theoretical and experimental TiO$_2$ mass percentage values in TiO$_2$-PS is due to residual PVP as proven by FTIR spectra which

show characteristic peaks for PS, TiO$_2$, and PVP (Figure D-2). Characteristic peaks of PS attributable to C-H stretching can be seen around 3000 cm^{-1} and C-C stretching around 1470 cm^{-1}. The TiO$_2$-PS spectrum contains characteristic PS peaks as well as the distinct TiO$_2$ peak between 500-700 cm^{-1}. Characteristic PVP peaks can be seen around 1750 cm^{-1}, 1634 cm^{-1} and 1264 cm^{-1}.[273,274]

To approximate the GO mass present in the final fibers, programmable thermal analysis (PTA) was used for GO-PS and TiO$_2$-GO-PS fibers. Based on multiple measurements of the same fiber, PTA detected 2±0.004% (m/v) GO content in TiO$_2$-GO-PS fibers and 8±0.006% GO in GO-PS fibers (Figure D-3).

6.3.3 Arsenate and pCBA Adsorption Tests

To assess the adsorption capacity of TiO$_2$-PS, varied sorbent dose aqueous phase adsorption isotherm experiments with sodium arsenate were conducted. Batch As(V) adsorption data fit by a Freundlich model are shown in Figure 6.6. Pure TiO$_2$ (P25) served as a benchmark for the performance of TiO$_2$. Previous experiments show that neat PS does not sorb arsenic.[275] The adsorption capacity of TiO$_2$-PS compared to neat PS fibers is attributed to the increase in surface area confirming increased porosity of TiO$_2$-PS composite (14.9 m^2/g) compared to neat PS (6 m^2/g) as well as TiO$_2$-PS-PVP (2.1 m^2/g; shown in Table 1), making TiO$_2$ surface area more accessible to pollutant molecules and facilitating mass transport from bulk solution to NM surface.

For an equilibrium As(V) concentration of 10 µg/L, q$_{TiO2-PS}$ was 1x10^{-3} µg As/mg TiO$_2$ and 8x10^{-5} µg As/mg TiO$_2$ for q$_{TiO2}$ (complete data table in Figure D-4). This

provides evidence that TiO_2 surface area accessible to As(V) was created through the use of PVP as a porogen. It is possible that improved washing could improve performance by further eliminating the PVP.

TiO_2-PS had higher adsorption capacity at pseudo-equilibrium conditions (C_e) to TiO_2 alone. A One-way ANCOVA was conducted to determine a significant difference between TiO_2 and TiO_2-PS adsorption capacity controlling for equilibrium arsenic concentration. There is a significant effect of sorbent composition on adsorption capacity (q_e, μg/g) after controlling for arsenic equilibrium concentration (C_e, mg/L), $F_{(2,21)}=699.49$, $p<0.05$. Adsorption experiments were conducted at pH 7 ± 0.1. Freundlich isotherm adsorption parameters are summarized in Table 1. Since arsenate is characterized with a p$K_{a2\text{-Arsenate}}$ of 6.8 and a p$K_{a3\text{-Arsenate}}$ of 11.6, the dominant species between pH 6 and 9 are $H_2AsO_4^-$ and $HAsO_4^{2-}$. The TiO_2-PS composite showed a lower Freundlich intensity parameter (n) to the TiO_2 isotherm, but contained less sorbent mass (TiO_2). The adsorption capacities per mass of adsorbent were in the order of TiO_2-PS > TiO_2 > neat PS.
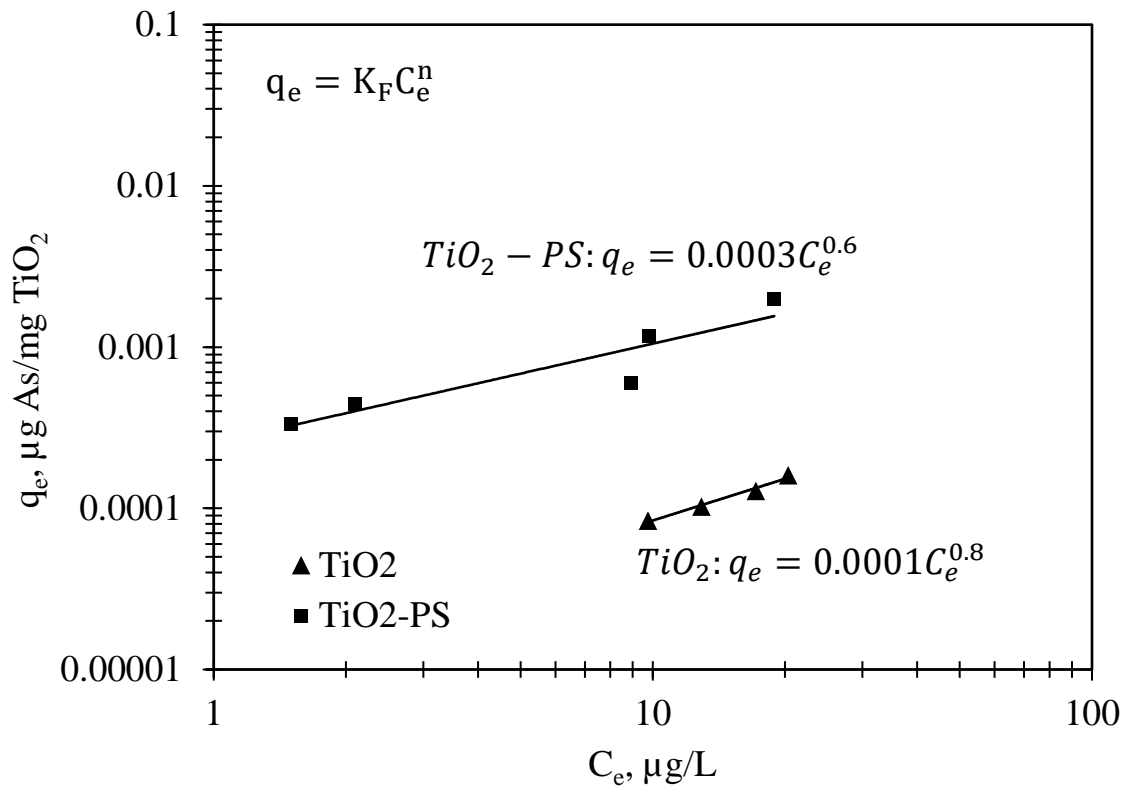
Figure 6.6 Experimental Isotherm Data Summary of TiO$_2$ and TiO$_2$-PS (pH 7±0.1, initial arsenate concentration: 20 ppb).

DCBR experiments were conducted over 10 days using 10 mM NaHCO$_3$ buffered nanopure water solution with initial arsenate concentration C$_0$=20 ppb based on 50% sorbate removal at equilibrium (C$_e$/C$_0$=0.5) while simulataneously simulating realistic water quality conditions (Figure 6.7).[253]
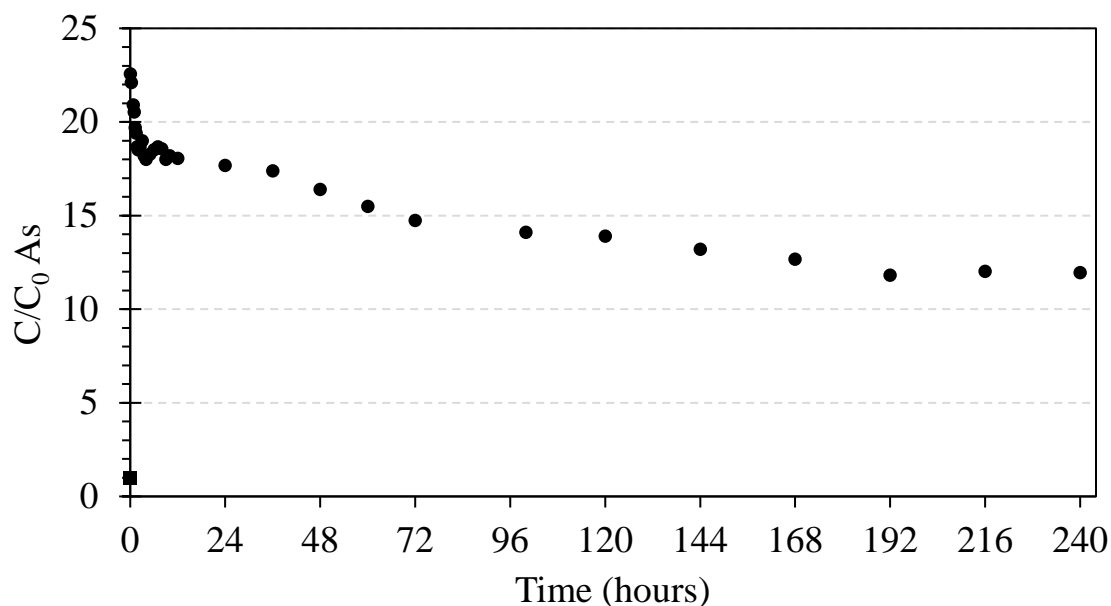
Figure 6.7 Observed TiO$_2$-GO-PS DCBR data arsenate adsorption on (pH 7±0.1, initial arsenate concentration: 20 ppb).

A single-point As(V)/pCBA removal test was conducted using GO-PS, GO-TiO$_2$-PS, and neat PS. Figure 6.8 shows adsorption of arsenic by TiO$_2$-GO-PS but not neat polymer fibers or GO-PS. pCBA was adsorbed by all GO-containing fibers. Some removal of pCBA by neat polymer fibers may be attributed to electrostatic effects. Removal of both arsenic and pCBA by NM-PS fibers were found to be significantly different from that of neat polymer fibers (p<0.05). Error bars shown are one standard deviation based on triplicate samples. Kinetics testing of pCBA removal by TiO$_2$-GO-PS was conducted using a Differential Batch Reactor Column (DCBR) in the same batch as the arsenate DCBR test previously described. pCBA was removed to about half of its initial concentration over a period of 10 days (Figure 6.9). pCBA has been found to sorb favorably to GO with similar surface profile between pH 7-10. Oxygen groups on the GO surface make GO hydrophilic and easily dispersable; however, these groups have been

133

found to play a limited role in pCBA adsorption by GO. Instead, hydrophobic effects were found to be the main mechanism of pCBA, followed by electrostatic repulsion.[267] This would explain the removal of pCBA by neat polymer fibers.

TiO$_2$ leaching was tested using aliquots collected at the conclusion on both the single-point removal test and the DCBR. ICP-MS analysis showed 16 µg/L Ti concentration after 10 days.
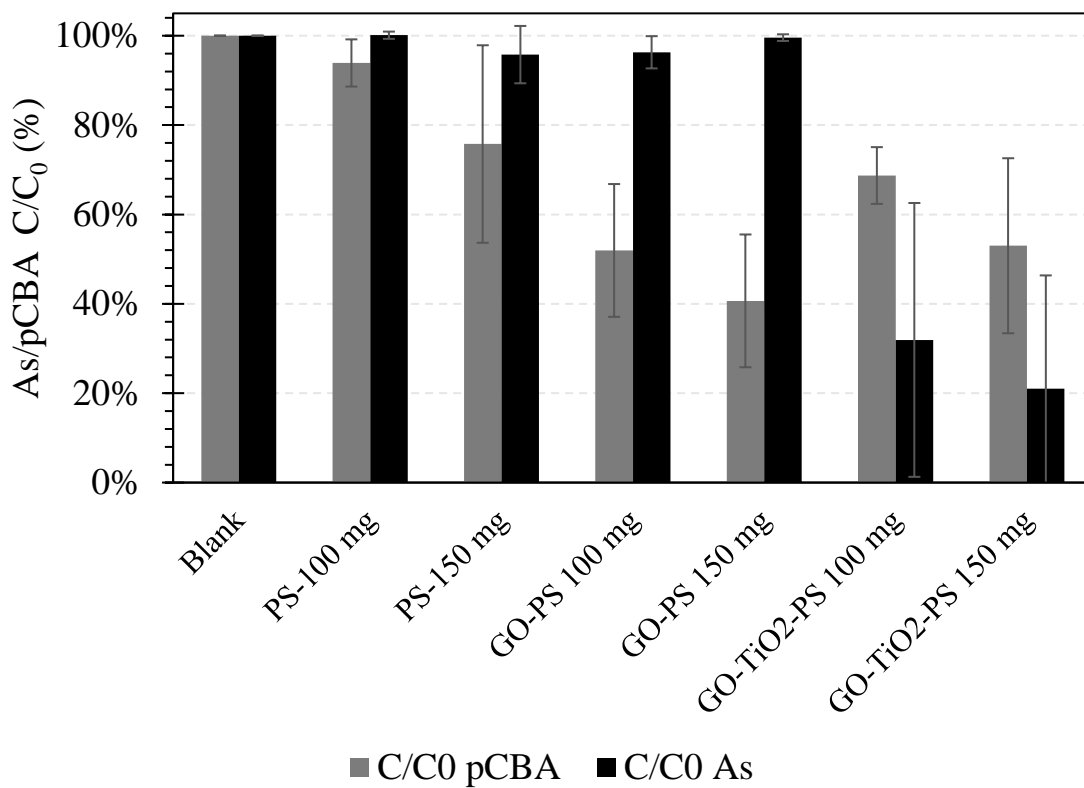
Figure 6.8 Single-point removal test of pCBA and arsenate by neat PS, GO-PS, and TiO2-GO-PS Equilibrium time ≈ 120 hours.
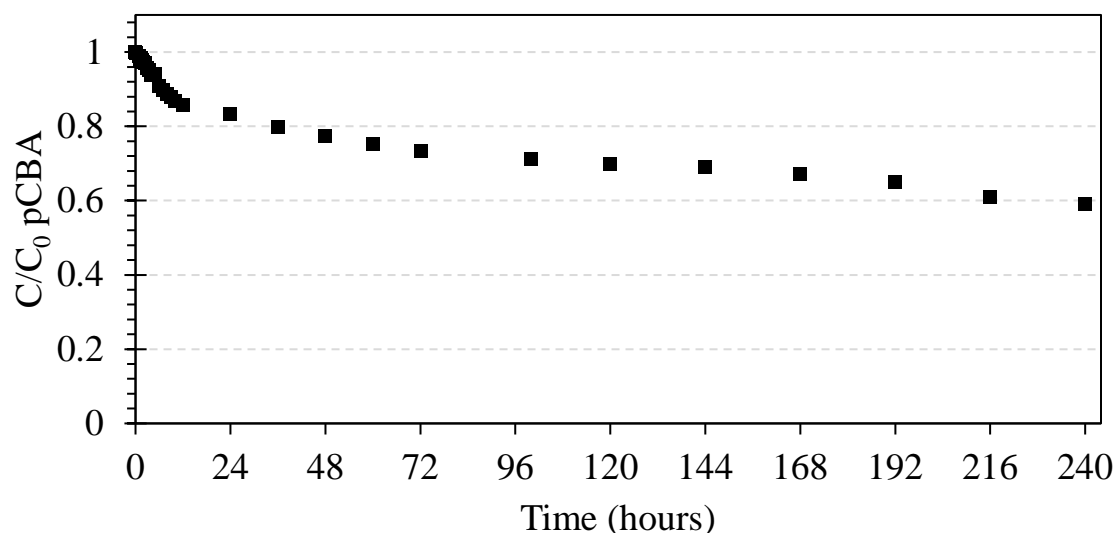
Figure 6.9 Observed TiO2-GO-PS DCBR data for pCBA adsorption (pH 7±0.1, initial arsenate concentration: 20 ppb; initial pCBA concentration = 1 mg/L).

This data suggests that the changes in the dispersion state of the TiO_2 particles in the electrospun polymeric matrix (as opposed to being suspended in water) coupled with electrostatic interactions compensates for the potential losses and blockage of surface area due to partial coating of TiO_2 surface by polymer. Previous work has shown similar results using superfine powdered activated carbon (SPAC) and polystyrene.[282] In this study, nanoscale titanium dioxide and graphene oxide were incorporated into polystyrene solution and co-spun with polyvinylpyrrolidone as a porogen to increase TiO_2 surface area available for arsenic adsorption. The use of a water-soluble polymer as a porogen streamlined the functionalization of the polymeric fiber architecture for use as an adsorbent for aqueous pollutants by producing a micro- and meso-porous fiber architecture which allowed the embedded TiO_2 to sorb arsenic from solution. This nanocomposite has application potential in both water and air treatment as a porous

135

material which can be easily adapted for a number of different pollutants. Future work includes fine-tuning polymer ratios and incorporating alternative polymers and nanomaterials. Additional studies are also required to explain the interactions of metal oxide and carbon-based nanomaterials and polymers at the intermolecular level during electrospinning.

6.4 Summary & Conclusions

- Porous TiO_2-GO-PS nanocomposite sorbent was fabricated via electrospinning in a single step using PVP as a porogenic sacrificial polymer which was eliminated via dissolution during application
  - FTIR and TGA data indicated about 20% (w/w) PVP remained after elimination;
  - Fiber diameter (<1.5 µm) did not change significantly after PVP elimination;
  - Surface area decreases with TiO_2 and PVP addition. Neat PS BET surface area was found to be 6 m^2/g, then decreased to 2 m^2/g as TiO_2-PVP-PS, and then increased sevenfold with PVP elimination: TiO_2-PS-PVP (2 m^2/g) < neat PS (6 m^2/g) < TiO_2-PS (15 m^2/g);
  - Cumulative pore volume of TiO_2-PS 20 times higher than that of TiO_2-PS-PVP.
- TiO_2-PS nanocomposite sorbent performance was comparable to non-embedded TiO_2 performance in arsenic adsorption batch tests
  - Freundlich fit parameters for TiO_2-PS: K=7.2, 1/n=0.4; TiO_2: K=0.75, 1/n=0.42
- In a single-point removal test, GO-TiO_2-PS removed 30-40% of pCBA, while GO-TiO2-PS removed 50-60% pCBA and 70-80% arsenic.

- DCBR testing showed up to 50% removal of arsenic and 60% removal of pCBA by GO-TiO$_2$-PS over 10 days.

- PSDM modeling calculated pore diffusion coeffiicient D$_p$≈1.5x10^{-7} cm^2/s.

- Fibers with TiO$_2$ and GO with porous PS can be fabricated to remove both a model organic and inorganic anionic pollutant.

Research Question 5:

Does the use of a sacrificial polymer as a porogen during electrospinning induce the production of meso- and macropores in a TiO_2-PS electrospun fiber?

Hypothesis 5:

PVP will act as a template for pores in TiO_2-PS fiber. By manipulating the phase separation process between the two polymers during and after electrospinning, a unique meso- and macroporosity will remain on the surface of the TiO_2-PS fiber after PVP elimination via dissolution.

Pore size, frequency, and tortuosity are important attributes of adsorbent materials used for contaminant remediation. The characteristics of pores dictate transport of contaminants out of aqueous matrices, specifically diffusion. The pore structure of a material determines how much of a contaminant it can adsorb.[51] Meso- and macroporous materials allow molecules such as arsenate ($d_{As} \approx 0.8$ nm) to travel from the surrounding aqueous matrix into the sorbent material where adsorption can take place. Experimental work from the previous chapters eliminated the possibility of depending on the volatilization of the organic solvent (DMF) in the precursor solution as being a sufficient force to form the desired meso- and macroporosity required. By co-spinning with PVP, the PVP and PS chains wrap around each other during solution mixing in such a way that the sacrificial polymer acts as a template for free surface area which can be achieved by dissolving the PVP during the adsorption step. This condition was verified via nitrogen porosimetry, SEM imaging, and arsenic adsorption testing, thus *confirming Hypothesis 5.*

139

Research Question 6:

How does the porosity of a TiO$_2$-PS-PVP fiber change before and after PVP elimination?

Hypothesis 6:

As PVP is eliminated from the fiber matrix via dissolution, internal surface area that was previously occupied by the PVP chains will become available, making pore size and number increase and opening slit-like pores in the fiber surface.

The use of sacrificial polymers as templates for the engineering of specific morphologies is important to researchers developing nanoscale technologies as a means for retaining nanomaterial function while anchoring those materials and thus preventing their release. Water treatment applications are uniquely suited for this technique of pore structure manipulation, as the use of water-soluble polymers excludes the need for an additional sacrificial polymer elimination step. Nitrogen porosimetry coupled with BJH model fitting allowed the fiber architectures of TiO$_2$-PS-PVP and TiO$_2$-PS to be compared. Prior to PVP elimination, the polymer nanocomposite surface are is 2 m^2/g, with a smaller (0.0044 cm^3/g) differential pore volume primarily between 10-100 nm wide available for pollutant transport. After PVP elimination, surface area increases to 15 m^2/g, and the pore volume distribution expands to sizes between 1-200 nm wide while the cumulative volume of pores increases 20 times (0.093 cm^3/g), showing a peak between 30-70 nm width pores. SEM imaging shows not only round pore surface structures on TiO$_2$-PS fibers but also long, slit-like structures which were not visible on TiO$_2$-PS-PVP fibers at the same magnification, thus *confirming Hypothesis 6.*

140

Research Question 7:

Does the sacrificial polymer method used in TiO$_2$-PS fibers, GO-PS fibers, and TiO$_2$-GO-PS fibers facilitate adsorption of representative oxo-anions (arsenate) and polar organic (pCBA) pollutants?

Hypothesis 7:

Using the sacrificial polymer method will make GO and TiO$_2$ surface area available for adsorption of arsenate and pCBA

Bottle point and DCBR arsenic and pCBA adsorption experiments were used to investigate and compare adsorption performance using Freundlich isotherm parameters and adsorption kinetics models for arsenate and pCBA. TiO$_2$ was used as the benchmark material for isotherms given that its entire surface would be exposed to the aqueous matrix, where the embedded TiO$_2$ was hypothesized to experience some adsorption capacity losses due to surface blockage by polymer molecules. Freundlich isotherm fits of adsorption experiment data yielded similar performance for both TiO$_2$ and TiO$_2$-PS. TiO$_2$ and TiO$_2$-PS both generated favorable energies of adsorption (1/n=0.42 for TiO$_2$, 1/n=0.4 for TiO$_2$-PS). pCBA and arsenate single-point removal experiments showed that GO-Ps and TiO2-GO-PS are both capable of adsorbing statistically significant amounts of both pollutants, *confirming Hypothesis 7.* Further, kinetics experiments confirmed that pCBA and arsenate can be removed by TiO$_2$-GO-PS in a DCBR configuration. Kinetic modeling of arsenate adsorption onto these fibers confirmed intraparticle diffusion as the dominant adsorption mechanism.

CHAPTER 7

DISSERTATION SYNTHESIS

7.1 Introduction

This chapter summarizes the dissertation and lists research hypotheses presented in this document as well as brief synopses of their answers. Section 7.2 summarizes how this document answered the overarching research question. Section 7.3 lists publications and conference proceedings where the findings in this dissertation were disseminated.

7.2 Answering the Research Question

The objective of this dissertation is to address the overarching question:

How can the surface area of nanomaterials available for reactions with target molecules be maximized without compromising the integrity of the electrospun polymeric adsorbent?

Each research question and hypothesis has made a contribution to answering the primary question. Here, a cohesive narrative is presented around the investigation of the question.

Research Question 1 asked if nanomaterial loadings below 5% (w/v) would increase electrospinning solution viscosity, therefore increasing the voltage required to produce a Taylor cone and increase fiber diameter. This project began with the construction of an

electrospinning apparatus from various individual components, as opposed to purchasing a conventional electrospinning device built specifically for this purpose, due to costs. Once the electrospinning apparatus setup and wiring was complete, various polymers and organic solvents were tested in different ratios in order to produce a continuous fiber. Two solutions, one of 20% (w/v) of PS in DMF and the other 20% (w/v) PVP in DMF, were chosen as the polymeric scaffold material. Next, nanomaterials were added in different mass ratios (based on polymer content) in order to observe the effect of nanomaterial loading. *Hypothesis 1 was partially confirmed* when 5% (w/v) nanomaterial dispersions in both PS and PVP showed increased viscosity and required higher critical voltage to produce a Taylor cone versus 0.5% and 0.05% (w/v). Fiber diameter decreased with increasing nanomaterial loading as a product of increased viscosity and surface tension in the charged jet during fiber spinning. Nanomaterial distribution was conserved throughout the spinning process. Research Question 2 asked if a composite fiber porous enough to act as an adsorbent could be produced in one step, without post-electrospinning processing. A TiO_2-PS fiber was tested as a sorbent for arsenic. The fiber failed to adsorb arsenic, indicating that the material was not porous, therefore *rejecting Hypothesis 2*. This project led to the conclusion that, although nanomaterials could be successfully incorporated into electrospun fibers, the fiber would not necessarily be porous enough to provide access points between a pollutant in an aqueous matrix and the reactive nanomaterial inside. Thus, an investigation into methods of increasing the porosity of electrospun fibers began.

Research Questions 3 and 4 moved from metal oxide nanomaterials to carbon-based nanomaterials (CNM). First, Research Question 3 asked if a known sorbent, superfine

powdered activated carbon, could be incorporated into electrospun PS fibers in a single step and preserve the accessibility of SPAC's inner pore network as part of the larger composite material. This would be done without post-electrospinning processing. The sorptive function of SPAC would be at least preserved as the SPAC would be anchored to the polymer network. *Hypothesis 3 was confirmed* by the porous structure seen in the SEM micrographs of the SPAC-PS composite, and further confirmed by both nitrogen adsorption-desorption experiments coupled with BET surface area modeling and PNT adsorption experiments. The SPAC-PS had six times higher BET surface area than the neat PS fiber and 30% higher adsorption capacity (based on percent difference in average q_e) for PNT. Research Question 4 moved from using SPAC as an additive to using three carbon-based nanomaterials with different geometries: C_{60} fullerenes as a zero-dimensional (0D) material, multiwalled carbon nanotubes as a one-dimensional (1D) material, and graphene platelets as two-dimensional (2D) material. The porous nature of CNMs coupled with the variation in geometry was hypothesized to lead to distinct fiber morphologies, specifically, that the fiber pore diameter and frequency would increase with increasing dimensionality based on higher numbers of edge and corner electrons available for reaction, and further, that DMF volatilization from within the CNM in the interior of the polymer jet coupled with phase separation and rapid solidification would produce inter-connected pore networks within the fibers. *Hypothesis 4 was rejected* based on nitrogen adsorption-desorption experiments with BET surface area modeling coupled with PNT adsorption testing. The surface area of PS fibers decreased with the addition of C_{60} fullerenes, multiwalled carbon

nanotubes, and graphene platelets, and the PNT adsorption capacity did not significantly

increase with the addition of CNM to electrospun fibers based on kinetics experiments.

Research Questions 5, 6, and 7 take a closer look at making the nanomaterials

enmeshed inside electrospun polymeric fibers more accessible by the aqueous matrix and

thus, the target pollutant (in this case, arsenic). Research Questions 5 and 6 explored the use

of a water-soluble polymer, PVP, as a porogen to induce a micro- and meso-porous fiber

architecture by manipulation of phase separation. It was hypothesized that the separation of

the two polymers would leave behind a micro- and macro-porous morphology which would

further expose TiO_2 enmeshed inside the fiber to the aqueous matrix (Hypothesis 5), and

that using PVP as a template would increase the surface area of the fiber after PVP

elimination (Hypothesis 6). *Hypothesis 5 was confirmed* by nitrogen adsorption and

desorption experiments coupled with BET surface area and BJH pore size analysis. BJH

pore size distribution curves show the co-existence of meso- and macro-porosity on the

surface of TiO_2-PS. Meso- and macro-porosity is established by the Type IV isotherm

acquired using the BET model, as well as BJH model fitting of the data. The absence of

saturation at partial pressure of the nitrogen isotherm, $p/p_0 \approx 1$, further confirms the presence

of macropores (pores wider than 50 nm). A variety of pore sizes can be observed on the

surface of TiO_2-PS fibers is shown in SEM images as well. Finally, Research Question 7

takes the application of a TiO_2-PS fiber as a sorbent for arsenic and compares it to

nanoscale TiO_2, a known adsorbent. Arsenic and pCBA adsorption experiments coupled

with Freundlich equation fitting *confirmed Hypothesis 7*, as TiO_2-PS matched the

performance of TiO_2 in a batch reactor adsorption test and TiO_2-GO-PS removed both

145

arsenate and pCBA to $C/C_0=0.5$ over a 10-day runtime with negligible NM leaching. Intraparticle diffusion was confirmed as the dominant adsorption mechanism using DCBR testing and kinetics modeling.

The discoveries described in the previous chapters can be synthesized into a clear strategy for fabrication of NM-polymer electrospun fibers for adsorption applications. The conclusions that emerge from the work in this dissertation are as follows:

First, viscosity, critical voltage, and fiber diameter increased with NM addition. SPAC addition to electrospun PS fibers made a sorbent which showed higher adsorption capacity for phenanthrene than neat PS. However, CNM-PS fibers did not show better PNT adsorption performance than neat PS. This may have had to do with the higher surface area-to-volume ratio of NM compared to SPAC as well as the low mass composition of CNM in the fiber. 30% (m/m) NM composition was achieved with titanium dioxide in Research Question 5. In order to make adsorption sites of embedded NM available for adsorption, the use of a porogen or other post-spinning processing is required, as shown in Research Questions 1 and 4. TiO2-PS fiber without a porogen did not sorb arsenic, as shown in RQ1, but had a maximum arsenic adsorption capacity of 0.2 mg As/g TiO_2 when a porogen was used (RQ7), comparable to that of suspended TiO_2. Using a water-soluble polymer as a porogen for adsorption applications is a method of incorporating the sacrificial polymer step without any additional fiber processing. Research Questions 5, 6, and 7 showed that the sacrificial polymer method using PS and PVP significantly increases pore volume and embedded NM sites available for adsorption of arsenic. Using PVP and PS in a 1:1 ratio affords a meso- and macro-porous structure not achieved with PS alone. Further, the

146

adsorption capacity of TiO_2-PS using the sacrificial polymer method was comparable to that of suspended TiO_2, confirming that the sacrificial polymer method preserves TiO_2 and GO adsorption sites even as it is embedded in the polymer support. Future work described in Chapter 8 will further advance the fabrication and application of electrospun fibers for water treatment applications.

7.3 Publications and Conference Proceedings

7.3.1 Publications

Published

Apul, O., Hoogesteijn von Reitzenstein, N., Schoepf, J., Ladner, D., Hristovski, K., Westerhoff, Superfine Powdered Activated Carbon Incorporated into Electrospun Polystyrene Fibers Preserve Adsorption Capacity. *Science of the Total Environment,* March 2017.

Hoogesteijn von Reitzenstein, N., Bi, X., Yang, Y., Hristovski, K., and Westerhoff, P. Morphology, structure, and properties of metal oxide/polymer nanocomposite electrospun mats. *Journal of Applied Polymer Science,* April 2016.

Provisional Patent Filing

"Non-Water Soluble Electrospun Polymeric Porous Fibers Containing Nanoparticles to Purify Water," U.S. Provisional Pat. Ser. No. M16-343P, filed June 16, 2017.

In Preparation

Hoogesteijn von Reitzenstein, N., Apul, O., Pruitt, E., Hristovski, K., Westerhoff, P. Morphology of Polymeric Electrospun Fibers Containing 0D Buckminster Fullerene, 1D Multiwalled Carbon Nanotubes, and 2D Graphene Oxide Nanomaterials. In preparation for submission to: *Journal of Applied Polymer Science*.

Hoogesteijn von Reitzenstein, N., Pruitt, E., Hristovski, K., Westerhoff, P. Hierarchical Pore Structures of Electrospun Titanium Dioxide Nanocomposites for Arsenate Removal. In preparation for submission to: *Small*.

7.3.2 Conference Talks, Poster Presentations, and Seminars

Oral Presentations

Hoogesteijn von Reitzenstein, N., Hristovski, K., Westerhoff, P. Electrospun Polymer-Supported Nanocomposites for Water Treatment. Sustainable Nanotechnology Organization Conference, Portland, OR, November 7-10, 2015.

Hoogesteijn von Reitzenstein, N., Hristovski, K., Westerhoff, P. Applications and Implications of Nanotechnology in the Environment: Polymer-Supported Nanocomposite Fibers, Reactive Oxygen Species, and Phase Distributions. Arizona State University Civil & Environmental Engineering Seminars, Tempe, AZ, May 10, 2015.

Hoogesteijn von Reitzenstein, N., Hristovski, K., Westerhoff, P. Nano-Enabled Polymer Hybridized Mats for Water Treatment. AZ Water 89th Annual Conference, Glendale, AZ. Thursday May 12, 2016.

Poster Presentations

Hoogesteijn von Reitzenstein, N., Hristovski, K., Westerhoff, P. Effect of Indium Nanoparticles on Electrospun Polyvinylpyrrolidone Fiber. Sustainable Nanotechnology Organization Conference, Boston, MA. November 2-4, 2014.

Hoogesteijn von Reitzenstein, N., Hristovski, K., Westerhoff, P. Integration of Metal oxide Nanoparticles into Electrospun Polyvinylpyrrolidne and Polystyrene Fibers. Arizona State University Ira A. Fulton Schools of Engineering Civil, Environmental & Sustainable Engineering Graduate Symposium, Tempe, AZ. March 2015.

Hoogesteijn von Reitzenstein, N., Hristovski, K., Westerhoff, P. Integration of Metal oxide Nanoparticles into Electrospun Polyvinylpyrrolidone and Polystyrene Fibers. Gordon Research Conference: Environmental Nanotechnology. Burlington, VT. July 2015.

Hoogesteijn von Reitzenstein, N., Hristovski, K., Westerhoff, P. Nano-Enabled Polymer Hybridized Mats for Water Treatment Systems. AZWater Research Workshop, January 2016.

Hoogesteijn von Reitzenstein, N., Apul, O., Pruitt, E., Hristovski, K., Westerhoff, P. Morphology of Polymeric Electrospun Fibers Containing 0D Buckminster Fullerene, 1D Multiwalled Carbon Nanotubes, and 2D Graphene Oxide Nanomaterials. American Chemical Society 253rd National Meeting & Exposition: Advanced Materials, Technologies, Systems, and Processes. April 2-6, 2017.

CHAPTER 8

SUMMARY, CONCLUSIONS, AND FUTURE RESEARCH NEEDS

This chapter provides a summary of key experimental and modelling observations, then answers seven Research Questions.

8.1 Summary

Chapter 3: Morphology, Structure, and Properties of Metal Oxide/Polymer Electrospun Mats

- Effect of 0-5% (w/v) metal oxide NP (TiO_2, In_2O_3) addition to PS fibers on viscosity, critical voltage, and fiber morphology was investigated;

- Viscosity and critical voltage increased with increasing weight percentage of NP in polymer solution;

- Critical voltage needed to produce Taylor cone was higher for PS than for PVP;

- A 50% increase in fiber diameter for 5% (w/v) was observed as a result of increased viscosity and surface tension; otherwise no significant differences observed;

- Even distribution of NP in fibers was observed.

Research Question 1:

Do metal oxide nanoparticle loadings at 0.05, 0.5, and 5% (m/v) increase electrospinning solution viscosity, increase voltage required to observe a Taylor cone, or increase electrospun fiber diameter?

Hypothesis 1:

Adding nanomaterials of any quantity will increase solution viscosity, therefore requiring higher voltage and resulting in larger fiber diameters than neat polymer fibers.

This project began with the construction of an electrospinning apparatus from various components due to cost restraints, as opposed to purchasing a conventional electrospinning device built specifically for this purpose. Once the electrospinning apparatus setup and wiring was complete, various polymers and organic solvents were tested in different ratios in order to produce a continuous fiber. Two solutions, one of 20% (m/v) of PS in DMF and the other 20% (m/v) PVP in DMF, were chosen as the polymeric scaffold material. Next, nanomaterials were added in different mass ratios (based on polymer content) in order to observe the effect of nanomaterial loading. *Hypothesis 1 was partially confirmed* when nanomaterial dispersions above 5% (w/v) in both PS and PVP showed increased viscosity and required higher critical voltage to produce a Taylor cone. Fiber diameter decreased with increasing nanomaterial loading as a product of increased viscosity and surface tension in the charged jet during fiber spinning. Nanomaterial distribution was conserved throughout the spinning process.

Research Question 2:

151

Research Question 2: Can metal oxide nanomaterials be incorporated into electrospun fibers without post-spinning treatment to enable arsenate adsorption by the composite nanofiber?

Hypothesis 2:

The use of volatile organic solvents, such as Dimethylformamide (DMF), will induce a fiber surface porosity which will provide access points for target contaminants, such as Arsenic, to be removed from aqueous solution via nanosorbents (TiO_2) embedded in the fiber.

A TiO_2-PS fiber was tested as a sorbent for Arsenic. The fiber failed to adsorb Arsenic, leading to the conclusion that the material was not porous, therefore *rejecting Hypothesis 2*. This project led to the conclusion that, although nanomaterials could be successfully incorporated into electrospun fibers, the fiber would not necessarily be porous enough to provide access points between a pollutant in an aqueous matrix and the reactive nanomaterial inside. Thus, an investigation into methods of increasing the porosity of electrospun fibers began.

Chapter 4: Superfine Powdered Activated Carbon Incorporated into Electrospun Polystyrene Fibers Preserve Adsorption Capacity

- Effect of 5% (w/v) superfine powdered activated carbon (SPAC) addition to polystyrene (PS) electrospun fibers and subsequent performance of fibers as phenanthrene (PNT) sorbent were investigated

- PTA analysis found 10% (w/w) in fiber

- Using neat PS as reference material, SPAC-PS fiber surface area increased 6 fold (from 6 m^2/g to 43 m^2/g)

- SPAC-PS fibers were found to be porous; accessibility of terminal adsorption sites was conserved

Research Question 3:

Can superfine powdered activated carbon be incorporated into electrospun polystyrene fibers in a single step while preserving accessibility to SPAC's inner pore network?

Hypothesis 3:

Hypothesis 3. SPAC can be incorporated into electrospun polymeric matrices in a single step without post-treatment while preserving accessibility to SPAC's inner pore network.

Hypothesis 3 was confirmed by the porous structure seen in the SEM micrographs of the SPAC-PS composite, and further confirmed by both nitrogen adsorption-desorption experiments coupled with BET surface area modeling and PNT adsorption experiments.

153

The SPAC-PS had six times higher BET surface area than the neat PS fiber and 30% higher adsorption capacity for PNT.

Chapter 5: Morphology of Polymeric Electrospun Fiber Containing Multi-Dimensional Nanomaterials for Water Purification

- Three carbon-based nanomaterials (0D fullerenes, 1D carbon nanotubes, and 2D graphene platelets) were incorporated into polystyrene electrospun fibers and 3 related hypotheses were tested:
  - the porous nature of hybrid CNM composites leads to increases in diameter, pore size, and pore frequency compared to a neat polymer fiber;
  - DMF evaporation from the NM inside the polymer leaves behind inter-connected pores in the solidified polymer; and
  - CNM addition during electrospinning enhances pore formation and improves PNT sorption
- Fiber diameter increased with CNM addition; pore size, pore frequency, and PNT adsorption performance did not change compared to neat PS fibers; no interconnected pores were observed.

Research Question 4:

How does the incorporation of different carbonaceous nanomaterial geometries into electrospun polystyrene fibers change the pore diameter, frequency, or shape?

Hypothesis 4.

The porous nature of hybrid CNM composites leads to increases in diameter, pore size, and number of pores compared to a neat polymer fiber, while Dimethylformamide (DMF) evaporation from the NM inside the polymer leaves behind inter-connected pores in the solidified polymer.

The porous nature of CNMs coupled with the variation in geometry was hypothesized to lead to distinct fiber morphologies, specifically, that the fiber pore diameter and frequency would increase with increasing dimensionality based in increasing edge and corner sites of the CNM, and further, that DMF volatilization from within the CNM in the interior of the polymer jet coupled with phase separation and rapid solidification of the fiber would produce inter-connected pore networks within the fibers. *Hypothesis 4 was rejected* based on nitrogen adsorption-desorption experiments with BET surface area modeling coupled with PNT adsorption testing. The surface area of PS fibers decreased with the addition of C_{60} fullerenes, multiwalled carbon nanotubes, and graphene platelets, and the PNT adsorption capacity did not significantly increase based on kinetics experiments.

156

Chapter 6: Hierarchical Pore Structures of Electrospun Titanium Dioxide Nanocomposites for Arsenate and pCBA Removal

- Porous TiO_2-GO-PS nanocomposite sorbent was fabricated via electrospinning in a single step using PVP as a porogenic sacrificial polymer which was eliminated via dissolution during application
    - FTIR and TGA data indicated about 20% (w/w) PVP remained after elimination;
    - Fiber diameter (<1.5 µm) did not change significantly after PVP elimination;
    - Surface area decreases with TiO_2 and PVP addition. Neat PS BET surface area was found to be 6 m^2/g, then decreased to 2 m^2/g as TiO_2-PVP-PS, and then increased sevenfold with PVP elimination: TiO_2-PS-PVP (2 m^2/g) < neat PS (6 m^2/g) < TiO_2-PS (15 m^2/g);
    - Cumulative pore volume of TiO_2-PS 20 times higher than that of TiO_2-PS-PVP.
- TiO_2-PS nanocomposite sorbent performance was comparable to non-embedded TiO_2 performance in arsenic adsorption batch tests
    - Freundlich fit parameters for TiO_2-PS: K=7.2, 1/n=0.4; TiO_2: K=0.75, 1/n=0.42
- In a single-point removal test, GO-TiO2-PS removed 30-40% of pCBA, while GO-TiO2-PS removed 50-60% pCBA and 70-80% arsenic.

157

- DCBR testing showed up to 50% removal of arsenic and 60% removal of pCBA by GO-TiO$_2$-PS over 10 days

Research Question 5:

Does the use of a sacrificial polymer as a porogen during electrospinning induce the

production of meso- and macropores in a TiO$_2$-PS electrospun fiber?

Hypothesis 5:

PVP will act as a template for pores in TiO2-PS fiber. By manipulating the phase

separation process between the two polymers during and after electrospinning, a unique

meso- and macroporosity will remain on the surface of the TiO$_2$-PS fiber after PVP

elimination via dissolution.

Pore size, frequency, and tortuosity are important attributes of adsorbent materials used for

contaminant remediation. The characteristics of pores dictate transport rates of

contaminants out of aqueous matrices. The pore structure of a material determines how

much of a contaminant it can adsorb.[51] Meso- and macroporous materials allow molecules

such as arsenate ($d_{As} \approx 0.8$ nm) to travel from the surrounding aqueous matrix into the

sorbent material where adsorption can take place. Experimental work from the previous

chapters eliminated the possibility of depending on the volatilization of the organic solvent

(DMF) in the precursor solution as being a sufficient force to form the desired meso- and

macroporosity required. By co-spinning with PVP, the PVP and PS chains wrap around

each other during solution mixing in such a way that the sacrificial polymer acts as a

template for free surface area which can be achieved by dissolving the PVP during the

adsorption step. This condition was verified via nitrogen porosimetry, SEM imaging, and

arsenic adsorption testing, thus *confirming Hypothesis 5.*

Research Question 6:

How does the porosity of a TiO$_2$-PS-PVP fiber change before and after PVP elimination?

Hypothesis 6:

As PVP is eliminated from the fiber matrix via dissolution, internal surface area that was previously occupied by the PVP chains will become available, making pore size and number increase and opening slit-like pores in the fiber surface.

The use of sacrificial polymers as templates for the engineering of specific polymer material morphologies is of particular interest to researchers developing nanoscale technologies as a means for retaining nanomaterial function while anchoring those materials and thus preventing their release. Water treatment applications are uniquely suited for this technique of pore structure manipulation, as the use of water-soluble polymers excludes the need for an additional sacrificial polymer elimination step. Nitrogen porosimetry coupled with BJH model fitting allowed the fiber architectures of TiO$_2$-PS-PVP and TiO$_2$-PS to be compared. Prior to PVP elimination, the polymer nanocomposite surface are is 2 m^2/g, with a smaller (0.0044 cm^3/g) differential pore volume primarily between 10-100 nm wide available for pollutant transport. After PVP elimination, surface area increases to 15 m^2/g, and the pore volume distribution expands to sizes between 1-200 nm wide while the cumulative volume of pores increases 20 times (0.093 cm^3/g), showing a peak between 30-70 nm width pores. SEM imaging shows not only round pore surface

structures on TiO$_2$-PS fibers but also long, slit-like structures which were not visible on

TiO$_2$-PS-PVP fibers at the same magnification, thus *confirming Hypothesis 6.*

Research Question 7: Does the sacrificial polymer method used in TiO$_2$-PS fibers, GO-PS

fibers, and TiO$_2$-GO-PS fibers facilitate adsorption of representative oxo-anions (arsenate)

and polar organic (pCBA) pollutants?

Hypothesis 7:

Using the sacrificial polymer method will make GO and TiO$_2$ surface area available for

adsorption of arsenate and pCBA.

Bottle point and DCBR arsenic and pCBA adsorption experiments were used to investigate

and compare adsorption performance using Freundlich isotherm parameters and adsorption

kinetics models for arsenate and pCBA. TiO$_2$ was used as the benchmark material for

isotherms given that its entire surface would be exposed to the aqueous matrix, where the

embedded TiO$_2$ was hypothesized to experience some adsorption capacity losses due to

surface blockage by polymer molecules. Freundlich isotherm fits of adsorption experiment

data yielded similar performance for both TiO$_2$ and TiO$_2$-PS. TiO$_2$ and TiO$_2$-PS both

generated favorable energies of adsorption (1/n=0.42 for TiO$_2$, 1/n=0.4 for TiO$_2$-PS).

pCBA and arsenate single-point removal experiments showed that GO-Ps and TiO2-GO-PS

are both capable of adsorbing statistically significant amounts of both pollutants,

confirming Hypothesis 7. Further, kinetics experiments confirmed that pCBA and arsenate

can be removed by TiO$_2$-GO-PS in a DCBR configuration. Kinetic modeling

8.2 Conclusions

The overarching research question posed and answered by this dissertation is:

How can the surface area of nanomaterials available for reactions with target molecules be maximized without compromising the integrity of the electrospun polymeric support?

This question was divided into 7 specific research questions and corresponding hypotheses, discussed in detail in the previous chapters. Nanomaterials were incorporated into electrospun polymeric fibers successfully while retaining their sorptive function with some changes to the electrospinning process used to spin neat polymer fibers, such as increasing spinning voltage. The addition of nanomaterials to polymeric electrospun fibers increased precursor solution viscosity and fiber diameter. Metal oxide nanomaterials were incorporated into electrospun polymeric fibers at a variety of mass ratios, as the preceding chapters show. Superfine powdered activated carbon preserved its terminal adsorption sites even as it became embedded in a polymer network. Nanomaterial geometry didn't have an effect on final fiber architecture. Nanomaterial sorption performance once embedded in electrospun polymeric networks was comparable to that of non-embedded nanomaterial for both a model hydrophobic organic pollutant and a model heavy metal. Synthesis methods were improved to facilitate adsorption of pollutants by incorporating a water-soluble polymer as a porogen, therefore streamlining the optimization of fiber architecture for

pollutant mass transfer from the aqueous matrix to the embedded nanomaterial without compromising the mechanical integrity of the composite fiber.

8.3 Future Research Needs

The discoveries made in this dissertation are valuable to advancing the state of science for nanocomposite sorbents, but also motivate further questions that should be addressed. The main objective of this dissertation was to find a way to anchor nanomaterials to a support network while retaining their desired function; that was achieved through the exploration of different techniques until the answer was found: using a water-soluble polymer as a porogen and eliminating the porogen during the treatment phase in an effective, streamlined process that did not compromise sorbent integrity or hinder nanomaterial adsorption capacity. Future research needs point to fine-tuning of electrospun nanocomposites for POU/POE applications at three levels. At the molecular level, future work should focus on alternative polymer/nanomaterial combinations to target a wider array of contaminants and make electrospun fibers more versatile. At the electrospinning process level, electrospinning should be modeled and studied in order to understand material deposition on the collector plate and facilitate the control of nanomaterial distribution, and thus, fiber architecture. Finally, at the application level, a reactor design should be refined to fully take advantage of the cylindrical geometry of the nanocomposite fibers.

8.3.1 Increasing versatility

To make electrospun nanocomposites more versatile, alternative polymers and nanomaterials should be fabricated as fibers and tested. The use of different polymers and

nanomaterials in a way that would make the electrospun fiber technology able to target multiple pollutants at once would increase their efficiency and application potential. This would include functionalizing the polymer itself to perform a treatment function, such as ion exchange. By converting or attaching surface groups to the polymer, the capacity of the whole fiber could be improved, as the polymer takes up at least 50% of the sorbent mass. The polymer would then move beyond acting as a support and become part of the reactive surface area available for mass transfer of pollutants out of the target matrix (air or water). This dissertation used polystyrene as the support polymer due to its ubiquity, low price, and legacy as a durable, highly hydrophobic polymer. However, other durable polymers, such as polypropylene, should be explored, especially for applications where the water quality may be highly acidic or otherwise problematic. Further in this vein, more work needs to be done to investigate durable, sustainable polymers and their capabilities as functionalized polymer supports for nanomaterials in POU/POE water treatment applications where spent sorbent fiber disposal to a landfill is unavailable.

8.3.2   Understanding Fiber Deposition Processes

The effect of the high intensity of the electrospinning jet from its exit through the needle tip to its eventual deposition on the collector plate is currently not well understood or fully modeled. Additionally, the relative motion of the jet components (organic solvent molecules, polymer molecules, and nanomaterial molecules) during their trajectory from needle tip to collector plate cannot be predicted. Although this work found good distribution of nanomaterials conserved in both the polymer precursor solution and the final fiber product after sonication, the final mass ratios of nanomaterial content did not quite

match up with the calculated ratios in the final fiber. Given the highly charged environment which electrospinning requires to occur and the different molecular weights of polymer solution components, further investigation into the effect of the electrospinning system on the fiber components at the atomic and electronic level would allow for finer control of fiber architecture, especially in multi-component systems such as polymer nanocomposites. By controlling the architecture of the fiber, nanomaterial distribution and placement can be optimized for surface reactions with target pollutants.

8.3.3 Understanding Physical Orientation of Fiber Components

Adsorption site availability is critical for adsorption of pollutants onto nanomaterials in nanomaterial-polymer fibers. The orientation of sorptive nanomaterials inside the polymer chains is a question whose answer would further improve fiber fabrication and performance. Polymer chains are known to wrap around carbon nanotubes, but investigation into polymer-TiO_2 relationships has not been thoroughly investigated. Establishing a relationship between polymer orientation around TiO_2 particles and polymer precursor solution preparation (for example, polymer mass ratio, stirring velocity or duration, sonication frequency, etc.) would optimize the precursor solution synthesis process to maximize available sorption sites once the fiber has been fabricated. In tandem with the question of nanomaterial orientation with relation to polymer chains in electrospun fibers, the differences in dispersion of TiO_2 in water versus in organic solvent-polymer solution and in the final polymer fiber would further explain differences in adsorption data between suspended TiO_2 and TiO_2-PS.

166

8.3.4 Reactor Design for Optimal Fiber Application

The ultimate utility of electrospun nanocomposite fiber sorbents depends as much on their mode of application as on the conditions of their fabrication. This dissertation tested electrospun fibers as sorbents in a batch reactor. However, experiments indicated that this is not the optimal configuration to fully take advantage of the nano- and micron-scale geometries of electrospun fibers. Much like sonication and functional coatings allow nanomaterial surface area to be better utilized by preventing their aggregation, electrospun fibers must be applied as two-dimensional layers, either horizontally or vertically. A reactor design which takes this quality into account would allow for the full benefit of the electrospun fiber by increasing the surface area of the fiber exposed to the matrix it is meant to treat. By coupling the characteristic rapid kinetics and mass transfer of nanomaterials with the ability of electrospun fibers to be stretched over a wide area, a plug flow reactor design should be investigated as the most functional configuration for sorbent fiber application in a POU/POE system.

The recommendations given for future work in the development of electrospun polymeric nanocomposites will further evolve electrospun fibers as an effective technology for water treatment at the POU/POE level. Electrospinning presents a simple method of anchoring a number of highly specialized, space-efficient materials into a polymer support which will prevent their release into the water supply while retaining their desired function and should be thoroughly explored as a means of developing new treatment technologies.

REFERENCES

(1)   WHO; UNICEF. *Monit. Program. water supply Sanit.* **2014**, 1–78.

(2)   Westerhoff, P.; Alvarez, P.; Li, Q.; Gardea-Torresdey, J.; Zimmerman, J. *Environ. Sci. Nano* **2016**, *3*, 1241–1253.

(3)   Impellitteri, C. A.; Patterson, C. L.; Haught, R. C.; Goodrich, J. A. *Small Drinking Water Systems State of the Industry and Treatment Technologies to Meet the Safe Drinking Water Act Requirements*; Cincinnati, OH, 2007.

(4)   Environmental Protection Agency. *Point-of-Use or Point-of- Entry Treatment Options for Small Drinking Water Systems*; 2006.

(5)   US EPA. Point-of-Use / Point-of-Entry Treatment https://cfpub.epa.gov/safewater/arsenic/arsenictradeshow/arsenic.cfm?action=Point-of-Use.

(6)   Qu, X.; Brame, J.; Li, Q.; Alvarez, P. J. J. *Acc. Chem. Res.* **2012**, *46*, 834–843.

(7)   Gleiter, H. *Acta Mater.* **2000**, *48*, 1–29.

(8)   Yang, K.; Zhu, L. Z.; Xing, B. S. *Environ. Sci. Technol.* **2006**, *40*, 1855–1861.

(9)   Wang, S.; Sun, H.; Ang, H. M.; Tadé, M. O. *Chem. Eng. J.* **2013**, *226*, 336–347.

(10)   Smith, S. C.; Rodrigues, D. F. *Carbon N. Y.* **2015**, *91*, 122–143.

(11)   Hoogesteijn von Reitzenstein, N.; Bi, X.; Yang, Y.; Hristovski, K.; Westerhoff, P. *J. Appl. Polym. Sci.* **2016**, *133*, 1–9.

(12)   Armstrong, M. R.; Shan, B.; Maringanti, S. V.; Zheng, W.; Mu, B. *Ind. Eng. Chem. Res.* **2016**, *55*, 9944–9951.

(13)   Demir, M. M.; Gulgun, M. A.; Menceloglu, Y. Z.; Abramchuk, S. S.; Makhaeva, E. E.; Khokhlov, A. R.; Matveeva, V. G.; Sulman, M. G. *Macromolecules* **2004**, *37*, 1787–1792.

(14)   Patel, A. C.; Li, S.; Wang, C.; Zhang, W.; Wei, Y. **2007**, *120*, 12289–12296.

(15)   Lu, X.; Wang, C.; Wei, Y. *Small* **2009**, *5*, 2349–2370.

(16)   International Agency for Research on Cancer. IARC Monographs- Classifications http://monographs.iarc.fr/ENG/Classification/ (accessed Jan 22, 2018).

(17)   International Agency for Research on Cancer. *IARC Monographs-Arsenic, Metals,*

Fibres and Dusts; 100; 100C; Lyon, 2012.

(18)   Atsdr. *U.S Public Heal. Serv. Agency Toxic Subst. Dis. Regist.* **2007**, 24.

(19)   USEPA. The Arsenic Rule: Background and Rule Provisions https://www.epa.gov/sites/production/files/2015-09/documents/train1-background.pdf (accessed Jan 11, 2018).

(20)   Robertson, F. N. *Environ. Geochem. Health* **1989**, *11*, 171–185.

(21)   Welch, A. H.; Westjohn, D. B.; Helsel, D. R.; Wanty, R. B. Arsenic in Ground Water of the United States: Occurrence and Geochemistry. *Ground Water*, 2000, *38*, 589–604.

(22)   Welch, A. H.; Lico, M. S.; Hughes, J. L. *Groundwater* **1988**, *26*, 333–347.

(23)   EPA. *Epa* **2000**, 1–156.

(24)   Sharma, V. K.; Sohn, M. Aquatic arsenic: Toxicity, speciation, transformations, and remediation. *Environment International*, 2009, *35*, 743–759.

(25)   Cole, R. H.; Frederick, R. E.; Healy, R. P.; Rolan, R. G. *J. (Water Pollut. Control Fed.* **1984**, *56*, 898–908.

(26)   World Health Organization (WHO). WHO | Arsenic http://www.who.int/mediacentre/factsheets/fs372/en/ (accessed Jan 12, 2018).

(27)   Ryker, S. J. *Geotimes* **2001**, *46*, 34–36.

(28)   Hristovski, K.; Baumgardner, A.; Westerhoff, P. *J. Hazard. Mater.* **2007**, *147*, 265–274.

(29)   Ungureanu, G.; Santos, S.; Boaventura, R.; Botelho, C. *J. Environ. Manage.* **2015**, *151*, 326–342.

(30)   Mohan, D.; Pittman, C. U. *J. Hazard. Mater.* **2007**, *142*, 1–53.

(31)   *Water Treatment: Principles and Design*; Crittenden, J. C.; Trusell, R. R.; Hand, D. W.; Howe, K. J.; Tachobanoglous, G., Eds.; 2nd ed.; John Wiley and Sons: Hoboken, New Jersey, 2005.

(32)   Freundlich, H. M. . *J. Phys. Chem* **1906**, *57*, 385–470.

(33)   Ayawei, N.; Ekubo, A. T.; Wankasi, D.; Dikio, E. D. *Orient. J. Chem.* **2015**, *31*, 1307–1318.

(34) Wolf, R. E. *U.S. Geol. Surv. Crustal Geophys. Geochemistry Sci. Cent.* **2005**, 7.

(35) Fabricius, A.-L.; Duester, L.; Meermann, B.; Ternes, T. a. *Anal. Bioanal. Chem.* **2014**, *406*, 467–479.

(36) Wilson, S. C.; Jones, K. C. *Environ. Pollut.* **1993**, *81*, 229–249.

(37) Mangas, E.; Vaquero, M. T.; Comellas, L.; Broto-Puig, F. *Chemosphere* **1998**, *36*, 61–72.

(38) USEPA. Quality Criteria for Water 1986 EPA440-5-86-001, 1986.

(39) Harrison, R. M.; Perry, R.; Wellings, R. A. *Water Res.* **1975**, *9*, 331–346.

(40) Organization, W. H. *Polynuclear aromatic hydrocarbons in Drinking-water Background document for development of WHO Guidelines for Drinking-water Quality*.

(41) BORNEFF, J.; KUNTE, H. *Arch. Hyg. Bakteriol.* **1964**, *148*, 585–597.

(42) Mackay, D.; Shiu, W. Y.; Ma, K. C. C. N.-O. R. T. D. 196 . O. M. *Volume II, Polynuclear Aromatic Hydrocarbons, Polychlorinated Dioxins, and Dibenzofurans*; 1992; Vol. II.

(43) Fornstedt, T.; Forssén, P.; Westerlund, D. *Anal. Sep. Sci. 5 Vol. Set, Vol. 2* **2015**, 1–22.

(44) *The theory of HPLC*; Elsevier, 1987; Vol. 17.

(45) Valderrama, C.; Gamisans, X.; de las Heras, X.; Farr??n, A.; Cortina, J. L. *J. Hazard. Mater.* **2008**, *157*, 386–396.

(46) Roduner, E. *Chem. Soc. Rev.* **2006**, *35*, 583–592.

(47) Yang and B. S. Xing., K. *Chem. Rev.* **2010**, *110*, 5989–6008.

(48) Adeleye, A. S.; Conway, J. R.; Garner, K.; Huang, Y.; Su, Y.; Keller, A. A. *Chem. Eng. J.* **2016**, *286*, 640–662.

(49) Pokropivny, V. V.; Skorokhod, V. V. *Mater. Sci. Eng. C* **2007**, *27*, 990–993.

(50) Qu, X.; Alvarez, P. J. J.; Li, Q. *Water Res.* **2013**, *47*, 3931–3946.

(51) Sontheimer, H.; Crittenden, J. C.; Summers, R. S. *Activated Carbon for Water Treatment*; 1988; Vol. 90.

(52)   Li, H.; Xu, C.; Srivastava, N.; Banerjee, K. *IEEE Trans. Electron Devices* **2009**, *56*, 1799–1821.

(53)   Mauter, M.; Elimelech, M. *Environ. Sci. Technol.* **2008**, *42*, 5843–5859.

(54)   McAllister, M. J.; Li, J. L.; Adamson, D. H.; Schniepp, H. C.; Abdala, A. A.; Liu, J.; Herrera-Alonso, M.; Milius, D. L.; Car, R.; Prud'homme, R. K.; Aksay, I. A. *Chem. Mater.* **2007**, *19*, 4396–4404.

(55)   Yang, S. T.; Chang, Y.; Wang, H.; Liu, G.; Chen, S.; Wang, Y.; Liu, Y.; Cao, A. *J. Colloid Interface Sci.* **2010**, *351*, 122–127.

(56)   Zhao, G.; Li, J.; Ren, X.; Chen, C.; Wang, X. *Environ. Sci. Technol.* **2011**, *45*, 10454–10462.

(57)   Liu, J.; Gao, Y.; Cao, D.; Zhang, L.; Guo, Z. *Langmuir* **2011**, *27*, 7926–7933.

(58)   Machida, M.; Mochimaru, T.; Tatsumoto, H. *Carbon N. Y.* **2006**, *44*, 2681–2688.

(59)   Upadhyay, R. K.; Soin, N.; Roy, S. S. *RSC Adv.* **2014**, *4*, 3823.

(60)   Liu, T.; Li, Y.; Du, Q.; Sun, J.; Jiao, Y.; Yang, G.; Wang, Z.; Xia, Y.; Zhang, W.; Wang, K.; Zhu, H.; Wu, D. *Colloids Surfaces B Biointerfaces* **2012**, *90*, 197–203.

(61)   Liu, F.; Chung, S.; Oh, G.; Seo, T. S. *ACS Appl. Mater. Interfaces* **2012**, *4*, 922–927.

(62)   Moradi, O.; Yari, M.; Moaveni, P.; Norouzi, M. *Fullerenes, Nanotub. Carbon Nanostructures* **2012**, *20*, 85–98.

(63)   Hristovski, K.; Westerhoff, P.; Crittenden, J. *J. Hazard. Mater.* **2008**, *156*, 604–611.

(64)   O'Carroll, D.; Sleep, B.; Krol, M.; Boparai, H.; Kocur, C. *Adv. Water Resour.* **2013**, *51*, 104–122.

(65)   Karn, B.; Kuiken, T.; Otto, M. *Environ. Health Perspect.* **2009**, *117*, 1823–1831.

(66)   Dankovich, T. A.; Gray, D. G. *Environ. Sci. Technol.* **2011**, *45*, 1992–1998.

(67)   Ren, D.; Colosi, L. M.; Smith, J. A. *Environ. Sci. Technol.* **2013**, *47*, 11206–11213.

(68)   Bennett, S. W.; Keller, A. A. *Appl. Catal. B Environ.* **2011**, *102*, 600–607.

(69)   Yang, J.; Li, D.; Wang, X.; Yang, X.; Lu, L. *J. Solid State Chem.* **2002**, *165*, 193–198.

(70)   Georgekutty, R.; Seery, M. K.; Pillai, S. C. *J. Phys. Chem. C* **2008**, *112*, 13563–

13570.

(71) Zodrow, K.; Brunet, L.; Mahendra, S.; Li, D.; Zhang, A.; Li, Q.; Alvarez, P. J. J. *Water Res.* **2009**, *43*, 715–723.

(72) Ehdaie, B.; Krause, C.; Smith, J. A. *Environ. Sci. Technol.* **2014**, *48*, 13901–13908.

(73) El-Kemary, M.; El-Shamy, H.; El-Mehasseb, I. *J. Lumin.* **2010**, *130*, 2327–2331.

(74) Alikhani, M.-Y.; Lee, S.-M.; Yang, J.-K.; Shirzad-Siboni, M.; Peeri-Dogaheh, H.; Khorasani, M.-S.; Nooshak, M.-A.; Samarghandi, M.-R. *Water Sci. Technol.* **2012**, *67*.

(75) Peiró, A. M.; Ayllón, J. A.; Peral, J.; Doménech, X. *Appl. Catal. B Environ.* **2001**, *30*, 359–373.

(76) Barakat, M. A.; Al-Hutailah, R. I.; Qayyum, E.; Rashid, J.; Kuhn, J. N. *Environ. Technol.* **2014**, *35*, 137–144.

(77) Kim, D. S.; Kwak, S.-Y. *Appl. Catal. A Gen.* **2007**, *323*, 110–118.

(78) Kominami, H.; Murakami, S.; Kato, J.; Kera, Y.; Ohtani, B. *J. Phys. Chem. B* **2002**, *106*, 10501–10507.

(79) Zhang, W. X. Nanoscale iron particles for environmental remediation: An overview. *Journal of Nanoparticle Research*, 2003, *5*, 323–332.

(80) Kaifas, D.; Malleret, L.; Kumar, N.; F??timi, W.; Claeys-Bruno, M.; Sergent, M.; Doumenq, P. *Sci. Total Environ.* **2014**, *481*, 335–342.

(81) Fan, J.; Guo, Y.; Wang, J.; Fan, M. *J. Hazard. Mater.* **2009**, *166*, 904–910.

(82) Shu, H. Y.; Chang, M. C.; Yu, H. H.; Chen, W. H. *J. Colloid Interface Sci.* **2007**, *314*, 89–97.

(83) Fang, Z.; Qiu, X.; Chen, J.; Qiu, X. *Appl. Catal. B Environ.* **2010**, *100*, 221–228.

(84) Shirazi, E.; Torabian, A.; Nabi-Bidhendi, G. *Clean - Soil, Air, Water* **2013**, *41*, 1062–1072.

(85) Ramos, M. A. V.; Yan, W.; Li, X.; Koel, B. E.; Zhang, W. *J. Phys. Chem. C* **2009**, *113*, 14591–14594.

(86) Hadipour-Goudarzi, E.; Montazer, M.; Latifi, M.; Aghaji, A. A. G. *Carbohydr. Polym.* **2014**, *113*, 231–239.

(87) Kumar, R.; Howdle, S.; Münstedt, H. *J. Biomed. Mater. Res. - Part B Appl. Biomater.* **2005**, *75*, 311–319.

(88) Chao, J. B.; Liu, J. F.; Yu, S. J.; Feng, Y. Di; Tan, Z. Q.; Liu, R.; Yin, Y. G. *Anal. Chem.* **2011**, *83*, 6875–6882.

(89) Liu, J.; Sonshine, D. a.; Shervani, S.; Hurt, R. H. *ACS Nano* **2010**, *4*, 6903–6913.

(90) Pena, M.; Meng, X.; Korfiatis, G. P.; Jing, C. *Environ. Sci. Technol.* **2006**, *40*, 1257–1262.

(91) Niu, H. Y.; Wang, J. M.; Shi, Y. L.; Cai, Y. Q.; Wei, F. S. *Microporous Mesoporous Mater.* **2009**, *122*, 28–35.

(92) Li, R.; Li, Q.; Gao, S.; Shang, J. K. *Chem. Eng. J.* **2012**, *185–186*, 127–135.

(93) Jing, C.; Meng, X.; Liu, S.; Baidas, S.; Patraju, R.; Christodoulatos, C.; Korfiatis, G. P. *J. Colloid Interface Sci.* **2005**, *290*, 14–21.

(94) Klaine, S. J.; Alvarez, P. J. J. J.; Batley, G. E.; Fernandes, T. F.; Handy, R. D.; Lyon, D. Y.; Mahendra, S.; McLaughlin, M. J.; Lead, J. R. *Environ. Toxicol. Chem.* **2008**, *27*, 1825–1851.

(95) Sanchez, V. C.; Jachak, A.; Hurt, R. H.; Kane, A. B. *Chem. Res. Toxicol.* **2012**, *25*, 15–34.

(96) Ratte, H. T. *Environ. Toxicol. Chem.* **1999**, *18*, 89–108.

(97) Zhang, Q. L.; Li, M. Q.; Ji, J. W.; Gao, F. P.; Bai, R.; Chen, C. Y.; Wang, Z. W.; Zhang, C.; Niu, Q. *Int. J. Immunopathol. Pharmacol.* **2011**, *24*.

(98) Izzati Fatimah Wahab, Saiful Izwan Abd Razak, Nor Syuhada Azmi, Farah Nuruljannah Dahli, A. H. M. Y. and N. H. M. N. *B. Adv. Carbon Nanostructures* **2016**.

(99) Deitzel, J. M.; Kleinmeyer, J.; Harris, D.; Tan, N. C. B. *Polymer (Guildf).* **2001**, *42*, 261–272.

(100) Trejo, N. K.; Frey, M. *J. Appl. Polym. Sci.* **2015**, *42657*, 1–10.

(101) Matsumoto, H.; Wakamatsu, Y.; Minagawa, M.; Tanioka, A. *J. Colloid Interface Sci.* **2006**, *293*, 143–150.

(102) Casper, C. L.; Stephens, J. S.; Tassi, N. G.; Chase, D. B.; Rabolt, J. F. *Macromolecules* **2004**, *37*, 573–578.

(103) Eda, G.; Liu, J.; Shivkumar, S. *Mater. Lett.* **2007**, *61*, 1451–1455.

(104) Eda, G.; Shivkumar, S. *J. Mater. Sci.* **2006**, *41*, 5704–5708.

(105) Lin, J.; Ding, B.; Yang, J.; Yu, J.; Sun, G. *Nanoscale* **2012**, *4*, 176–182.

(106) Fridrikh, S. V.; Yu, J. H.; Brenner, M. P.; Rutledge, G. C. *Phys. Rev. Lett.* **2003**, *90*, 144502.

(107) Kizildag, N.; Beceren, Y.; Kazanci, M.; Cukul, D. **2012**.

(108) Medeiros, E. S.; Mattoso, L. H. C.; Offeman, R. D.; Wood, D. F.; Orts, W. J. Effect of relative humidity on the morphology of electrospun polymer fibers. *Canadian Journal of Chemistry*, 2008, *86*, 590–599.

(109) Frenot, A.; Chronakis, I. S. *Curr. Opin. Colloid Interface Sci.* **2003**, *8*, 145–155.

(110) Huang, Z.-M.; Zhang, Y.-Z.; Kotaki, M.; Ramakrishna, S. *Compos. Sci. Technol.* **2003**, *63*, 2223–2253.

(111) Lin, J.; Shang, Y.; Ding, B.; Yang, J.; Yu, J.; Al-Deyab, S. S. *Mar. Pollut. Bull.* **2012**, *64*, 347–352.

(112) Pan, H.; Li, L.; Hu, L.; Cui, X. *Polymer (Guildf).* **2006**, *47*, 4901–4904.

(113) Rnjak-Kovacina, J.; Weiss, A. S. *Tissue Eng. B, Rev.* **2011**, *17*, 365–372.

(114) Lowery, J. L.; Datta, N.; Rutledge, G. C. *Biomaterials* **2010**, *31*, 491–504.

(115) Pham, Q. P.; Sharma, U.; Mikos, A. G. *Biomacromolecules* **2006**, *7*, 2796–2805.

(116) Soliman, S.; Pagliari, S.; Rinaldi, A.; Forte, G.; Fiaccavento, R.; Pagliari, F.; Franzese, O.; Minieri, M.; Di Nardo, P.; Licoccia, S.; Traversa, E. *Acta Biomater.* **2010**, *6*, 1227–1237.

(117) Powell, H. M.; Boyce, S. T. *J. Biomed. Mater. Res. Part A* **2008**, *84A*, 1078–1086.

(118) Powell, D. W.; Mifflin, R. C.; Valentich, J. D.; Crowe, S. E.; Saada, J. I.; West, a. B. *Am J Physiol Cell Physiol* **1999**, *277*, C1-19.

(119) Rnjak, J.; Li, Z.; Maitz, P. K. M.; Wise, S. G.; Weiss, A. S. *Biomaterials* **2009**, *30*, 6469–6477.

(120) Rnjak-Kovacina, J.; Wise, S. G.; Li, Z.; Maitz, P. K. M.; Young, C. J.; Wang, Y.; Weiss, A. S. *Biomaterials* **2011**, *32*, 6729–6736.

(121) Balguid, A.; Mol, A.; van Marion, M. H.; Bank, R. A.; Bouten, C. V. C.; Baaijens, F. P. T. *Tissue Eng. Part A* **2008**, *15*, 437–444.

(122) Eichhorn, S. J.; Sampson, W. W. *J. R. Soc. Interface* **2005**, *2*, 309–318.

(123) Yang, Y.; Zhu, X.; Cui, W.; Li, X.; Jin, Y. *Macromol. Mater. Eng.* **2009**, *294*, 611–619.

(124) Blakeney, B. A.; Tambralli, A.; Anderson, J. M.; Andukuri, A.; Lim, D.-J.; Dean, D. R.; Jun, H.-W. *Biomaterials* **2011**, *32*, 1583–1590.

(125) Park, G. S.; Lee, J. S.; Kim, S. T.; Park, S.; Cho, J. *J. Power Sources* **2013**, *243*, 267–273.

(126) Rajala, J.; Shin, H.; Lolla, D.; Chase, G. *Fibers* **2015**, *3*, 450–462.

(127) Baker, B. M.; Gee, A. O.; Metter, R. B.; Nathan, A. S.; Marklein, R. A.; Burdick, J. A.; Mauck, R. L. *Biomaterials* **2008**, *29*, 2348–2358.

(128) Zhang, Y.; Ouyang, H.; Lim, C. T.; Ramakrishna, S.; Huang, Z.-M. *J. Biomed. Mater. Res.* **2005**, *72B*, 156–165.

(129) Ji, C.; Annabi, N.; Khademhosseini, A.; Dehghani, F. *Acta Biomater.* **2011**, *7*, 1653–1664.

(130) Nam, J.; Huang, Y.; Agarwal, S.; Lannutti, J. *Tissue Eng.* **2007**, *13*, 2249–2257.

(131) Kim, G. H.; Kim, W. D. *J. Biomed. Mater. Res. - Part B Appl. Biomater.* **2007**, *81*, 104–110.

(132) Leong, M. F.; Chan, W. Y.; Chian, K. S.; Rasheed, M. Z.; Anderson, J. M. *J. Biomed. Mater. Res. - Part A* **2010**, *94*, 1141–1149.

(133) Simonet, M.; Stingelin, N.; Wismans, J. G. F.; Oomens, C. W. J.; Driessen-Mol, A.; Baaijens, F. P. T. *J. Mater. Chem. B* **2014**, *2*, 305–313.

(134) Megelski, S.; Stephens, J. S.; Bruce Chase, D.; Rabolt, J. F. *Macromolecules* **2002**, *35*, 8456–8466.

(135) Pratyush Dayal, †; Jing Liu, ‡; Satish Kumar, ‡; and Thein Kyu*, †. *Macromolecules* **2007**, *40*, 7689–7694.

(136) Bognitzki, M.; Czado, W.; Frese, T.; Schaper, A.; Hellwig, M.; Steinhart, M.; Greiner, A.; Wendorff, J. H. *Adv. Mater.* **2001**, *13*, 70–72.

(137) Berghmans, H.; Cooman, R. De. *Polymer (Guildf).* **1998**, *39*, 4621–4629.

(138) Bogntizki, M.; Frese, T.; Steinhart, M.; Greiner, A.; Wendorff, J. H.; Schaper, A.; Hellwig, M. *Polym. Eng. Sci.* **2001**, *41*, 982–989.

(139) Kalra, V.; Lee, J.; Lee, J. H.; Lee, S. G.; Marquez, M.; Wiesner, U.; Joo, Y. L. *Small* **2008**, *4*, 2067–2073.

(140) Park, H. S.; Choi, B. G.; Hong, W. H.; Jang, S. Y. *J. Colloid Interface Sci.* **2013**, *406*, 24–29.

(141) Bognitzki, M.; Frese, T.; Steinhart, M.; Greiner, A.; Wendorff, J. H.; Schaper, A.; Hellwig, M. *Polym. Eng. Sci.* **2001**, *41*, 982–989.

(142) Zhang, L.; Hsieh, Y. Lo. *Nanotechnology* **2006**, *17*, 4416–4423.

(143) Moon, S.; Choi, J.; Farris, R. J. *Fibers Polym.* **2008**, *9*, 276–280.

(144) You, Y.; Youk, J. H.; Lee, S. W.; Min, B. M.; Lee, S. J.; Park, W. H. *Mater. Lett.* **2006**, *60*, 757–760.

(145) Sarazin, P.; Roy, X.; Favis, B. D. *Biomaterials* **2004**, *25*, 5965–5978.

(146) Fejos, M.; Molnár, K.; Karger-Kocsis, J. *Materials (Basel).* **2013**, *6*, 4489–4504.

(147) Tran, C.; Kalra, V. *Soft Matter* **2013**, *9*, 846–852.

(148) Sing, K. S. W. *Pure Appl. Chem.* **1985**, *57*.

(149) Zhan, S.; Chen, D.; Jiao, X.; Tao, C. **2006**, 11199–11204.

(150) Covarrubias, C.; García, R.; Arriagada, R.; Yánez, J.; Ramanan, H.; Lai, Z.; Tsapatsis, M. *J. Memb. Sci.* **2008**, *312*, 163–173.

(151) Pokhrel, L. R.; Dubey, B.; Scheuerman, P. R. *Environ. Sci. Technol.* **2013**, *47*, 12877–12885.

(152) O'Hern, S. C.; Boutilier, M. S. H.; Idrobo, J.-C.; Song, Y.; Kong, J.; Laoui, T.; Atieh, M.; Karnik, R. *Nano Lett.* **2014**, *14*, 1234–1241.

(153) Gonzalez, M. J.; Miranda-Massari, J. R.; Berdiel, M. J.; Duconge, J.; Rodríguez-López, J. L.; Hunninghake, R.; Cobas-Rosario, V. J. *J. Orthomol. Med.* **2014**, *29*, 154–156.

(154) Doktor, T.; Kytýř, D.; Valach, J.; Jiroušek, O. 978–988.

(155) Micromeritics Instrument Corporation. Mercury Intrusion Porosimetry Theory http://www.micromeritics.com/Repository/Files/Mercury_Porosemitry_Theory_post

er_.pdf (accessed Jan 10, 2018).

(156) Xu, X.; Yang, L.; Xu, X.; Wang, X.; Chen, X.; Liang, Q.; Zeng, J.; Jing, X. *J. Control. Release* **2005**, *108*, 33–42.

(157) Nitanan, T.; Akkaramongkolporn, P.; Ngawhirunpat, T.; Rojanarata, T.; Panomsuk, S.; Opanasopit, P. *Int. J. Pharm.* **2013**, *450*, 345–353.

(158) Li, M.; Han, G.; Yang, B. *Fabrication of the catalytic electrodes for methanol oxidation on electrospinning-derived carbon fibrous mats*; 2008; Vol. 10.

(159) Bhardwaj, N.; Kundu, S. C. *Biotechnol. Adv.* **2010**, *28*, 325–347.

(160) Thavasi, V.; Singh, G.; Ramakrishna, S. *Energy Environ. Sci.* **2008**, *1*, 205.

(161) Kaur, S.; Ma, Z.; Gopal, R.; Singh, G.; Ramakrishna, S.; Matsuura, T. *Langmuir* **2007**, *23*, 13085–13092.

(162) Saeed, K.; Haider, S.; Oh, T. J.; Park, S. Y. *J. Memb. Sci.* **2008**, *322*, 400–405.

(163) Li, L.; Li, Y.; Cao, L.; Yang, C. *Carbohydr. Polym.* **2015**, *125*, 206–213.

(164) Lee, M. W.; An, S.; Latthe, S. S.; Lee, C.; Hong, S.; Yoon, S. S. *ACS Appl. Mater. Interfaces* **2013**, *5*, 10597–10604.

(165) Wu, J.; Wang, N.; Wang, L.; Dong, H.; Zhao, Y.; Jiang, L. *ACS Appl. Mater. Interfaces* **2012**, *4*, 3207–3212.

(166) Tran, D.; Marti, A.; Balkus, K. *Fibers* **2014**, *2*, 308–317.

(167) Daels, N.; De Vrieze, S.; Sampers, I.; Decostere, B.; Westbroek, P.; Dumoulin, a.; Dejans, P.; De Clerck, K.; Van Hulle, S. W. H. *Desalination* **2011**, *275*, 285–290.

(168) Xu, X.; Yang, Q.; Wang, Y.; Yu, H.; Chen, X.; Jing, X. *Eur. Polym. J.* **2006**, *42*, 2081–2087.

(169) Kim, H. G.; Kim, J. H. *Fibers Polym.* **2011**, *12*, 602–609.

(170) Ignatova, M.; Manolova, N.; Rashkov, I. *Eur. Polym. J.* **2007**, *43*, 1112–1122.

(171) Pant, B.; Pant, H. R.; Pandeya, D. R.; Panthi, G.; Nam, K. T.; Hong, S. T.; Kim, C. S.; Kim, H. Y. *Colloids Surfaces A Physicochem. Eng. Asp.* **2012**, *395*, 94–99.

(172) Mangal, R.; Srivastava, S.; Archer, L. a. *Nat. Commun.* **2015**, *6*, 1–9.

(173) Li, C. J.; Zhang, S. S.; Wang, J. N.; Liu, T. Y. *Catal. Today* **2014**, *224*, 94–103.

(174) Khalil, A.; Kim, J. J.; Tuller, H. L.; Rutledge, G. C.; Hashaikeh, R. *Sensors Actuators, B Chem.* **2016**, *227*, 54–64.

(175) Dong, H.; Fey, E.; Gandelman, A.; Jones, W. E. *Chem. Mater.* **2011**, 2008–2011.

(176) Li, D.; Xia, Y. *Adv. Mater.* **2004**, *16*, 1151–1170.

(177) Ramakrishna, S.; Fujihara, K.; Teo, W.-E.; Lim, T.-C. *J. Eng. Fiber. Fabr.* **2008**, *3*, 46–47.

(178) Li, Y.; Gong, J.; He, G.; Deng, Y. *Mater. Chem. Phys.* **2011**, *129*, 477–482.

(179) Su, C.; Ran, X.; Hu, J.; Shao, C. *Environ. Sci. Technol.* **2013**, *47*, 11562–11568.

(180) Ramaseshan, R.; Sundarrajan, S.; Jose, R.; Ramakrishna, S. *J. Appl. Phys.* **2007**, *102*, 111101.

(181) Li, D.; Xia, Y. *Nano Lett.* **2003**, *3*, 555–560.

(182) Ding, B.; Kim, C. K.; Kim, H. Y.; Seo, M. K.; Park, S. J. Titanium dioxide nanofibers prepared by using electrospinning method. *Fibers and Polymers*, 2004, *5*, 105–109.

(183) Madani, M.; Sharifi-Sanjani, N.; Hasan-Kaviar, A.; Choghazardi, M.; Faridi-Majidi, R.; Hamouda, A. S. *Polym. Eng. Sci.* **2013**, *53*, 2407–2412.

(184) Caruso, R. a.; Susha, A.; Caruso, F. *Chem. Mater.* **2001**, *13*, 400–409.

(185) Matijević, E.; Scheiner, P. *J. Colloid Interface Sci.* **1978**, *63*, 509–524.

(186) Schindelin, J.; Arganda-Carreras, I.; Frise, E.; Kaynig, V.; Longair, M.; Pietzsch, T.; Preibisch, S.; Rueden, C.; Saalfeld, S.; Schmid, B.; Tinevez, J.-Y. J.-Y.; White, D. J.; Hartenstein, V.; Eliceiri, K.; Tomancak, P.; Cardona, A.; Liceiri, K.; Tomancak, P.; A., C. *Nat. Methods* **2012**, *9*, 676–682.

(187) Fong, H.; Chun, I.; Reneker, D. H. *Polymer (Guildf).* **1999**, *40*, 4585–4592.

(188) Leach, M. K.; Feng, Z.-Q.; Tuck, S. J.; Corey, J. M. *J. Vis. Exp.* **2011**, 2–6.

(189) Yang, Q.; Li, Z.; Hong, Y.; Zhao, Y.; Qiu, S.; Wang, C.; Wei, Y. *J. Polym. Sci. Part B Polym. Phys.* **2004**, *42*, 3721–3726.

(190) Mackay, M. E.; Dao, T. T.; Tuteja, A.; Ho, D. L.; van Horn, B.; Kim, H.-C.; Hawker, C. J. *Nat. Mater.* **2003**, *2*, 762–766.

(191) Doshi, J.; Reneker, D. H. *Conf. Rec. 1993 IEEE Ind. Appl. Conf. Twenty-Eighth IAS*

Annu. Meet. **1993**, *35*, 151–160.

(192) Batchelor, G. K. The stress system in a suspension of force-free particles. *Journal of Fluid Mechanics*, 1970, *41*, 545.

(193) Einstein, A. On the movement of small particles suspended in stationary liquids required by the molecular-kinetic theory of heat. *Annalen der Physik*, 1905, *322*, 549–560.

(194) Tuteja, A.; Duxbury, P. M.; Mackay, M. E. *Macromolecules* **2007**, *40*, 9427–9434.

(195) Ojha, S. S.; Afshari, M.; Kotek, R.; Gorga, R. E. *J. Appl. Polym. Sci.* **2008**, *108*, 308–319.

(196) Pai, C.-L.; Boyce, M. C.; Rutledge, G. C. *Macromolecules* **2009**, *42*, 2102–2114.

(197) Balgis, R.; Kartikowati, C. W.; Ogi, T.; Gradon, L.; Bao, L.; Seki, K.; Okuyama, K. *Chem. Eng. Sci.* **2015**.

(198) Lee, K. H.; Kim, H. Y.; Bang, H. J.; Jung, Y. H.; Lee, S. G. *Polymer (Guildf).* **2003**, *44*, 4029–4034.

(199) Mazinani, S.; Ajji, A.; Dubois, C. *Polymer (Guildf).* **2009**, *50*, 3329–3342.

(200) Jordan, J.; Jacob, K. I.; Tannenbaum, R.; Sharaf, M. a.; Jasiuk, I. *Mater. Sci. Eng. A* **2005**, *393*, 1–11.

(201) Khare, H. S.; Burris, D. L. *Polymer (Guildf).* **2010**, *51*, 719–729.

(202) Dutta, P. K.; Ray, A. K.; Sharma, V. K.; Millero, F. J. *J. Colloid Interface Sci.* **2004**, *278*, 270–275.

(203) Jiang, Y.; Wang, W. N.; Biswas, P.; Fortner, J. D. *ACS Appl. Mater. Interfaces* **2014**, *6*, 11766–11774.

(204) Jiang, Y.; Wang, W. N.; Liu, D.; Nie, Y.; Li, W.; Wu, J.; Zhang, F.; Biswas, P.; Fortner, J. D. *Environ. Sci. Technol.* **2015**, *49*, 6846–6854.

(205) Yoon, K.; Hsiao, B. S.; Chu, B. *J. Mater. Chem.* **2008**, *18*, 5326.

(206) Ellis, G. Grand challenges for engineering. *IEEE Engineering Management Review*, 2009, *37*, 3.

(207) Matsui, Y.; Nakano, Y.; Hiroshi, H.; Ando, N.; Matsushita, T.; Ohno, K. *Water Sci. Technol.* **2010**, *62*, 2664–2668.

(208) Partlan, E.; Davis, K.; Ren, Y.; Apul, O. G.; Mefford, O. T.; Karanfil, T.; Ladner, D. A. *Water Res.* **2016**, *89*, 161–170.

(209) Ellerie, J. R.; Apul, O. G.; Karanfil, T.; Ladner, D. A. *J. Hazard. Mater.* **2013**, *261*, 91–98.

(210) de Faria, A. F.; Perreault, F.; Shaulsky, E.; Hoover Arias Chavez, L.; Elimelech, M. *ACS Appl. Mater. Interfaces* **2015**, 150517163606006.

(211) Mohammadzadehmoghadam, S.; Dong, Y.; Jeffery Davies, I. *J. Polym. Sci. Part B Polym. Phys.* **2015**, *53*, 1171–1212.

(212) Bayley, G. M.; Mallon, P. E. *Polymer (Guildf).* **2012**, *53*, 5523–5539.

(213) Jadhav, A. H.; Mai, X. T.; Ofori, F. A.; Kim, H. *Chem. Eng. J.* **2015**, *259*, 348–356.

(214) Sen, R.; Zhao, B.; Perea, D.; Itkis, M. E.; Hu, H.; Love, J.; Bekyarova, E.; Haddon, R. C. *Nano Lett.* **2004**, *4*, 459–464.

(215) Das, S.; Wajid, A. S.; Bhattacharia, S. K.; Wilting, M. D.; Rivero, I. V.; Green, M. J. *J. Appl. Polym. Sci.* **2013**, *128*, 4040–4046.

(216) Barzegar, F.; Bello, A.; Fabiane, M.; Khamlich, S.; Momodu, D.; Taghizadeh, F.; Dangbegnon, J.; Manyala, N. *J. Phys. Chem. Solids* **2015**, *77*, 139–145.

(217) Doudrick, K.; Herckes, P.; Westerhoff, P. *Environ. Sci. Technol.* **2012**, *46*, 12246–12253.

(218) Karanfil, T.; Kilduff, J. E. *Environ. Sci. Technol.* **1999**, *33*, 3217–3224.

(219) Bonvin, F.; Jost, L.; Randin, L.; Bonvin, E.; Kohn, T. *Water Res.* **2016**, *90*, 90–99.

(220) Apul, O. G.; Hoogesteijn von Reitzenstein, N.; Schoepf, J.; Ladner, D.; Hristovski, K. D.; Westerhoff, P. *Sci. Total Environ.* **2017**, *592*, 458–464.

(221) Long, R. Q.; Yang, R. T. Carbon nanotubes as superior sorbent for dioxin removal [1]. *Journal of the American Chemical Society*, 2001, *123*, 2058–2059.

(222) Kim, C.; Choi, Y. S.; Lee, S. M.; Park, J. T.; Kim, B.; Lee, Y. H. *J Am Chem Soc* **2002**, *124*, 9906–9911.

(223) Peng, X.; Li, Y.; Luan, Z.; Di, Z.; Wang, H.; Tian, B.; Jia, Z. *Chem. Phys. Lett.* **2003**, *376*, 154–158.

(224) Wang, X.; Chen, C.; Hu, W.; Ding, A.; Xu, D.; Zhou, X. *Environ. Sci. Technol.* **2005**, *39*, 2856–2860.

(225) Liu, Z.; Gao, Y.; Bando, Y. *Appl. Phys. Lett.* **2003**, *81*, 4844–4846.

(226) Hilding, J.; Grulke, E. A.; Sinnott, S. B.; Qian, D.; Andrews, R.; Jagtoyen, M. *Langmuir* **2001**, *17*, 7540–7544.

(227) Li, Y. H.; Wang, S. G.; Wei, J. Q.; Zhang, X. F.; Xu, C. L.; Luan, Z. K.; Wu, D. H.; Wei, B. Q. *Chem. Phys. Lett.* **2002**, *357*, 263–266.

(228) Li, Y. H.; Wang, S.; Cao, A.; Zhao, D.; Zhang, X.; Xu, C.; Luan, Z.; Ruan, D.; Liang, J.; Wu, D.; Wei, B. *Chem. Phys. Lett.* **2001**, *350*, 412–416.

(229) Lu, C.; Chung, Y. L.; Chang, K. F. *Water Res.* **2005**, *39*, 1183–1189.

(230) Keblinski, P.; Nayak, S. K.; Zapol, P.; Ajayan, P. M. *Phys. Rev. Lett.* **2002**, *89*, 255503.

(231) Furmaniak, S.; Terzyk, A. P.; Gauden, P. A.; Rychlicki, G. *J. Colloid Interface Sci.* **2006**, *295*, 310–317.

(232) Werder, T.; Walther, J. H.; Jaffe, R. L.; Halicioglu, T.; Koumoutsakos, P.; Field, M.; Corporation, E.; V, W. F. a; Sunny, V. *J. Phys. Chem. B* **2003**, *107*, 1345–1352.

(233) Zare, K.; Gupta, V. K.; Moradi, O.; Makhlouf, A. S. H.; Sillanpää, M.; Nadagouda, M. N.; Sadegh, H.; Shahryari-ghoshekandi, R.; Pal, A.; Wang, Z.; Tyagi, I.; Kazemi, M. *J. Nanostructure Chem.* **2015**, *5*, 227–236.

(234) Ren, X.; Chen, C.; Nagatsu, M.; Wang, X. *Chem. Eng. J.* **2011**, *170*, 395–410.

(235) Ahmadpour, A.; Do, D. D. *Carbon N. Y.* **1996**, *34*, 471–479.

(236) Hackley, V. A.; Wiesner, M. R. *CEINT, Natl. Inst. Standars Technol.* **2010**, 1–10.

(237) Jian, M.; Wang, H.; Liu, R.; Qu, J.; Wang, H.; Zhang, X. *Environ. Sci. Nano* **2016**.

(238) Wang, Y.; Tang, J.; Xie, S.; Liu, J.; Xin, Z.; Liu, X.; Belfiore, L. A. *RSC Adv.* **2015**, 42174–42177.

(239) Kedem, S.; Schmidt, J.; Paz, Y.; Cohen, Y. *Langmuir* **2005**, *21*, 5600–5604.

(240) Chronakis, I. S. *J. Mater. Process. Technol.* **2005**, *167*, 283–293.

(241) Apul, O. G.; Wang, Q.; Zhou, Y.; Karanfil, T. *Water Res.* **2013**, *47*, 1648–1654.

(242) Kronberg, B.; Costas, M.; Silveston, R. *Pure Appl. Chem.* **1995**, *67*, 897–902.

(243) Trivedi, P.; Axe, L. *Environ. Sci. Technol.* **2000**, *34*, 2215–2223.

(244) Koeppenkastrop, D.; De Carlo, E. H. *Environ. Sci. Technol.* **1993**, *27*, 1796–1802.

(245) Yean, S.; Cong, L.; Yavuz, C. T.; Mayo, J. T.; Yu, W. W.; Kan, A. T.; Colvin, V. L.; Tomson, M. B. *J. Mater. Res.* **2005**, *20*, 3255–3264.

(246) Mayo, J. T.; Yavuz, C.; Yean, S.; Cong, L.; Shipley, H.; Yu, W.; Falkner, J.; Kan, A.; Tomson, M.; Colvin, V. L. *Sci. Technol. Adv. Mater.* **2007**, *8*, 71–75.

(247) Bang, S.; Patel, M.; Lippincott, L.; Meng, X. *Chemosphere* **2005**, *60*, 389–397.

(248) Peter, K. T.; Vargo, J. D.; Rupasinghe, T. P.; De Jesus, A.; Tivanski, A. V.; Sander, E. A.; Myung, N. V.; Cwiertny, D. M. *ACS Appl. Mater. Interfaces* **2016**, *8*, 11431–11440.

(249) Crespy, D.; Friedemann, K.; Popa, A. M. *Macromol. Rapid Commun.* **2012**, *33*, 1978–1995.

(250) Peter, K. T.; Johns, A. J.; Myung, N. V.; Cwiertny, D. M. *Water Res.* **2017**, *117*, 207–217.

(251) Senthamizhan, A.; Balusamy, B.; Celebioglu, A.; Uyar, T. *J. Mater. Chem. A* **2016**, *4*, 2484–2493.

(252) Beheshti, H.; Irani, M.; Hosseini, L.; Rahimi, A.; Aliabadi, M. *Chem. Eng. J.* **2016**, *284*, 557–564.

(253) Hand, D. W.; Crittenden, J. C.; Thacker, W. E. *J. Environ. Eng.* **1983**, *109*, 82–101.

(254) Mertz, K. (Michigan T. U.; Gobin, F.; Hand, D.; Hokanson, D.; Crittenden, C. AdDesignS, 1994.

(255) Worch, E. *Adsorption technology in water treatment: Fundamentals, processes, and modeling*; 2012.

(256) Smith, A. H.; Lingas, E. O.; Rahman, M. *Bull. World Health Organ.* **2000**, *78*, 1093–1103.

(257) Polizzotto, M. L.; Kocar, B. D.; Benner, S. G.; Sampson, M.; Fendorf, S. *Nature* **2008**, *454*, 505–508.

(258) Colman, J. A.; MARCIVE - York University.; Massachusetts. Dept. of Environmental Protection.; Massachusetts. Dept. of Public Health.; Geological Survey (U.S.). Arsenic and uranium in water from private wells completed in bedrock of east-central Massachusetts--concentrations, correlations with bedrock units, and estimated probability maps. *Scientific investigations report 2011-5013*,

2011, 1 online resource (vi, 113 p.).

(259) Roh, T.; Lynch, C. F.; Weyer, P.; Wang, K.; Kelly, K. M.; Ludewig, G. *Environ. Res.* **2017**, *159*, 338–343.

(260) Westerhoff, P.; Song, G.; Hristovski, K.; Kiser, M. a. *J. Environ. Monit.* **2011**, *13*, 1195–1203.

(261) Peill, N. J.; Hoffmann, M. R. *Environ. Sci. Technol.* **1995**, *29*, 2974–2981.

(262) Gao, B.; Lim, T. M.; Subagio, D. P.; Lim, T. T. *Appl. Catal. A Gen.* **2010**, *375*, 107–115.

(263) Keller, A. a.; McFerran, S.; Lazareva, A.; Suh, S. *J. Nanoparticle Res.* **2013**, *15*.

(264) Williams, G.; Seger, B.; Kamat, P. V. *ACS Nano* **2008**, *2*, 1487–1491.

(265) Kim, K.-H.; Kabir, E.; Jahan, S. A. *Sci. Total Environ.* **2017**, *575*, 525–535.

(266) Loos, R.; Locoro, G.; Comero, S.; Contini, S.; Schwesig, D.; Werres, F.; Balsaa, P.; Gans, O.; Weiss, S.; Blaha, L.; Bolchi, M.; Gawlik, B. M. *Water Res.* **2010**, *44*, 4115–4126.

(267) Li, H.; Cao, Y.; Zhang, D.; Pan, B. *Sci. Total Environ.* **2018**, *618*, 269–275.

(268) Landers, J.; Gor, G. Y.; Neimark, A. V. *Colloids Surfaces A Physicochem. Eng. Asp.* **2013**, *437*, 3–32.

(269) Qin, D.; Lu, W.; Zhu, Z.; Li, N.; Xu, T.; Wang, G.; Chen, W. *Ind. Eng. Chem. Res.* **2017**, *56*, 11151–11160.

(270) Joseph, K.; Raj, A.; Viswanathan, B. *Indian J. Chem.* **2009**, *48*, 1378–1382.

(271) Lin, T. F.; Wu, J. K. *Water Res.* **2001**, *35*, 2049–2057.

(272) Siegel, R. W.; Ramasamy, S.; Hahn, H.; Zongquan, L.; Ting, L.; Gronsky, R.; Introduction, I. *J. Mater. Res.* **1988**, *3*, 1367–1372.

(273) Jang, I. B.; Sung, J. H.; Choi, H. J.; Chin, I. *J. Mater. Sci.* **2005**, *40*, 3021–3024.

(274) Loría-Bastarrachea, M. I.; Herrera-Kao, @bullet W; Cauich-Rodríguez, J. V; Cervantes-Uc, J. M.; Vázquez-Torres, @bullet H; Vila-Ortega, @bullet A. .

(275) Hoogesteijn Von Reitzenstein, N.; Bi, X.; Yang, Y.; Hristovski, K.; Westerhoff, P. *J. Appl. Polym. Sci.* **2016**, *133*.

(276) Draper, N. R. *Commun. Stat. - Theory Methods* **1998**, *27*, 2581–2623.

(277) Badruzzaman, M.; Westerhoff, P.; Knappe, D. R. U. *Water Res.* **2004**, *38*, 4002–4012.

(278) Hristovski, K. D.; Markovski, J. *Sci. Total Environ.* **2017**, *598*, 258–271.

(279) Hristovski, K. D.; Westerhoff, P. K.; Crittenden, J. C.; Olson, L. W. *Environ. Sci. Technol.* **2008**, *42*, 3786–3790.

(280) W.I. Weber, H. Sontheimer, J.C. Crittenden, S. S. *Activated Carbon for Water Treatment*; 2nd ed.; DVGW-Forschungsstelle: Karlsruhe, Germany, 1988.

(281) Agency, U. S. E. P. Test Methods for Evaluating Solid Waste (Physical/Chemical Methods SW-846), 1996.

(282) Apul, O. G.; Hoogesteijn von Reitzenstein, N.; Schoepf, J.; Ladner, D.; Hristovski, K. D.; Westerhoff, P. *Sci. Total Environ.* **2017**, *592*.

APPENDIX A

THE FOLLOWING CONTAINS SUPPLEMENTAL INFORMATION FOR

CHAPTER 4: MORPHOLOGY, STRUCTURE, AND PROPERTIES OF METAL

OXIDE/POLYMER NANOCOMPOSITE ELECTROSPUN MATS.
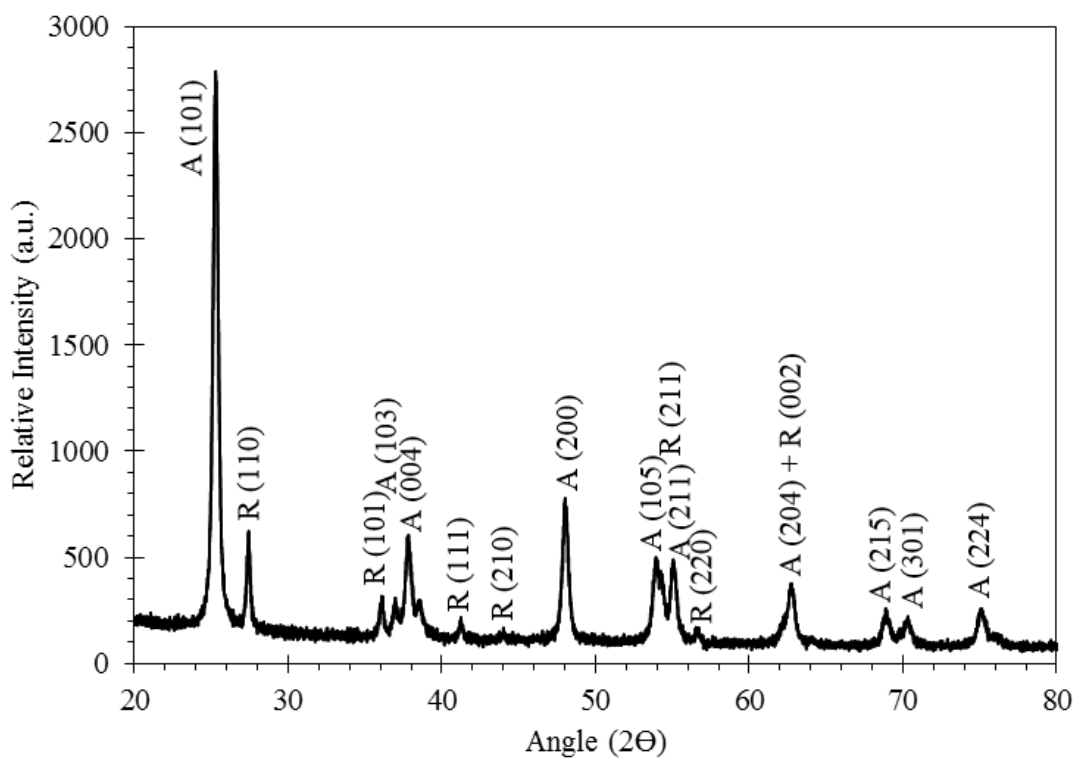
Figure A-1. XRD Spectra of TiO₂. "A" indicates an anatase phase peak, "R" indicates a rutile phase peak.
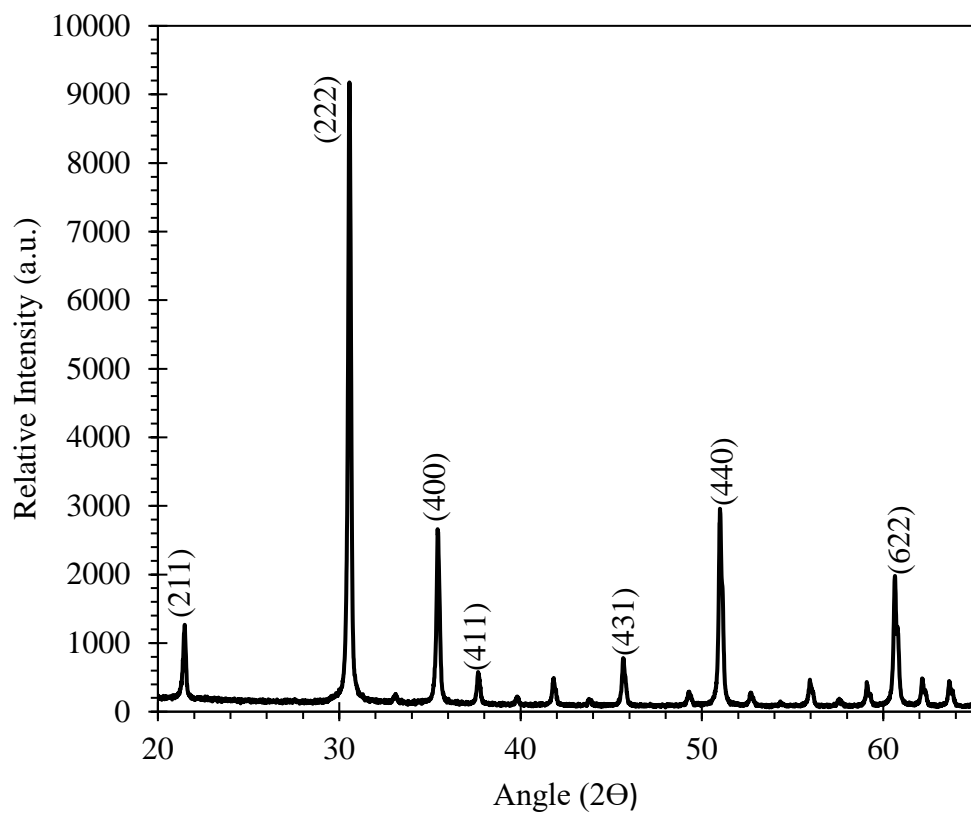
Figure A-2. XRD Spectra of In$_2$O$_3$.
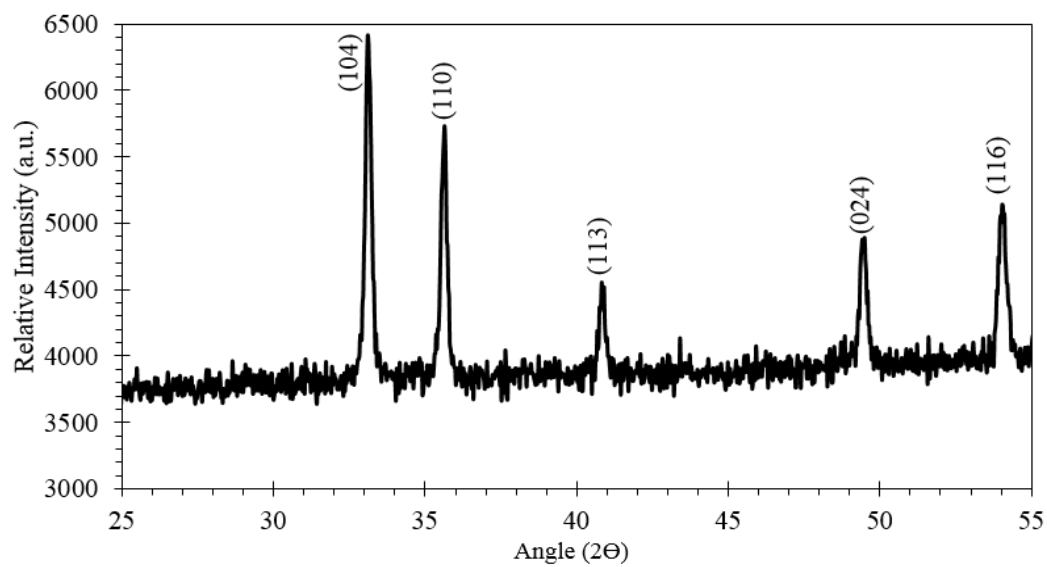
Figure A-3. XRD Spectra of Fe₂O₃. Background noise is due to fluorescence.
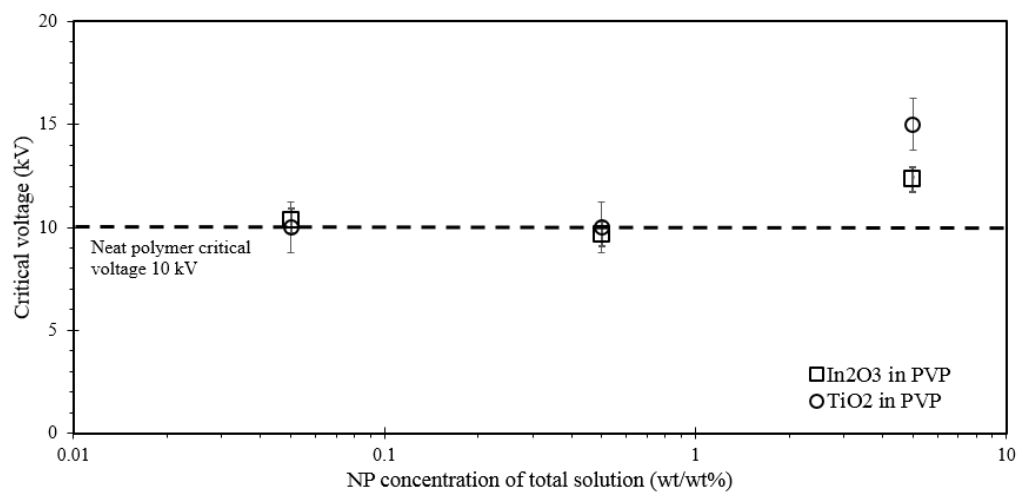
Figure A-4. Critical Voltage to Reach Unstable and Stable Taylor Cone in PVP solutions. Error bars indicate one standard deviation from triplicate experiments using the same NP-polymer solution. Critical voltage applied did not change significantly until 5 % (m/v) NP loading. This may be a product of the viscosity increase at 5 % (m/v) NP loading (see Figure 3.3).

APPENDIX B

THE FOLLOWING CONTAINS SUPPLEMENTAL INFORMATION FOR

CHAPTER 5:"SUPERFINE POWDERED ACTIVATED CARBON INCORPORATED

INTO ELECTROSPUN POLYSTYRENE FIBERS PRESERVE ADSORPTION

CAPACITY.
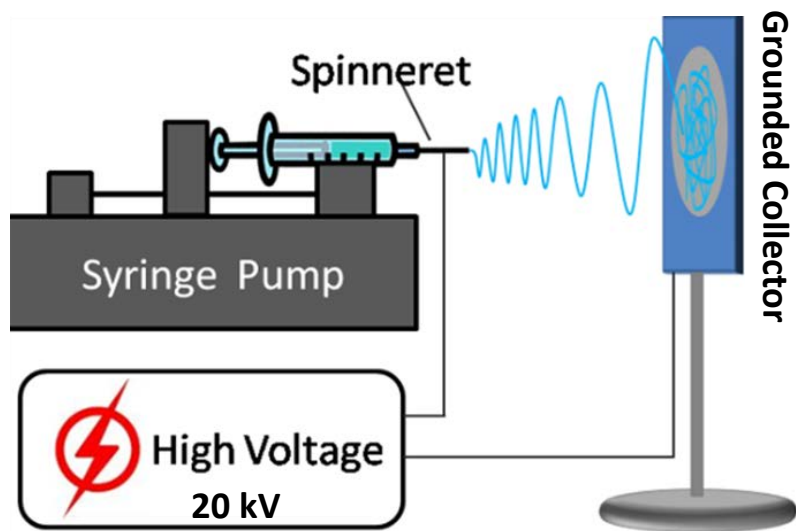
Figure B-1. Schematic Diagram of Electrospinning Apparatus (adopted from Huang and You, 2013).
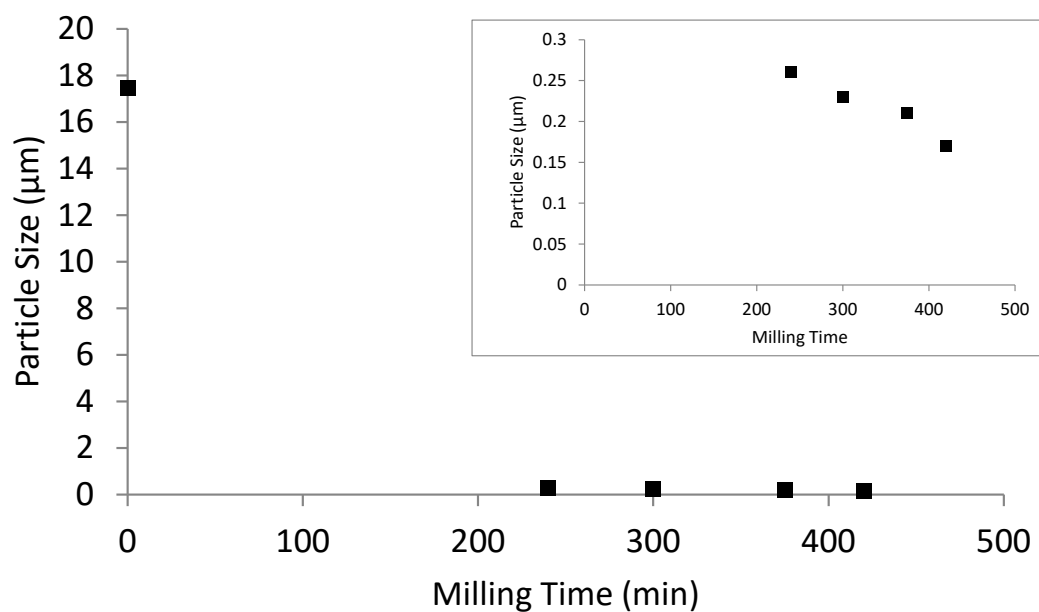
Figure B-2. The Change of Particle Size with Milling Time. The insert zooms in to the last 4 data points.
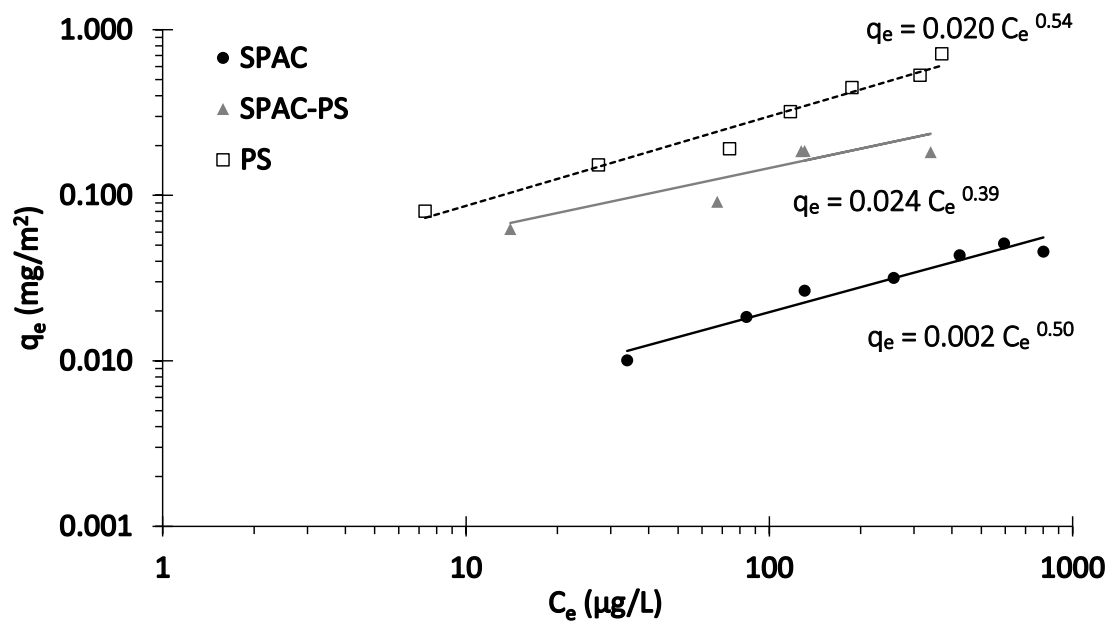
Figure B-3. Liquid Phase Adsorption Isotherms of phenanthrene on SPAC alone, SPAC-PS composite and neat PS on dry mass basis per unit specific surface area.
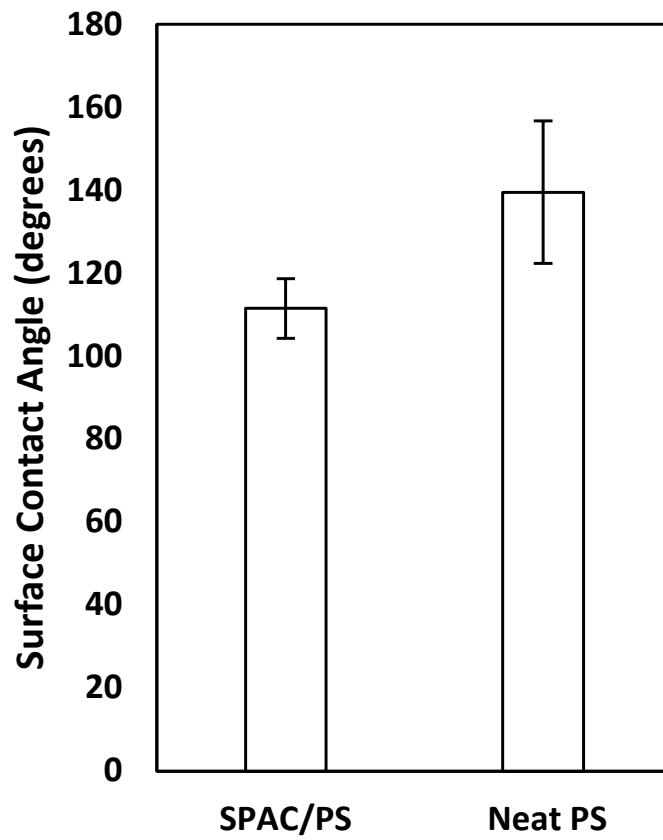
Figure B-4. Comparison of Surface Contact Angles for Neat PS and SPAC-PS composite *p*-value according to Student's t-test for one-tailed hypothesis testing is 0.056.
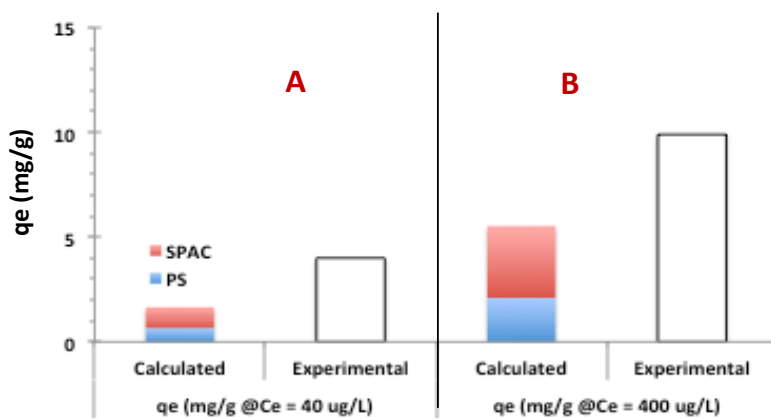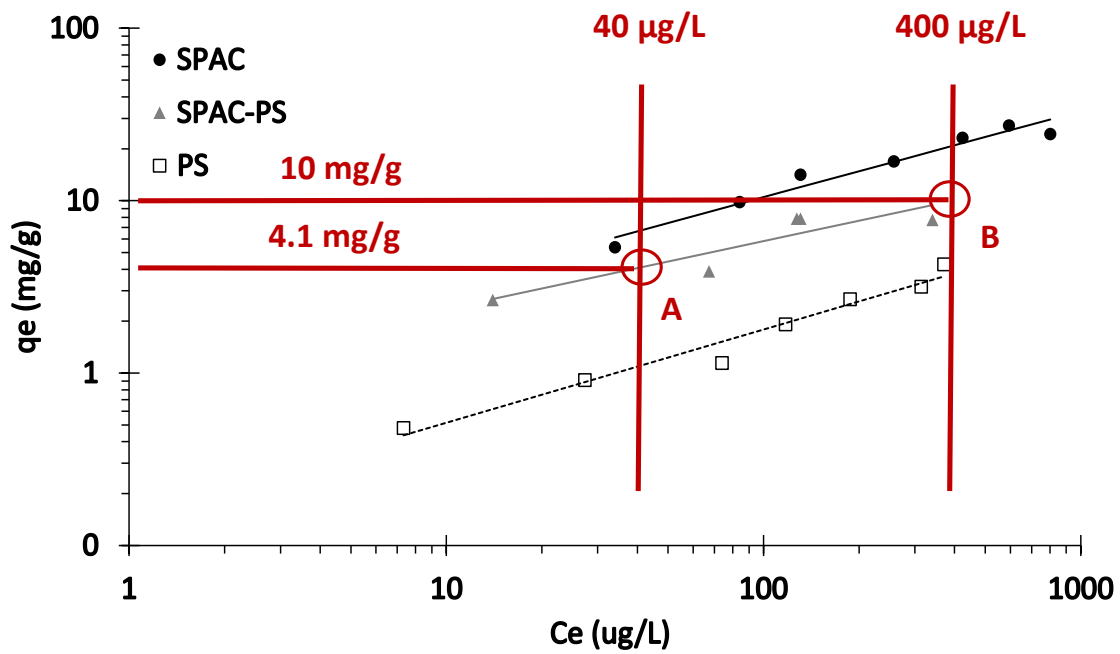
Figure B-5. Method for Determination of Adsorption Capacities ($q_{e\_measured}$) at 40 and 400 µg/L (point A and point B) from the isotherms (top). Comparison of experimental ($q_{e\_measured}$) and weighted average (i.e., calculated from experimental values) ($q_{e\_calculated}$) adsorption capacities at 40 and 400 µg/L (bottom).

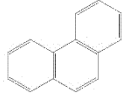**Table B-1. Molecular Properties of Phenanthrene. Adapted from Zhang et al., 2010.**

Molecular weight (g/mol)	Molecular size (ÅxÅxÅ)	Solubility in water (mg/L)	Density (g/cm^3)	log K_{ow}	λ_{UV} (nm)	Molecular Structure	Planarity (dihedral)
178.23	11.7 x 8.0 x 3.4	1.1	1.063	4.68	250		Planar (0)

Table B-2. Programmable Thermal Analysis (PTA) Results for Neat PS and SPAC-PS Composite Before and After PNT Adsorption.

Sample	Elemental Carbon (%)			
	1	2	3	Ave ± Std. Dev.
Neat PS Before PNT Adsorption	0.02	0.05	0.08	0.05 ± 0.03
Neat PS After PNT Adsorption	0.08	0.18	0.10	0.12 ± 0.05
SPAC-PS Composite Before PNT Adsorption	10.3	10.3	10.4	10.4 ± 0.02
SPAC-PS Composite After PNT Adsorption	11.8	12.6	11.4	11.9 ± 0.50

Table B-3. Elemental Composition of PS Pellets, PS Fibers, PS-SPAC Composite Fibers

Elements detected less than 0.1% in neither of the samples were not reported. The errors reported are two standard deviation of 60 seconds of measurement for one sample. Elements detected more than 1% were underlined.

Elements (%)	PS pellets	Neat PS fibers	PS-SPAC composite fibers
C, O, H	$\underline{100 \pm 0.00}$	$\underline{98.0 \pm 0.02}$	$\underline{80.0 \pm 0.11}$
W	<0.1	0.1 ± 0.00	<0.1
Zn	<0.1	0.1 ± 0.00	0.1 ± 0.00
Fe	<0.1	0.1 ± 0.01	$\underline{14 \pm 0.09}$
Ti	<0.1	<0.1	0.1 ± 0.01
Ca	<0.1	0.2 ± 0.02	$\underline{1.7 \pm 0.05}$
Al	<0.1	<0.1	0.5 ± 0.21
P	<0.1	<0.1	0.4 ± 0.02
Si	<0.1	0.3 ± 0.08	$\underline{2.2 \pm 0.06}$
Cl	<0.1	<0.1	0.1 ± 0.01
S	<0.1	0.1 ± 0.04	0.6 ± 0.02
Mg	<0.1	$\underline{1.2 \pm 0.65}$	<0.1

Table B-4. Theoretical Adsorption Capacities for Individual and Composite Materials.

C_e	$q_{e\text{-SPAC}}$	$q_{e\text{-PS}}$	$q_{e\text{-SPAC-PS}}$ measured	$q_{e\text{-SPAC-PS}}$ calculated
(µg/L)	(mg/g)	(mg/g)	(mg/g)	(mg/g)
40	6.6	1.1	4.1	1.7
400	21	3.8	10	5.5

Non-Linear Freundlich Model

Non-linear Freundlich Model was employed to fit the experimental isotherm data (see equation 4.1):

$$q_e = K_F C_e^n \qquad\qquad [1]$$

where K_F [(mg/g)/(Ce)^n] is the capacity parameter equal to the amount adsorbed at a value of C_e equal to unity, and n is a dimensionless parameter related to the heterogeneity of the surface. The coefficient of determination (r^2) values indicated that FM exhibited the goodness of fit to the experimental data.

APPENDIX C

THE FOLLOWING CONTAINS SUPPLEMENTARY INFORMATION FOR

CHAPTER 6: MORPHOLOGY OF POLYMERIC ELECTROSPUN FIBERS

CONTAINING 0D BUCKMINSTER FULLERENE, 1D MULTIWALLED CARBON

NANOTUBES, AND 2D GRAPHENE OXIDE NANOMATERIALS.
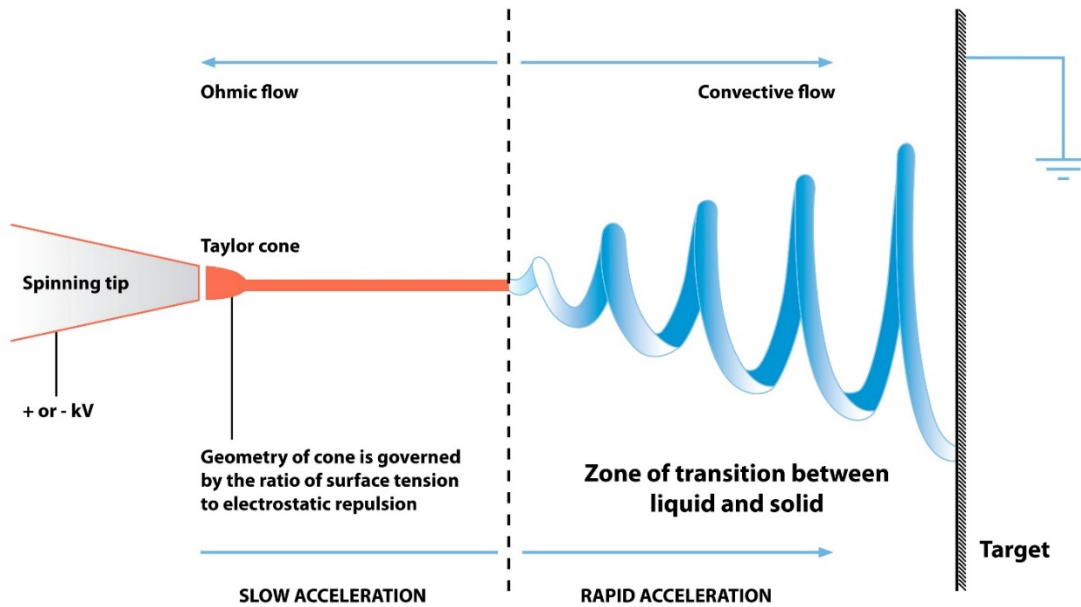
Figure C-1. Horizontal Electrospinning Setup showing Taylor cone formation as well as differences in charged jet between the capillary tip and grounded collector. Diagram by Joanna Gatford/The New Zealand Institute for Plant and Food Research Ltd, distributed under a CC-BY 2.0 License.
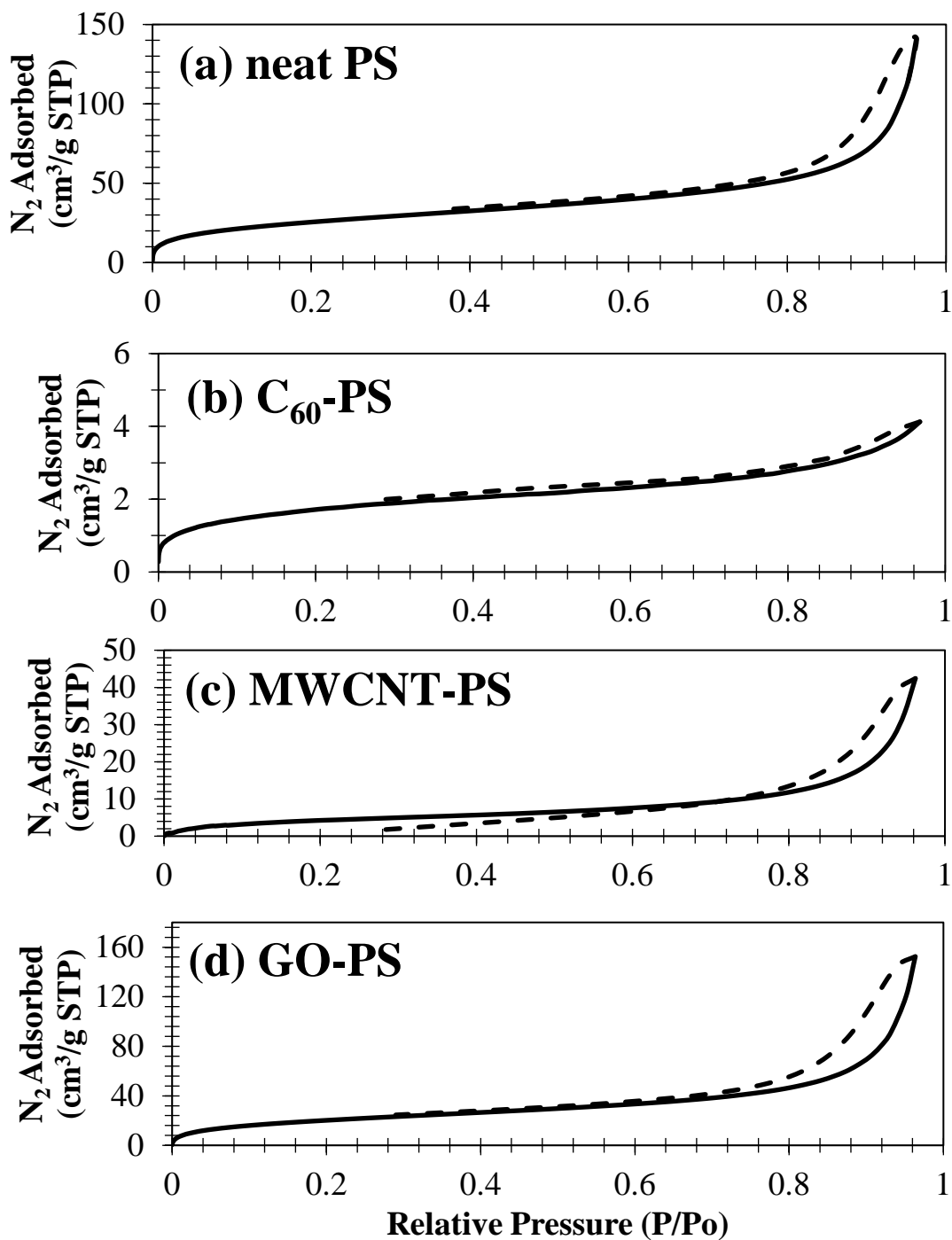
Figure C-2. Nitrogen Isotherms at 77K for Neat PS, C60-PS, MWCNT-PS, and GO-PS fibers. Adsorption branches are shown as solid lines and desorption branches are shown as dashed lines.
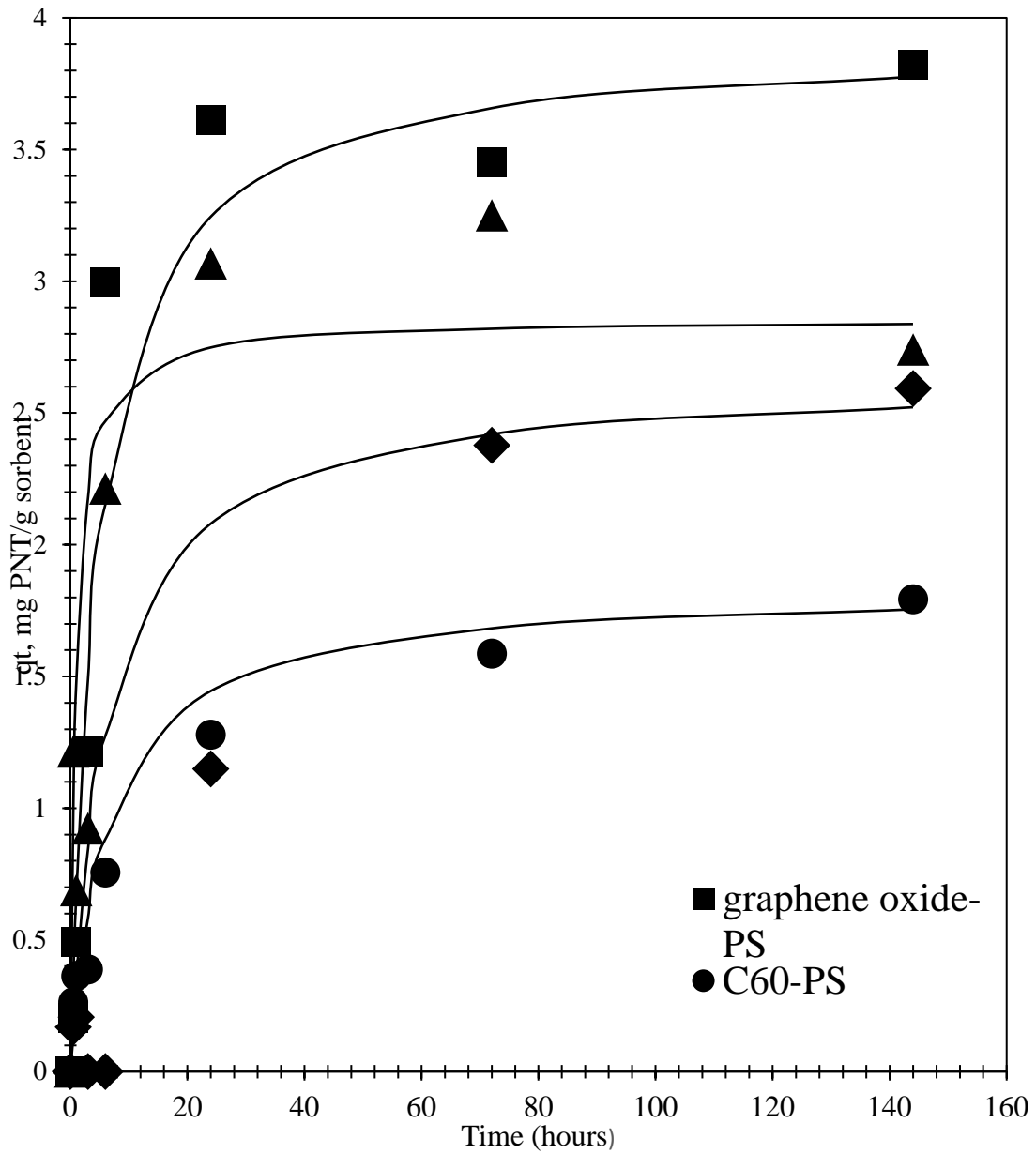
Figure C-3. Adsorption Capacity , q$_t$, mg PNT/g sorbent, for GO-PS, C60-PS, MWCNT-PS, and neat PS based on experimental data (points) and pseudo second order model (lines).
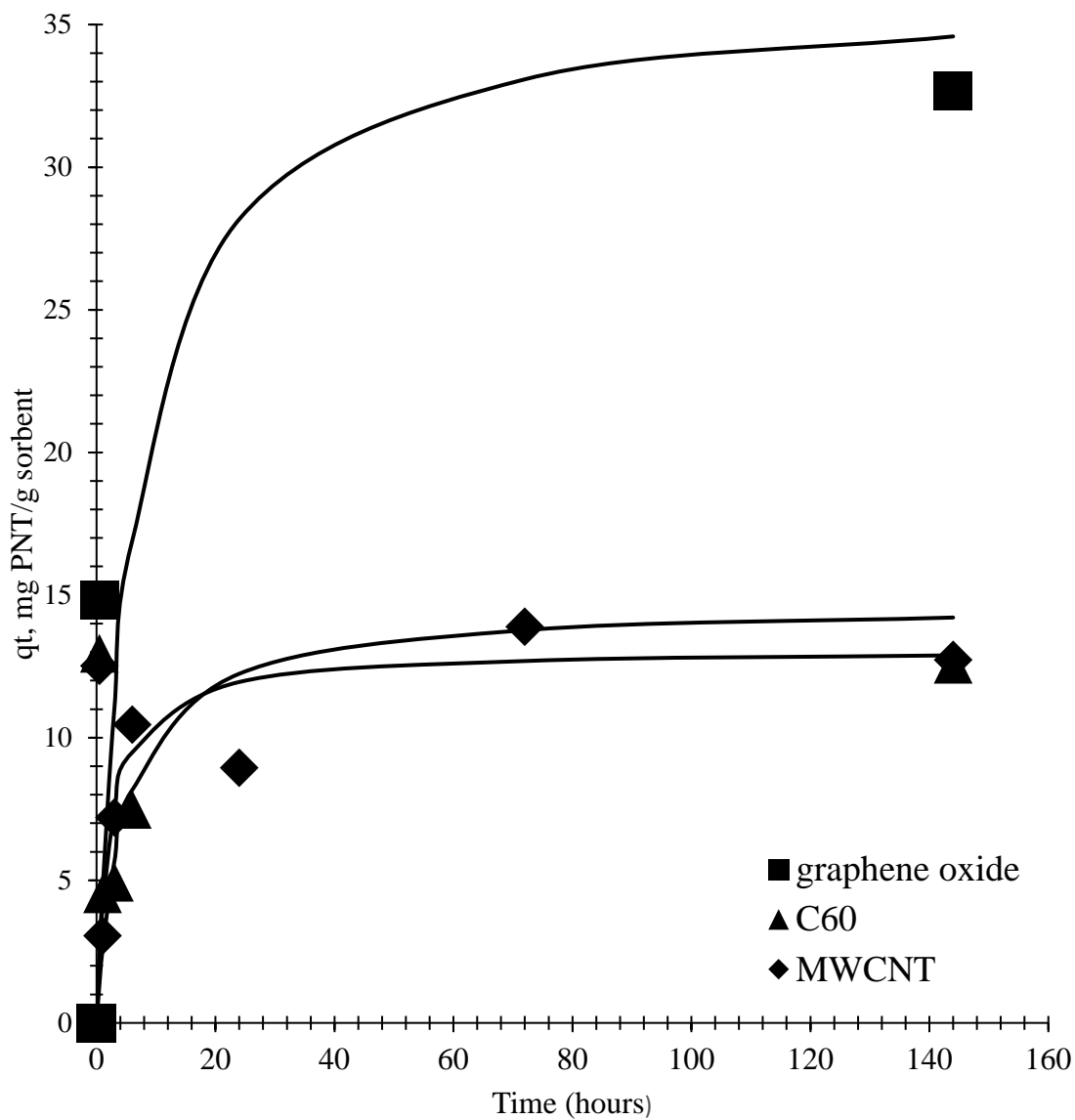
Figure C-4. Adsorption Capacity, q_t, mg PNT/g sorbent, for suspended GO, C60, and MWCNT based on experimental data (points) and pseudo second order model.

APPENDIX D

THE FOLLOWING CONTAINS SUPPLEMENTAL INFORMATION FOR

CHAPTER 7: HIERARCHICAL PORE STRUCTURES OF ELECTROSPUN

TITANIUM DIOXIDE AND GRAPHENE OXIDE NANOCOMPOSITES USING PVP

AS A SACRIFICIAL POLYMER.
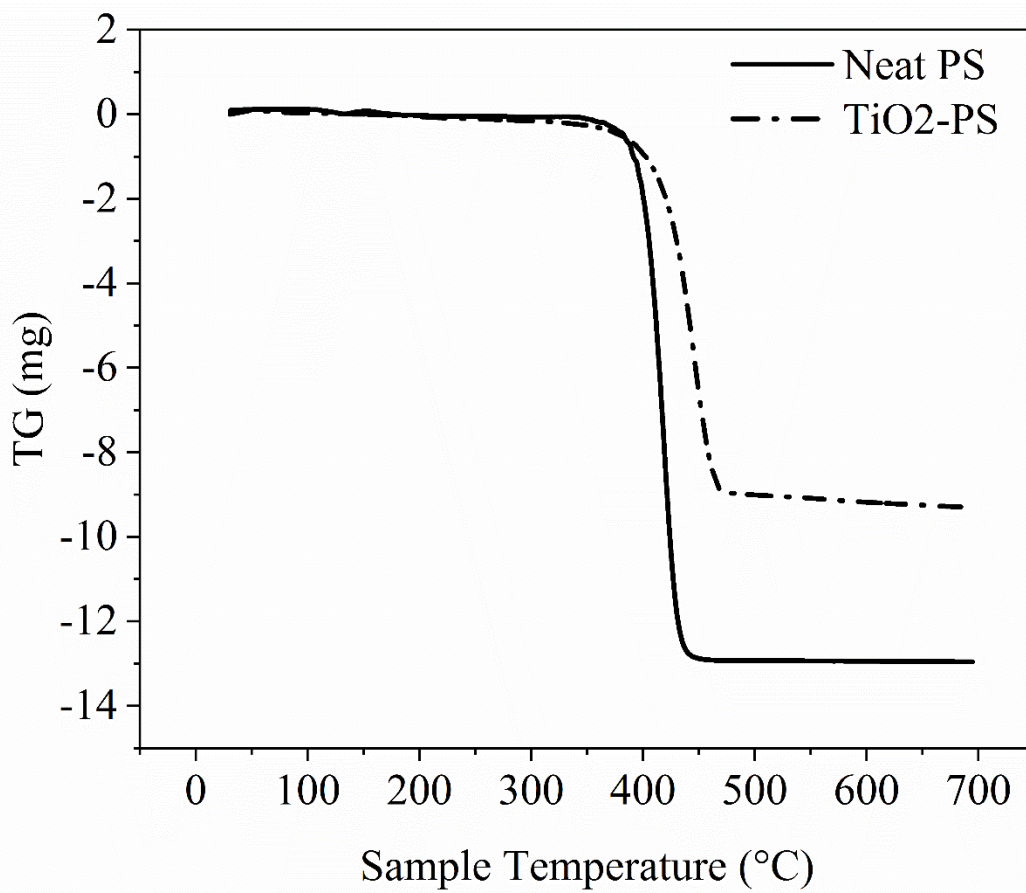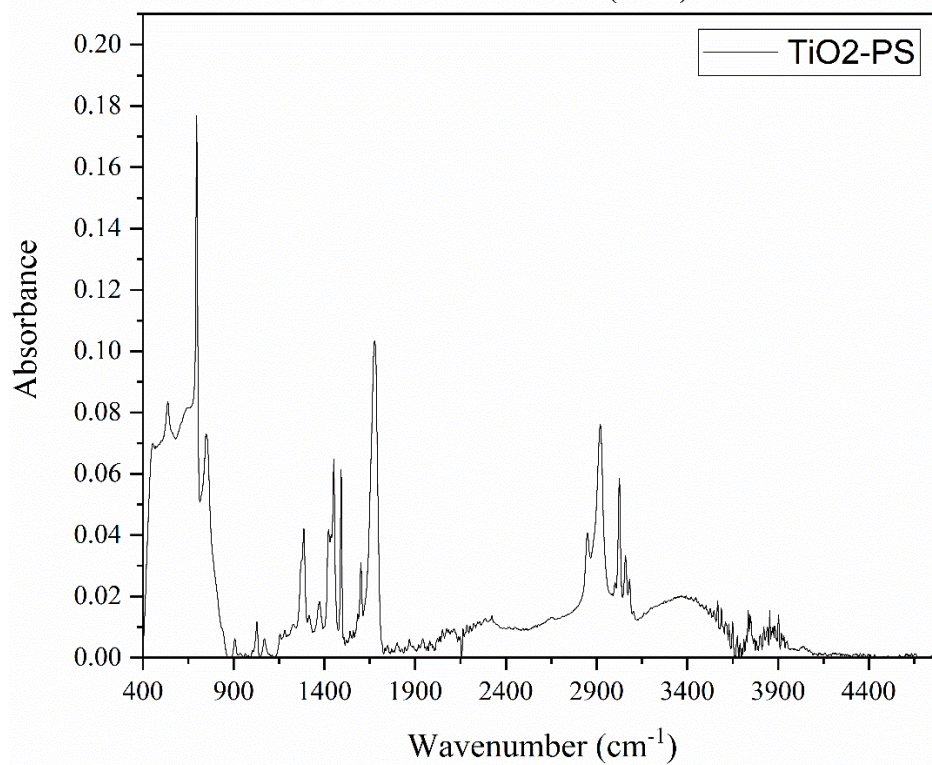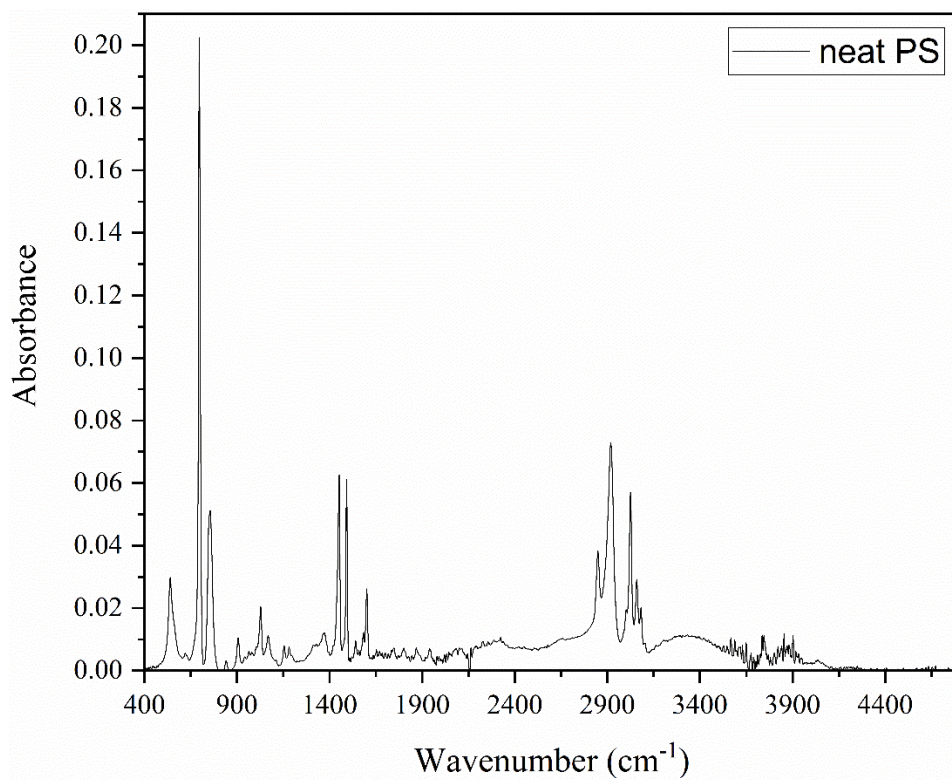
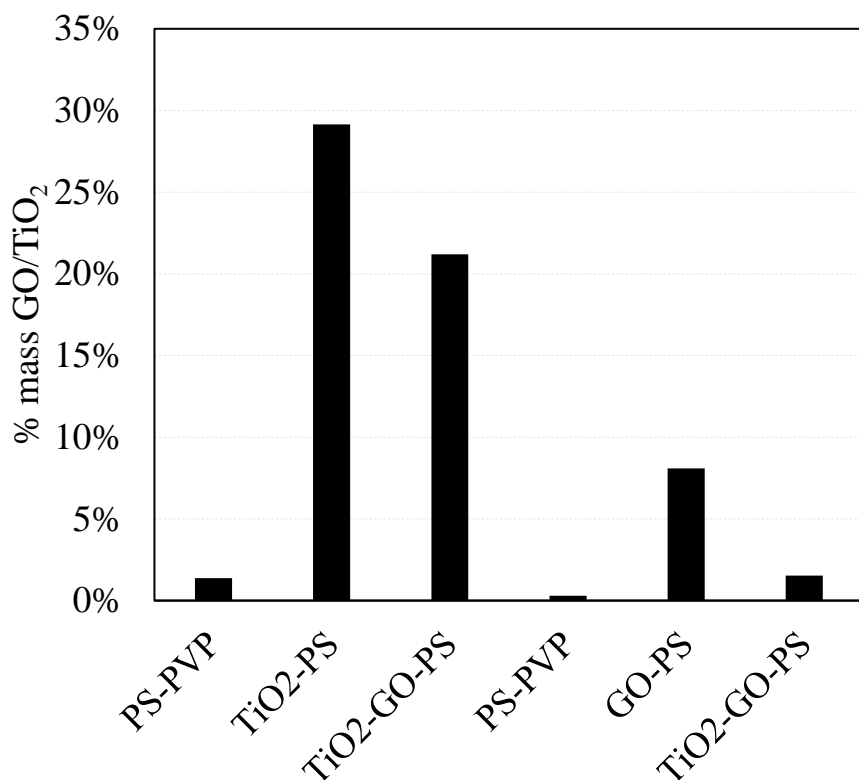**Figure D-1. TGA Degradation Profiles for Neat PS and TiO$_2$-PS.**

Figure D-2 FTIR Profiles of Neat PS and TiO₂-PS.

D-3. GO composition of NM-PS fibers by mass.

Non-Linear Freundlich Model

Non-linear Freundlich Model was employed to fit the experimental isotherm data (see equation 4.1):

$$q_e = K_F C_e^n \qquad\qquad [1]$$

where K_F [$(mg/g)/(Ce)^n$] is the capacity parameter equal to the amount adsorbed at a value of C_e equal to unity, and n is a dimensionless parameter related to the heterogeneity of the surface. The coefficient of determination (r^2) values indicated that FM exhibited the goodness of fit to the experimental data.